On the Application of the Sliding Box Analogy for an Energy Balance Approach to Fatigue Modeling in Cold Environments

Investigating the application of a novel, physics based, approach to fatigue damage modeling for aluminum without empirical fits.

Thesis in Aerospace Structures and Materials

Jasper F. Bramlage | 4790316

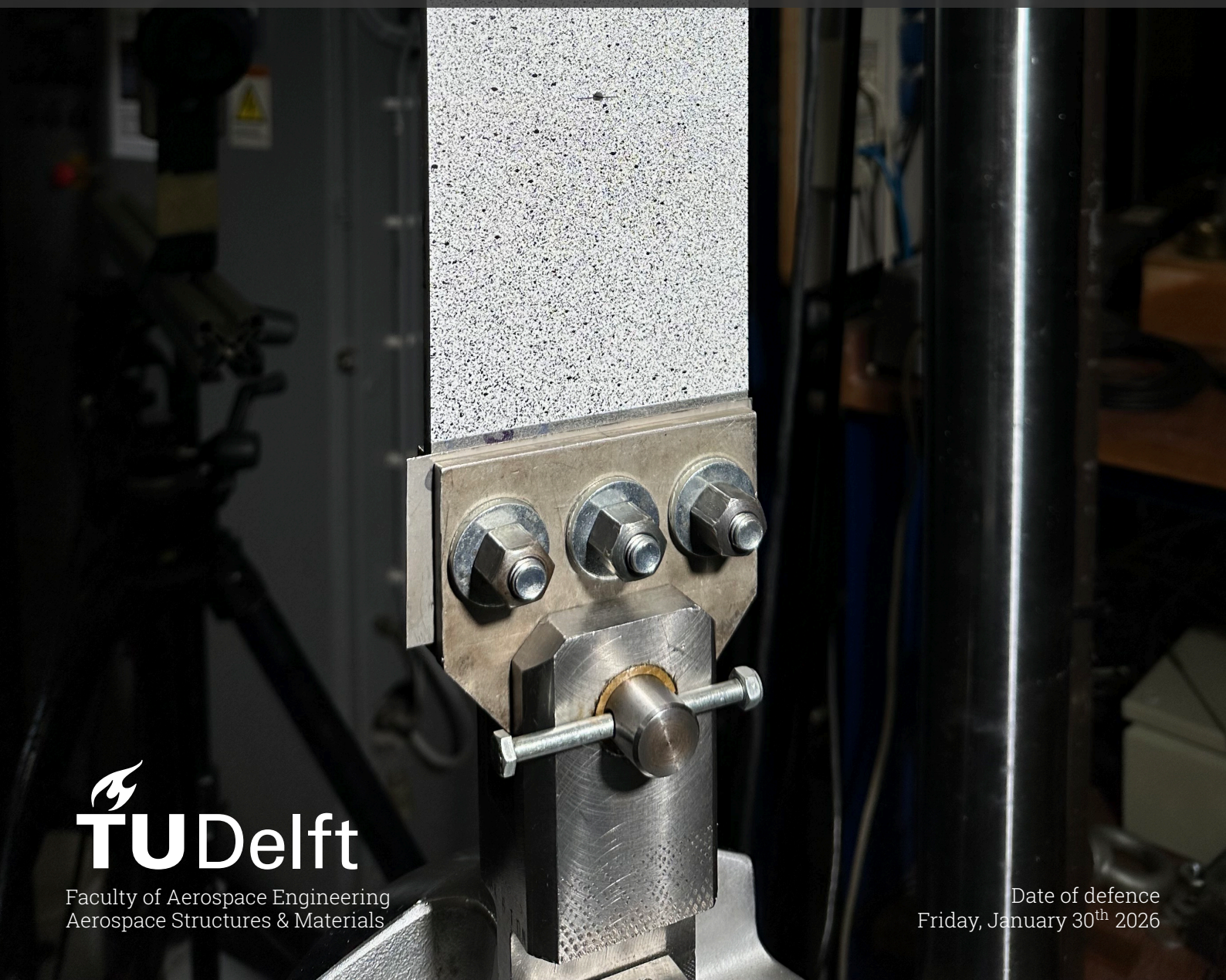

TU Delft
Faculty of Aerospace Engineering
Aerospace Structures & Materials

Date of defence
Friday, January 30th 2026

On the Application of the Sliding Box Analogy for an Energy Balance Approach to Fatigue Modeling in Cold Environments

Investigating the application of a novel, physics based, approach to fatigue damage modeling for aluminum without empirical fits.

by

Jasper F. Bramlage

To obtain the degree of Master of Science at the Delft University of Technology,
this thesis is to be defended publicly on Friday, January 30, 2026, at 14:00.

Student number:	4790316	
Project duration:	June 23, 2025 – January 12, 2026	
Graduation committee:	Dr.-ing. S. G. P. Castro,	TU Delft, Chair
	Prof.dr.ir. R. C. Alderliesten,	TU Delft, Responsible supervisor
	Dr.ir. J. A. Pascoe,	TU Delft, Examiner
	M.Sc. A. Raman,	TU Delft, Advisory Member

Cover: A fatigue test specimen fully clamped and loaded during a measurement cycle on the 250 kN MTS test machine. (Original)

An electronic version of this thesis is available at http://repository.tudelft.nl/.

TU Delft

Preface

This thesis concludes my master's degree in Aerospace Structures and Materials at TU Delft. Throughout my studies, I was fortunate to broaden my experience beyond the regular curriculum, most notably through Formula Student Team Delft and a subsequent internship in Formula 1. These experiences, in addition to the related coursework, shaped my interest in structural integrity and, in particular, fatigue analysis and its applications.

The work presented in this thesis investigates the application and extent of validity of a novel physics-based energy-balance approach with the sliding box analogy for predictive fatigue crack-growth modeling in aluminum alloys in cold environments. The project is motivated by the need for reliable damage-tolerance tools for future hydrogen-powered aircraft structures, where liquid-hydrogen storage tanks and adjacent structures are subjected to cyclic mechanical and thermal loading. To evaluate the model beyond a single baseline case, the scope includes a diversified selection of aluminum alloys and controlled variations in thickness and stress ratio, with a dedicated low-temperature test reaching -30°C. The methodology combines quasi-static tensile testing to determine case-specific elastic and plastic properties with constant-amplitude fatigue crack-growth experiments on standard geometry specimens. Crack growth is monitored via periodic high-contrast imaging, and Digital Image Correlation (DIC) is used to assess plastic-zone development around the crack tip. This research was conducted within the Luchtvaart in Transitie program, specifically in the context of the ICEFlight project.

The experimental campaign was carried out using the mechanical testing facilities at the Delft Aerospace Structures and Materials Laboratory. I am grateful to Dave, Chantal, and Alexander for their practical support and guidance during test setup and execution, especially regarding the climate chamber experiments and associated troubleshooting. I would like to sincerely thank René Alderliesten for his supervision and for the degree of technical freedom and critical input that helped shape the direction of this work.

Finally, I wish to thank my friends for being there for me throughout the project, both in Delft and from afar. A special thanks goes to my family for their unwavering support throughout this thesis and over the course of my studies.

Jasper F. Bramlage
Delft, January 2026

Abstract

This thesis investigates the application and extent of validity of a novel physics-based energy-balance approach with the Sliding Box analogy. The scope focuses on predictive modeling of fatigue crack growth in aluminum alloys at low temperatures. The motivation for this research arises from the increasing demand for reliable fatigue-life prediction methods in the context of hydrogen-powered aviation, where liquid-hydrogen storage tanks and adjacent structures are exposed to cyclic mechanical and thermal loading in cold environments. Traditional empirical approaches, such as Paris' law, are limited by their reliance on extensive experimental calibration, especially when material properties and environmental factors vary significantly.

The research aims to expand and validate the Energy Balance with the Sliding Box analogy (EBSB) framework by comparing its predictions to a comprehensive experimental dataset covering both room-temperature and low-temperature conditions down to $-30°$C. The study considers a diversified selection of aluminum alloys with quasi-static property differences that emulate changes expected at low temperature. The investigated materials are 7075-T6, 2024-T3, 6061-T6, and an artificially over-aged 2024-A300. Additionally, thicknesses from 1 to 6.5 mm and two stress ratios, $R = 0.1$ and $R = 0.5$, are varied to evaluate their influence on the modeled fatigue crack-growth response. The methodology combines quasi-static tensile testing to determine case-specific elastic–plastic properties with constant-amplitude fatigue crack-growth experiments on standard geometry specimens. Crack growth is measured via periodic high-contrast image capture. Furthermore, Digital Image Correlation (DIC) is employed to evaluate plastic-zone development from periodic displacement-field measurements around the advancing crack tip.

The results demonstrate that the EBSB model—particularly in its direct sliding-box form—captures the general trends and order of magnitude of fatigue crack growth in aluminum alloys well. However, predictive accuracy is limited by the current formulation of the plastic energy dissipation term and by the treatment of stress-state transitions (plane stress/plane strain). The quantification of plastic-volume growth within the energy balance was varied in an attempt to capture increased energy absorption at low temperature. The model tends to overestimate crack-growth rates, especially for pronounced variations in yield strength and strain hardening relative to the 7075-T6 baseline. This effect is not mitigated by adopting larger plastic-zone approximations; for lower thicknesses of 7075-T6, however, using a larger plastic-zone estimate (e.g., based on a von Mises yield criterion) reduces model error, consistent with better agreement with the plane-stress assumption.

Overall, the EBSB model is sensitive to material-specific strain-energy absorption characteristics, particularly yield strength and the degree of strain hardening. Experimental observations confirm the expected increase in yield strength and work hardening at low temperature, but also reveal an unexpected decrease in ductility for the low-temperature 7075-T6 tests, highlighting the complex coupling between material behavior and environment. Improvements to the EBSB framework are proposed, including a parametrically defined plastic strain energy density derived from quasi-static stress–strain data and the introduction of a damping term, C_p, to account for crack-shielding effects. Recommendations for future work include expanded cryogenic testing, improved DIC resolution, and the development of more robust analytical and numerical treatments to better capture strain hardening, stress-state transitions, and plastic-zone evolution.

This work contributes to the development of more predictive, less empirically dependent fatigue modeling approaches for aerospace structures operating in cold and cryogenic environments, with direct relevance to the design and safety assessment of hydrogen storage systems in next-generation aircraft.

Contents

List of Figures

List of Tables

Nomenclature

Abbreviations

Abbreviation	Definition
AoI	Area of interest
DIC	Digital image correlation
EBSB	Energy Balance with Sliding Box analogy (energy-balance + sliding-box analogy framework)
EPFM	Elastic-plastic fracture mechanics
FEA	Finite element analysis
FOV	Field of view
LEFM	Linear elastic fracture mechanics
MTS	Material Testing System (manufacturer name) fatigue testing machine
RMSE	Root mean square error
SED	Strain energy density
SERR	Strain energy release rate
Vic-2D	Correlated Solutions Vic-2D (2D DIC software)

Symbols

Symbol	Definition	Unit
A	Area	$[\mathrm{mm}]$
A_i	Area of iso-strain region i (DIC post-processing)	$[\mathrm{mm}]$
$\mathbf{A}$	Subset deformation/shape-function matrix in DIC mapping	
a	Crack length	$[\mathrm{mm}]$
a_{eff}	Effective crack length (Irwin), $a_{\mathrm{eff}} = a + r_y$)	$[\mathrm{mm}]$
c	Effective crack length (Dugdale), $c = a + \rho$	$[\mathrm{mm}]$
C	Paris-law material constant	$[\mathrm{mm}/\left(\mathrm{cycle} \cdot \mathrm{MPa}\sqrt{\mathrm{m}}\right)]$
C_p	Damping factor accounting for plastic crack shielding phenomena	$[\mathrm{mJ} \cdot \mathrm{mm}]$
C_{fric}	Sliding-box model constant (friction term)	$[-]$
C_{stic}	Sliding-box model constant (stiction term)	$[-]$
d	Displacement vector (DIC)	
d_{opt}	Optimal displacement from subset matching (DIC)	
E	Young's modulus	$[\mathrm{GPa}]$
E'	Effective Young's modulus (plane stress/strain form)	$[\mathrm{GPa}]$
E^*	Effective stiffness used with finite-width correction ($E^* = E/\beta$)	$[\mathrm{GPa}]$
F	Reference-image intensity distribution (DIC)	
$F(t)$	Forcing function in sliding-box analogy (energy-based)	$[\mathrm{mJ}]$
G	Strain energy release rate (SERR)	$\left[\mathrm{J}/\mathrm{m}^2\right]$
g	Gray-value residual vector (DIC)	
$\mathbf{G}$	Subset intensity-gradient matrix (DIC)	
K	Stress intensity factor	$[\mathrm{MPa}\sqrt{\mathrm{m}}]$

Symbol	Definition	Unit
K_I	Mode I stress intensity factor	$[\mathrm{MPa}\sqrt{\mathrm{m}}]$
K_{eff}	Effective stress intensity factor (closure-corrected context)	$[\mathrm{MPa}\sqrt{\mathrm{m}}]$
K_T	Stress concentration factor	$[-]$
L	Effective specimen length	$[\mathrm{mm}]$
m	Paris-law exponent	$[-]$
N	Number of load cycles	$[-]$
N_{step}	Cycle increment between measurement points	$[-]$
Q	Golden-ratio scale factor in plastic energy density relation	$[-]$
R	Stress ratio ($R = S_{\min}/S_{\max}$)	$[-]$
r	Radial coordinate from crack tip (polar form)	$[\mathrm{mm}]$
r_p	Plastic-zone radius	$[\mathrm{mm}]$
S	Engineering/nominal stress	$[\mathrm{MPa}]$
$S_{\max}$	Maximum cyclic stress	$[\mathrm{MPa}]$
$S_{\min}$	Minimum cyclic stress	$[\mathrm{MPa}]$
S_{op}	Crack opening stress	$[\mathrm{MPa}]$
$S(t)$	Sinusoidal stress function used in sliding-box forcing definition	$[\mathrm{MPa}]$
T	Specimen thickness	$[\mathrm{mm}]$
t	Time in loading functions	$[\mathrm{s}]$
U	Energy (generic)	$[\mathrm{mJ}]$
U_a	Energy dissipation due to crack surface creation	$[\mathrm{mJ}]$
U_e	Elastic energy dissipation	$[\mathrm{mJ}]$
U_p	Plastic energy dissipation	$[\mathrm{mJ}]$
U_{spring}	Stored/absorbed elastic energy from Hooke's Law	$[\mathrm{mJ}]$
$U_{\max}$	Maximum absorbed energy per cycle	$[\mathrm{mJ}]$
$U_{\mathrm{EB},i}$	Energy balance at cycle increment i (EBSB context)	$[\mathrm{mJ}]$
U_{op,E^*}	Opening-stress-level energy term (cracked effective stiffness)	$[\mathrm{mJ}]$
$U_{\mathrm{op},E}$	Opening-stress-level energy term (un-cracked elastic stiffness)	$[\mathrm{mJ}]$
V	Volume	$[\mathrm{mm}^3]$
V_p	Plastic volume	$[\mathrm{mm}^3]$
W	Specimen width	$[\mathrm{mm}]$
W_0	Strain energy density ($W_0 = \int_0^\epsilon \sigma \, d\epsilon$)	$[\mathrm{mJ}/\,\mathrm{mm}^3]$
W_p	Plastic strain energy density	$[\mathrm{mJ}/\,\mathrm{mm}^3]$
Y	Geometry factor in stress intensity factor relations (general form)	$[-]$
ΔK	Stress intensity factor range	$[\mathrm{MPa}\sqrt{\mathrm{m}}]$
ΔK_{eff}	Effective stress intensity factor range which includes an opening stress correction	$[\mathrm{MPa}\sqrt{\mathrm{m}}]$
ΔK_I	Mode I stress intensity factor range	$[\mathrm{MPa}\sqrt{\mathrm{m}}]$
$\Delta G_{\max}$	Range in maximum strain energy release rate	$[\mathrm{J}/\mathrm{m}^2]$
U	Applied work (energy-balance)	$[\mathrm{mJ}]$
U_a	Surface-creation energy dissipation	$[\mathrm{mJ}]$
U_p	Plastic energy dissipation	$[\mathrm{mJ}]$
U_e	Elastic energy dissipation	$[\mathrm{mJ}]$
β	Finite-width / geometry correction factor (e.g. Feddersen)	$[-]$
γ	Surface roughness factor factor	$[-]$
ϵ	Strain	$[-]$ or $[\%]$
ϵ_v	Equivalent (Von Mises) strain	$[-]$
ϵ_y	Yield strain (from offset-yield definition)	$[-]$

Symbol	Definition	Unit
λ	Shear lip scaling factor	$[-]$
ν	Poisson's ratio	$[-]$
ρ	Dugdale plastic zone length ahead of crack tip	
σ	Stress	$[\mathrm{MPa}]$
σ_0	Remote/applied nominal stress (far-field)	$[\mathrm{MPa}]$
σ_v	Equivalent stress used with equivalent strain in plastic energy density estimation	$[\mathrm{MPa}]$
σ_{vm}	Von Mises equivalent stress	$[\mathrm{MPa}]$
σ_x	Normal stress component in x direction (also y, z)	$[\mathrm{MPa}]$
τ	Shear stress (generic)	$[\mathrm{MPa}]$
τ_{zx}	Shear stress component in zx plane (also zy, xy)	$[\mathrm{MPa}]$
θ	Polar angle around crack tip (for stress-field/plastic-zone)	
θ_0	Crack-growth direction angle	
$\xi(x, p)$	Subset mapping/shape function in DIC correlation	
φ	Golden ratio (used as exponent in plastic energy density relation)	$[-]$

1

Introduction

1.1. Motivation and Context

Hydrogen is a leading candidate for low-emission aviation fuel, but liquid-hydrogen adoption brings its own storage and integration challenges. These include cryogenic tanks, insulation, boil-off management, and dedicated safety systems. The challenges of liquid hydrogen introduce new cyclic loading and thermal environments that make fatigue crack growth and damage tolerance central concerns for the design of tanks and surrounding aircraft structures. Loading and thermal environmental conditions motivate the need for fatigue crack-growth modeling approaches that remain predictive when temperature and material responses change, rather than relying solely on extensive testing in complex cold environments for empirical fits.

The project is conducted within the Luchtvaart in Transitie (LiT) program, more precisely in the context of the ICEFlight project. LiT is an R&D and innovation program aimed at accelerating aviation sustainability, with climate-neutral flying by 2050 as a long-term guiding target. Specifically, the ICEFlight project focuses on technologies for hydrogen-powered aircraft, investigating liquid hydrogen as both a fuel and a cooling source for future aircraft powertrains [1].

1.1.1. Hydrogen in Aviation

Hydrogen is considered a promising alternative aviation fuel due to its potential to eliminate carbon dioxide emissions when consumed and significantly reduce other combustion by-products associated with conventional hydrocarbon-based fuels. Its high gravimetric energy density, in comparison with other alternative power sources, makes it attractive for aerospace applications where mass efficiency is critical. This highlights hydrogen as one of the best potential options for future low-emission propulsion systems. As highlighted by Nagelsmit and Veldhuis [2] from NLR and TU Delft, hydrogen therefore represents a critically important technology in the transition toward sustainable aviation, complementing other options such as sustainable aviation fuels and hybrid-electric propulsion.

However, the adoption of hydrogen requires overcoming substantial engineering challenges related to fuel storage and aircraft integration. Compared to liquid hydrocarbons, hydrogen has a relatively lower volumetric energy density, necessitating larger or more complex storage systems and introducing significant changes to aircraft configurations and structures. Liquid hydrogen storage, named as the preferred solution for aviation [2], requires cryogenic tanks, insulation, boil-off management, dedicated fuel handling, and safety systems. These requirements extend beyond the aircraft, demanding new airport-side infrastructure for hydrogen production, storage, and refueling. As such, while hydrogen offers compelling emissions advantages, its practical implementation will require coordinated advances in airframe design, thermal and structural systems, and global aviation fuel logistics.

Hordeski [3] investigates hydrogen with cryogenic as well as compression storage solutions in the context of alternative future fuels. Hydrogen at cryogenic temperatures presents significant challenges due to the extreme conditions required for liquefaction and storage. Hydrogen must be cooled to -253°C to remain in liquid form, which demands specialized refrigeration systems. The process of liquefaction

itself is highly energy-intensive and can consume about 40% of the hydrogen's energy content. In general, cryogenic applications imply storage temperatures under $-150°$C [4], which can therefore also relate to structures surrounding liquid hydrogen-related equipment.

Once stored, liquid hydrogen faces evaporation losses, known as boil-off. Even in highly insulated tanks, hydrogen gradually escapes as gas due to heat absorption. NASA, for example, experienced 44% excess hydrogen usage when fueling space shuttles, as a large portion boiled off before use. This problem is particularly severe in automotive applications—hydrogen stored in vehicles can evaporate at a rate of up to 4% per day if left idle, leading to significant fuel losses over time [3]. This fact demonstrates the relevance of hydrogen exposure for storage solutions and may lead to pressure-induced load variation as well.

The safety risks associated with cryogenic hydrogen storage are another major concern. Handling liquid hydrogen requires intrusive precautions. Additionally, hydrogen is highly flammable, and leaks can be difficult to detect due to its colorless and odorless nature, necessitating specialized fueling procedures and fail-safe design. Despite its advantages, these challenges make large-scale cryogenic hydrogen storage costly and complex.

1.1.2. Relevance of Fatigue Analysis

Traditionally, fatigue analysis is an important topic in the design of aircraft due to the typical loading profiles found in flight operation. The cyclic nature of reversed loading between ground and flight operation as well as the load profiles found in flights from vibrations, cargo, pressurization, turbulence, and maneuvering loads necessitates fatigue-related structural analysis. When considering the move to alternative fuel requirements such as hydrogen, the necessity for new structural modeling approaches for cryogenic storage vessels becomes evident. Whether the storage tanks and related structure are simply suspended in an airframe or are implemented in a load-carrying capacity, the effects of the new environmental conditions need to be accounted for.

When we take a look at these new structural challenges, fatigue analysis is especially relevant in the design of cryogenic hydrogen storage tanks and their surrounding aircraft structures because these components may be subject to repeated pressure cycling during fueling and flight, as well as severe thermal cycling when cooled to cryogenic temperatures in addition to regular flight loads. In hydrogen-powered aircraft, the liner and tank wall may endure large-amplitude temperature shocks, which can cause cyclic stress reversals that combine with the structural loads and safety requirements of flight operation. At cryogenic temperatures, commonly used aluminum alloys such as aluminum alloy 6061-T6 show marked changes in mechanical behavior. For example, their strength and work hardening rate increase dramatically, and cyclic loading at around 108 K can lead to significantly longer fatigue life than at room temperature [4]. Furthermore, when aluminum is exposed to hydrogen, its fatigue crack growth rate is strongly influenced by the frequency of loading: at low frequencies, hydrogen environments enhance crack propagation more than inert gases [5]. These phenomena reflect the beginnings of a dual challenge: aluminum may become stronger and more fatigue-resistant in cryogenic cycling, but hydrogen exposure and pressure cycling can accelerate damage depending on the exact storage manner and temperature.

These considerations all contribute to the necessity of novel sizing and modeling approaches for this technically challenging new engineering design context.

1.2. Contribution of the Presented Research

The aim of this thesis is to investigate the mechanisms and phenomena involved in alternative, physics-based approaches to model fatigue damage propagation, such as energy balance terms and ways to create predictive formulations. A focus will be directed towards the low-temperature properties of relevant aluminum metals for hydrogen tanks that have an effect on the fatigue damage tolerance in plates, with particular emphasis on how well crack damage propagation can be modeled without having to conduct experiments at low temperatures, between $0°$C and $-50°$C, or even at cryogenic temperatures below $-100°$C.

This thesis aims to contribute to the development of future models capable of characterizing low-temperature fatigue damage growth. This significantly reduces the complications and costs associated with determining empirical cryogenic material and damage growth properties. Additionally, an alternative to Paris curve exponential fits would also be useful to work towards eliminating issues with dimensional inaccuracies. Finding such a novel approach without delving into the complexities of thermodynamics or the need for computationally intensive steps can provide a new angle that allows fatigue damage modeling to be more analytically predictive and less testing dependent.

1.3. Overview of the Coming Chapters

Chapter 2 reviews literature concerning the fracture-mechanics basis for fatigue crack growth, motivates an energy-balance description, and summarizes the sliding-box analogy together with plastic-zone and low-temperature effects relevant to aluminum structures. Chapter 3 then states the research objective, defines research questions, formulates hypotheses, and derives the scope and limits that frame the investigation. Chapter 4 details the theoretical adaptations to the energy-balance model and the complete experimental methodology, including specimen selection, quasi-static and fatigue testing (also at low temperature), Digital Image Correlation setup, and data processing. Chapter 5 presents the experimental results and the corresponding Energy Balance with Sliding Box (EBSB) model outcomes, including crack-growth and strain-field analyses. Finally, chapters 6 through 8 will cover an interpretation of the findings, consolidate the conclusions, and provide targeted recommendations for future work on low-temperature fatigue modeling and testing.

2

Literature Review

2.1. Overview of the Theoretical Background

Fracture mechanics provides a framework for analyzing how cracks initiate and grow in structural materials, enabling engineers to predict failure and evaluate the integrity of components operating under complex loading conditions. Its development arose from the need to understand brittle failures that could not be explained by traditional continuum strength theories, particularly in applications where flaws, stress concentrations, or cyclic loading significantly reduce structural reliability. Today, fracture mechanics is integral to the design, assessment, and life management of critical systems across aerospace, civil, and mechanical engineering. By relating material resistance to crack growth with the applied stress state, it allows for more accurate safety evaluations than those based solely on nominal stress or yield criteria, especially when defects are unavoidable or damage accumulates over time.

This chapter presents the theoretical and methodological foundations relevant to fatigue crack growth in aerospace structures. It begins by outlining established knowledge on crack propagation and fracture mechanics, highlighting the key principles for fatigue damage analysis. The Paris curve fatigue damage accumulation model is reviewed to identify its strengths and limitations, providing context for the further development of energy-based interpretations of fatigue damage growth. The energy balance approach and a conceptual analogy for cycle dependency are presented from prior studies, followed by a review of methods used to estimate plastic energy density and characterize the plastic zone at a crack tip. Particular emphasis is placed on linear elastic approaches for basic validation of the novel analogy-based approach.

The chapter then synthesizes literature on the effects of low and cryogenic temperatures on fatigue and fracture behavior, reflecting their importance in aerospace applications and emerging cryogenic systems. Finally, research addressing the practical aspects of fatigue testing is reviewed, including the capabilities, constraints, and methodologies associated with commonly used experimental equipment. Collectively, these sections establish the state of knowledge relevant to the subsequent analysis and should aid in motivating the approaches adopted later in this thesis.

2.2. Crack Propagation & Fracture Mechanics

According to Wang [6], fracture mechanics is commonly divided into linear elastic fracture mechanics (LEFM) and non-linear elasto-plastic fracture mechanics (EPFM). The applicability of either approach depends on the material behavior, the loading conditions, and the extent of plasticity near the crack tip. LEFM provides accurate predictions when the material response is predominantly elastic and the plastic zone remains small. In contrast, low-strength steels, some aluminum alloys, and polymers often exhibit significant crack-tip plasticity, particularly under high loads, which could make EPFM more appropriate.

Stress and strain analyses are also frequently idealized using plane stress or plane strain assumptions. Plane stress refers to a state where the stress through the thickness is negligible, a condition characteristic of thin plates or structures. This assumption is often applied in fracture mechanics to describe the stress field in thin bodies containing cracks, where out-of-plane stresses are minimal [6][7].

$$\sigma_z = 0, \quad \tau_{zx} = 0, \quad \tau_{zy} = 0, \quad \epsilon_z \neq 0 \tag{2.1}$$

Plane strain conditions exist in thicker bodies, where the material dimension out of the loading plane is greater than in-plane dimensions. This leads to $\sigma_z \neq 0$ and $\epsilon_z = 0$ in comparison to the plane stress condition. In the context of fatigue life and fracture mechanics in the rest of this thesis, the plane stress condition will be generally assumed and provides a basis for the assumptions of linear elastic behavior of plates.

In ductile materials, areas of stress concentration, such as notches, holes, and other defects, create regions of localized plasticity, which prevent failure from localized stresses even above the yield point. However, under repeated cyclic loading above the fatigue limit, microcrack nucleation can occur in slip bands and lead to fatigue crack initiation [8]. These cracks then act as new stress concentrators, allowing propagation even under bulk stresses below the yield strength, eventually leading to failure above a critical stress intensity.

A common approach to numerically represent stress concentrations is the stress concentration factor K_T, which is relevant for macro-sized geometric stress concentrations. When the size of a notch goes towards infinitely small, like in a fatigue crack, the theory behind the factor K_T breaks down; instead, one can use the approximation of a new term, the stress intensity factor. This is a factor that considers the finite width of a specimen as a function of the crack length [6].

$$K = \sigma_0 \beta \sqrt{\pi a} \tag{2.2}$$

$$\beta = \sqrt{\sec\left(\frac{\pi a}{W}\right)} \tag{2.3}$$

Where σ_0 is the applied stress at a clean and distant representative region of the specimen with width W, a is the crack length at the affected cross-section. These are also visually shown in 2.1. Equation 2.3 is the Feddersen geometry correction factor, which is useful for center-cracked plates with an existent crack of total length $2a$. Broek [7] shows that the more general solution according to Isida's mapping function, $K = Y\sigma_0\sqrt{a}$ in a center-cracked case, is very closely approximated by Feddersen up to $2a/W = 0.85$. This is generally after final failure, making Feddersen a suitable crack length geometry correction for fracture mechanics.

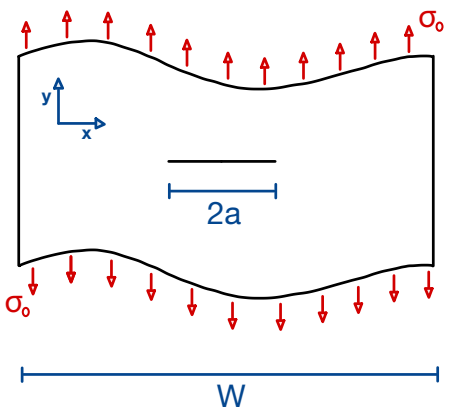

Figure 2.1: Fatigue plate geometry and stress, σ_0, definition.

After cracks have nucleated and propagated, a damaged section of plate will eventually fracture. According to Kotousov et al. [9], the classical linear elastic fracture criterion can be written in terms of the stress intensity factor as $K = K_C$, where K is the stress intensity factor at a crack tip and K_C is the critical value of the stress intensity factor or apparent fracture toughness. The critical stress intensity factor can additionally also be related to the plate thickness of the tested specimen material. When the applied stress level, ΔS, remains low, the size of the plastically deformed region ahead of the crack tip remains small in comparison with the other characteristic dimensions of the specimen geometry, which includes crack length. Therefore, at this low failure stress, the non-linear elasto-plastic criteria may be expected to recover the classical linear elastic criterion. As a crack propagates toward a length that would increase the value of the stress intensity factor to exceed the critical one, this assumption breaks down, defining the interval of where LEFM can be considered a good representation.

2.2.1. Existing Fatigue Damage Accumulation Predictions

The prediction of fatigue crack growth under constant-amplitude (CA) loading is a central concept in fracture mechanics, and it is commonly expressed using the Paris equation, which relates the rate of crack propagation to the range of the stress intensity factor. Schijve [8] outlines two main quantities which are essential for such a prediction. Firstly the crack growth resistance of the material, represented by:

$$\frac{da}{dN} = f(K), \tag{2.4}$$

Which defines the crack extension per cycle as a function of the stress intensity factor (K). As well as, the crack driving force $K(a)$, given as a function of crack length, which accounts for the stress intensity distribution in the structure as the crack grows. The incremental number of cycles ΔN_i required for a small crack extension Δa_i at crack length a_i can be obtained from

$$\Delta N_i = \frac{\Delta a_i}{\left(\frac{da}{dN}\right)_{a=a_i}}. \tag{2.5}$$

Integrating this relation between the initial crack length a_0 and a final crack length a_f yields the total number of cycles to failure:

$$N_{a_0 \to a_f} = \int_{a_0}^{a_f} \frac{da}{f_R(\Delta K)}. \tag{2.6}$$

When the Paris' law is applicable, the crack growth rate can be expressed as a power-law function of the stress intensity factor range in of constant amplitude cycles $\Delta K = K_{\max} - K_{\min}$:

$$\frac{da}{dN} = C(\Delta K)^m, \tag{2.7}$$

where C and m are material constants determined experimentally. The stress intensity factor range is generally defined as

$$\Delta K = \beta \Delta S \sqrt{\pi a}, \tag{2.8}$$

where β is a geometry correction factor and ΔS is the applied cyclic stress range. Substituting this relation into the fatigue life integral gives the crack growth life:

$$N = \frac{1}{C(\Delta S)^m} \int_{a_0}^{a_f} \frac{da}{(\beta\sqrt{\pi a})^m}. \tag{2.9}$$

Since β often varies with crack length, this integral is typically evaluated numerically. Nevertheless, it is evident that the fatigue life N is inversely proportional to $(\Delta S)^m$, implying that an increase in stress amplitude significantly accelerates crack growth. For most metallic materials, the exponent m is approximately 3; therefore, increasing the maximum stress level by a factor of 1.25 results in a twofold reduction in crack growth life, as $1.25^3 \approx 2$. The Paris equation thus provides a robust analysis framework for predicting fatigue crack propagation by linking material properties, geometry, and cyclic loading conditions through measurable parameters. The simplicity of this approach is its biggest strength and with some experimental data, the processing complexity and application effort remains minimal.

Overall, the Paris relation has done the engineering world well to provide a way to model fatigue damage growth in the stable crack growth regime. Unfortunately, this approach also has some drawbacks. Most importantly among these is the dependency on testing to empirically quantify the constants C and m. This process usually involves running a fatigue test with the exact geometry and material in question to then curve fit an exponential function to determine the Paris constants. Determining these test based curve fits can therefore become very time and resource intensive, especially with more complex applications or varieties of materials.

In the greater context of the motivating concepts relating to hydrogen storage in this thesis, the drawbacks of the Paris curve approach to fatigue damage modeling become evident. In order to find Paris constants for potential structural materials in varying environmental conditions, including cryogenic temperatures, experiments need to be conducted for each combination of variables. Especially in the context of extreme environments we can therefore define a very clear benefit from fatigue damage modeling that does not rely on empirical data.

Finally, in addition to the models listed here there are a variety of other existing approaches in addition to Paris' exponential curve fit approach. Some of these models are also significantly more accurate over the entire life of a metallic component taking into account initiation and final failure, as well as variable amplitude loading beyond the Miner's rule. These models include fully empirical and semi-empirical terms and are used for higher accuracy modeling of complex fatigue damage simulations often dependent on databases of information including models like AFGROW, strip yield approaches, as well as more general finite element analyses [10].

2.3. Energy Balance Description for Fatigue Damage Propagation

The energy balance approach provides an alternative way to describe fatigue crack growth - or more generally, fatigue damage growth - including the Paris curve, by focusing on the physical energy dissipation mechanisms rather than empirical power-law fits. Generally the concept is based on the strain energy release rate (SERR) approach as described by Griffith [11] and usually equates to the energy release rate related to crack growth to a change in applied work.

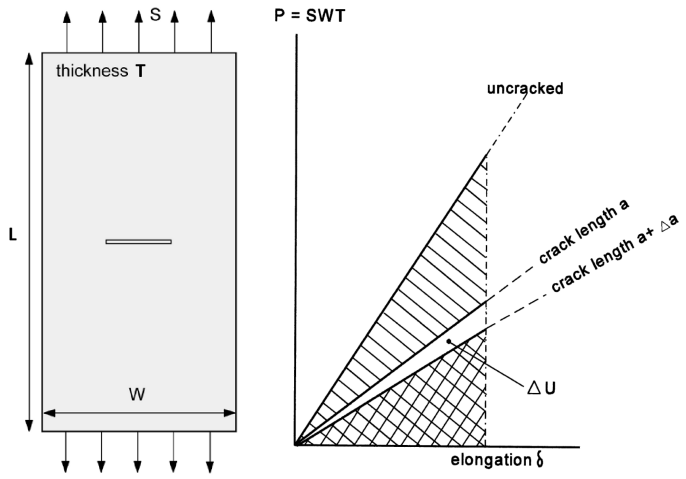

Figure 2.2: Elastic response and crack growth energy dissipation in a plate with and without a crack. Modified from Schijve [8]

The fundamental equation equates the change in applied work to the energy release rate due to damage growth and plasticity, plus the elastic energy lost in the process. Alderliesten [12] and Kuijk [13] state:

$$\dot{U} = \dot{U}_a + \dot{U}_p + \dot{U}_e \tag{2.10}$$

where:

- U represents the applied work,
- U_a is the energy dissipation due to crack surface creation,
- U_p corresponds to the energy lost due to plastic deformation,
- U_e accounts for the elastic energy dissipation.

Finding the contributions to this summation from relevant sources is critical to derive a representative equation. If the energy dissipation from fatigue damage accumulation can be defined robustly then the energy balance approach may provide a fitting framework for physics based analysis.

Kuijk [13] expresses the change in energy from 2.10 with respect to crack length (a) assuming that the change in applied work is the energy dissipated during crack surface energy and plastic energy dissipation:

$$\frac{dU}{da} = \frac{dU_a}{da} + \frac{dU_p}{da} \tag{2.11}$$

A further approach to the outlining of the various terms of the energy balance has been completed by Alderliesten [12] who hypothesizes that the energy dissipated per cycle (N) instead and can also be split into surface energy creation and plastic energy dissipation. It is stated that we can express the plastic energy dissipated for crack growth as the product of a change in plastic volume, V_p, and a plastic energy density dU_p/dV_p.

$$\frac{dU}{dN} = \frac{dU_a}{dN} + \frac{dU_p}{dN} = \frac{dU_a}{dA}\frac{dA}{dN} + \frac{dU_p}{dV_p}\frac{dV_p}{dN} \tag{2.12}$$

This specific analysis is powerful due to the common base for both sides of the equation being the cycle dependency dN. The following relations show the energy terms and the additional terms required to make them cycle dependent. Now, we can define the total energy absorption in an un-cracked specimen that is a distance of L between clamps under nominal stress S, as shown in Figure 2.2 as well.

$$U_{\text{spring}} = \frac{1}{2}\sigma\varepsilon WTL = \frac{1}{2}\frac{S^2}{E}WTL \tag{2.13}$$

The Feddersen correction factor can be employed to incorporate a crack length into Equation 2.13 using an effective stiffness $E^* = E/\beta$ for a correction of the energy. The correction is useful to define the stiffness of a plate that has been damaged by a crack reducing its effective stiffness – and as a consequence, the energy absorption. The maximum cyclic nominal stress is represented by $S_{\max}$ for the expression of maximum energy absorption $U_{\max}$.

$$U_{\max} = \frac{1}{2}\frac{S_{\max}^2}{E^*}WTL = \frac{1}{2}\frac{S_{\max}^2}{E}WTL\sqrt{\sec\left(\frac{\pi a}{W}\right)} \tag{2.14}$$

Next, the energy release from crack surface creation may be calculated using the Griffith theory, Equation 2.15, where we can assume the surface energy of a metal is in the order of $G = 1$ Jm^{-2} as Vitos et al. [14] confirms for aluminum. The change in crack surface per cycle is equal to two times the product of incremental increase in crack length and thickness for the two new crack surfaces that are created per unit of crack growth.

$$\frac{dU_a}{dA} = G \rightarrow \frac{dU_{\mathrm{a}}}{da} = 2 \cdot \frac{dU_{\mathrm{a}}}{dA} \gamma \lambda T \tag{2.15}$$

To find the total energy dissipated for crack growth itself we can continue by scaling this energy release with corrections for shear lip formation and surface roughness. Kuijk [13] defined the surface roughness factor $\gamma = 1$ due to lacking consensus for quantifying this value in literature. Hogeveen [15] however, did manage to find trends of increasing surface roughness related to larger values of the stress ratio $R = S_{\min}/S_{\max}$, as well as for greater $S_{\max}$ generally. Furthermore, the effect of the environment, Hogeveen [15] also tested in a vacuum, also showed increased surface roughness of the crack surface post-failure. However, the argument can be made that for small crack lengths, and therefore small values of ΔK, the value $\gamma = 1$ is likely close to reality. At that point there is a low likelihood of a significantly rough surface having formed, which is aligned with the effect of lower average stress intensity at the crack front also associated with low R and $S_{\max}$ values.

The shear lip factor increases from one to $\sqrt{2}$ during formation. For a fatigue experiment with a developed shear lip in the crack propagation phase of the Paris curve the value can simply defined as $\lambda \approx \sqrt{2}$. It is likely that a more symmetric load case without shear lip formation, or shear lips only being present in final failure cycles, may allow the assumption that $\lambda \approx 1$.

The final element to the energy balance, as it was presented by Alderliesten [12] and Kuijk [13], is the plastic energy dissipation term. This term was defined rather straight forward as a function of the plastic strain energy density and plastic volume. This term from Equation 2.12 can be defined with respect to a crack increment by the addition of the term da/dN:

$$\frac{dU_p}{dN} = \frac{dU_p}{da}\frac{da}{dN} = \frac{dU_p}{dV_p}\frac{dV_p}{da}\frac{da}{dN} = \frac{dU_p}{dV_p}\frac{dA_p}{da}\frac{da}{dN} \cdot T \tag{2.16}$$

With this final element defined with a choice of plastic zone radius or another volumetric formulation that is proportional to the crack length, the energy balance can be defined. The cycle dependent variety of the energy balance is a combination of Equation 2.11 and Equation 2.12, such that with da/dN factored out:

$$\frac{dU}{dN} = \frac{dU}{da}\frac{da}{dN} = \left[\frac{dU_{\mathrm{a}}}{da} + \frac{dU_{\mathrm{p}}}{da}\right]\frac{da}{dN} \tag{2.17}$$

This new cycle dependent description of the dissipated energy balance can be filled in with Equations 2.15 and 2.16 to yield a general energy balance [12] [13].

$$\frac{dU}{dN} = \left[2 \cdot \frac{dU_{\mathrm{a}}}{dA}\gamma\lambda T + \frac{dU_p}{dV_p}\frac{d}{da}\left(A_p T\right)\right]\frac{da}{dN} \tag{2.18}$$

This relation describes the change in energy dissipated as a consequence of crack growth rate with respect to cycles. This is a powerful relationship that has been established, representing a descriptive model of the energy dissipation as a function of the crack growth rate. The following subsection 2.3.2 will dive into a methodology to convert this limited descriptive energy dissipation model into a predictive framework for the purpose of predicting the fatigue behavior of a metal based on the energy balance given by Equation 2.18.

As a first step in this process, a discretized version of the above differential equation should be considered for numerical modeling. This is given by Equation 2.19 below.

$$\text{Discrete Energy Balance:} \quad U(a+\Delta a) - U(a) \approx \left[\frac{dU_{\mathrm{a}}}{dA} \cdot 2\gamma\lambda T + \frac{dU_p}{dV_p}\frac{dA_p}{da} \cdot T\right]\Delta a \tag{2.19}$$

Lastly, there is a limitation to the presented quantification of the energy balance as a consequence of crack growth. Namely, that we are dealing with a causality issue calculating the energy dissipation from the crack growth, as Equation 2.18 describes the energy that must be dissipated as a consequence of a crack length increment. If used for as a predictive model with an input of da/dN we are calculating the resulting dissipated energy due to the increase in free surface and plastic zone associated with the increment in crack length. Consequently, the importance of attaining an accurate description of the plastic zone and energy release is critical to gather useful results from an approach employing this rendition of an energy balance framework. The coming sections in this literature review will deal with further frameworks using energy based predictive methods followed by a more detailed overview of existing plastic zone estimations.

2.3.1. A Tuned Plastic Energy Density

Before delving deeper into the Sliding box predictive framework and energy term approximations, the original formulation for the plastic energy density dU_p/dV_p can be reviewed as it was derived from experimental data by Kuijk [13]. This value is a prerequisite to define the energy captured in the plastic energy dissipation. This aspect can be defined as the strain energy density of the non-elastically deformed material ahead of the crack tip. Two aspects complicate the estimation of this value, those being the additional elastic energy that is stored in and around plastically deformed zones as well as the work hardening that can occur past the yield point in non elastic-prefect-plastic materials. Together these aspects increase the total amount of energy that is trapped or dissipated around the crack tip. Kuijk [13] merged elastic and plastic energy in the plastic zone arguing that the elastic energy storage is significantly smaller than the plastic energy dissipation for constant amplitude loading.

By using the energy balance from Equation 2.18, giving experimental measurements of the change in applied energy as well as crack length as input, the value of the plastic energy density can be extracted. This produced the data shown in Figure 2.3 combining all additional material effects, elastic energy, and plasticity induced crack shielding for a variety of materials. Effectively, this process tunes the entire energy balance to the materials and loading conditions present.

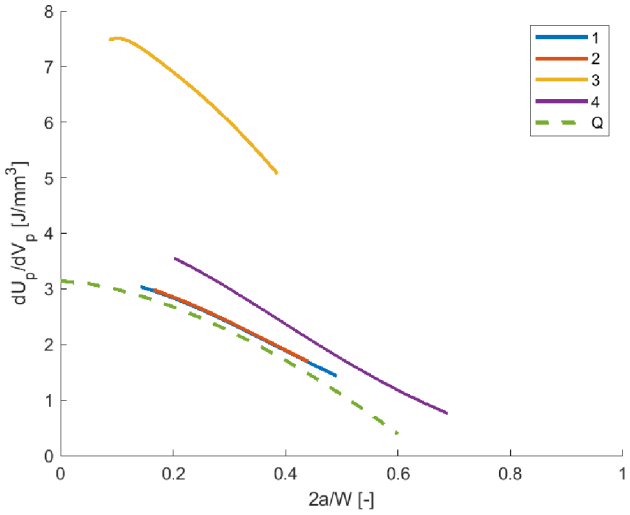

Figure 2.3: Generalized relation for the plastic energy density and effects not otherwise accounted for. Plot is scaled by $(S_y/S_{\max})^2$, which leads to the definition of curve Q, corresponding to Equation 2.20. Lines 1 and 2 refer to 2024-T3 at $R = 0$ and 0.3, respectively. Lines 3 and 4 refer to 7075-T6 at $R = 0.1$ and Fe 510 Nb at $R = 0.5$. Figure taken from Kuijk [13].

This relation given by solving for dUp/dV_p shows a decreasing trend with respect to crack length. Kuijk [13] went on to generalize the observed trend with a decreasing, unit consistent, power law. This power law is dependent on the crack length a, geometric constants, the golden ratio, and a stress level scale factor which was observed to normalize and collapse measured plastic energy densities of metals, aluminum and steel to the power law. The golden ratio is implemented here as a happenstance which closely approximates the slope and curvature of the data plotted on the geometry normalized Figure 2.3.

$$\frac{dU_{\mathrm{p}}}{dV_{\mathrm{p}}} = Q\left(\frac{S_y}{S_{\max}}\right)^2 = \pi\left[1 - 2\left(\frac{2a}{W}\right)^{\phi}\right]\left(\frac{S_y}{S_{\max}}\right)^2 \tag{2.20}$$

An investigation of this aspect may be useful to refine or simply validate the approach, especially since aluminum 7075-T6 tests showed substantial deviation to the proposed law. Although it is unit correct, there is no justified physics based relation between the golden ratio and the plastic energy density in metals. Another source related to the work of Kuijk [13] is Quan [16] who determines that for 7075-T6 the total plastic dissipation per cycle and the plastic dissipation in the reversed plastic zone show a nonlinear relation with $\frac{da}{dN}$ and $\frac{dU}{da}$. The dataset produced for this conclusion is also the same dataset employed by Kuijk [13] for 7075-T6.

Furthermore, changing the materials and testing environment further, will impact the quasi-static mechanical properties, affecting the energy balance. It is possible that when the parameters in a modeling approach differ significantly from those used to produce Figure 2.3, the robustness of the developed golden ratio based power law may break down. An interesting approach may be to vary other parameters in the energy balance to account for these changes in a logical way and improve the presented energy balance.

2.3.2. Sliding Box Analogy for the Energy Balance Approach

As mentioned in the energy summation steps, the next step required to model, the fatigue damage accumulation in a specimen, is a crack growth prediction. This section is wholly based on the work of Kuijk [13], who used an incrementation method based on a sliding box analogy to turn the energy balance into a predictive model. The approach is based on the concept of stiction and friction and models the progression of a crack in a manner similar to how a box moves across a surface under a periodic sinusoidal load. Terms such as stiction, friction, and acceleration are all considered with this analogy. Testing showed good correlation with experimental fatigue curves and is promising for modeling the crack growth rate analytically in different materials based on representative quasi-static mechanical properties.

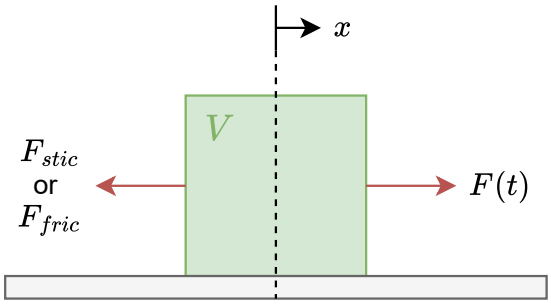

Figure 2.4: Simple sliding box free body diagram

Note that when integrating the general equations of motion the term for acceleration $z \propto F/M$ is used. In this analogy the forcing function is energy based and therefore the mass is analogously replaced with the volume $V = WTL$ of the specimen that can absorb energy, writing instead that $z \propto U/V$. In the same way, instead of applying a regular load to the box to induce movement, the forcing function, $F(t)$, is replaced by the range of applied energy as a squared sinusoidal function of stress, $F(t) \propto S(t)^2$.

The forcing energy function is scaled to the maximum stress with a sinusoidal load as observed in a fatigue experiment load cycle. The function to replicate this is defined as Equation 2.21, which scales the sinusoidal to maximum and minimum applied nominal stress to a period of one second.

$$S(t) = S_{\min} + (S_{\max} - S_{\min}) \cdot \frac{1}{2}(1 - \cos(2\pi t)) \tag{2.21}$$

Then the energy-based forcing function, $F(t)$, can be calculated directly with Equation 2.13 using again the geometry correction factor β to increase the stress intensity throughout cycles, or an energy balance can be employed to calculate the increment in available energy to be dissipated in crack growth by means of the next sliding box analogy loop. The direct method is given by Equation 2.22, and the energy balance indirect iterative approach is given by Equation 2.23. We define for the i^{th} cycle ($i = N$), and the initial state is referred to with the subscript zero

Direct approach:

$$F(t) = \frac{1}{2}\frac{S(t)^2}{E} WTL \cdot \beta(a) \tag{2.22}$$

Indirect energy balance approach:

$$F(t) = \frac{U_{\max,i}}{U_{\max,0}} \left(\frac{1}{2}\frac{S(t)^2}{E} WTL \right) \tag{2.23}$$

where:

$$U_{\max,i} = U_{\max,0} + \sum_{N=1}^{i} \left[\frac{dU}{dN} \right]_{EB,i} \tag{2.24}$$

with:

$$\begin{aligned} U_{\max,0} &= U_{op,E} + (U_{\max,E^*} - U_{op,E^*}) \\ &= \frac{1}{2}\frac{S_{op}^2}{E} WTL + \left(\frac{1}{2}\frac{S_{\max}^2}{E^*} WTL - \frac{1}{2}\frac{S_{op}^2}{E^*} WTL \right) \\ &= \frac{1}{2}\frac{S_{op}^2}{E} WTL + \frac{1}{2}\frac{S_{\max}^2 - S_{op}^2}{E} WTL \cdot \beta(a) \end{aligned} \tag{2.25}$$

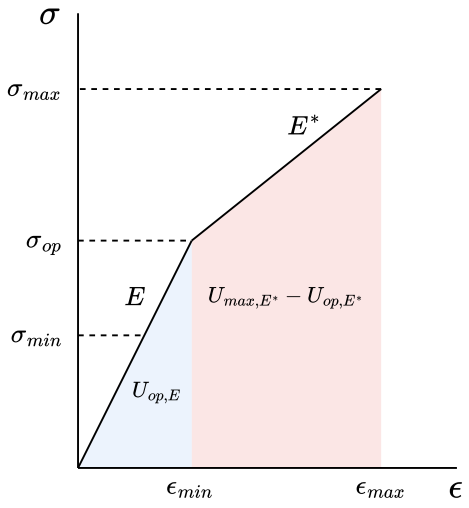

Figure 2.5: Actual energy taken up by a specimen with an opening stress correction and a penalized effective stiffness. Represented mathematically by Equation 2.25

The base initial energy dissipation per cycle is given by $U_{max,0}$ for the indirect approach which is an accurate first guess based on the opening stress correction to the absorbed maximum energy. This

initial value is also used subsequently to scale the forcing function with which makes it a very important initial approximation. To ensure the accuracy of the initial maximum energy, the opening stress correction is based on a bilinear stress-strain curve using energy methods, a visual example of such a curve and of the components of $U_{max,0}$ is given in Figure 2.5. The elastic energy components is given by the area underneath the stress strain curve up until the crack opening stress, S_{op}. Beyond the opening stress, the load is assumed to be distributed over only the material that remains un-cracked resulting in a lower effective stiffness. Finding the energy under the remaining portion of the cycle's stress-strain curve, from S_{op} to $S_{\max}$ is done by the remaining energy term in Equation 2.25. Each of these energies are shown schematically in Figure 2.5, the process of this energy formulation is based on Alderliesten [17].

We've been using a variable for the opening stress thus far without defining it in the first place. The opening stress is covered by a wide range of literature including the author of the sliding box approach in Van Kuijk et al. [18], who compares varieties of phenomenological crack closure corrections. These include some for aluminum such as De Koning [19], Schijve [20], and Elber [21], based in part on the work of Alderliesten [17] to define a physical actual opening stress. The energy based bilinear stress-strain approach used in Equation 2.25 in the presented methodology makes use of the phenomenological opening stress for S_{op} based on the stress ratio $R = S_{\min}/S_{\max}$ as developed from Elber [21] by Schijve [20][8].

$$\left.\frac{S_{op}}{S_{\max}}\right|_{\text{Schijve}} = 0.45 + 0.22R + 0.21R^2 + 0.12R^3 \tag{2.26}$$

In cycles following the first one, the crack growth is then calculated as a function of the ratio $U_{\max,i}/U_{\max,0}$ making use of the spring energy formulation again to determine the squared sinusoidal energy absorption function, $F(t)$ for the energy balance. Every time the sliding box analogy is iterated for another load cycle, the sliding box analogy must be run based on the energy forcing function defined above, and the equations of motion as well as the stiction threshold, shown in Figure 2.6, from Equation 2.27. Since stiction and friction are the principal that this methodology uses to describe the loading and propagation of a crack plane, these two variables must also be defined to modify the forcing function based on whether or not the imaginary box is sticking or moving. To account for the opening stress in the energy balance the force of friction and stiction are defined as follows:

$$\begin{aligned} F_{\text{fric}} &= C_{\text{fric}}\, U_{\max}(a=0) = \tfrac{S_{op}}{S_{\max}} U_{\max,0} \\ F_{\text{stic}} &= C_{\text{stic}}\, U_{\max}(a=0) = 0.99999999 \cdot U_{\max,0} \end{aligned} \tag{2.27}$$

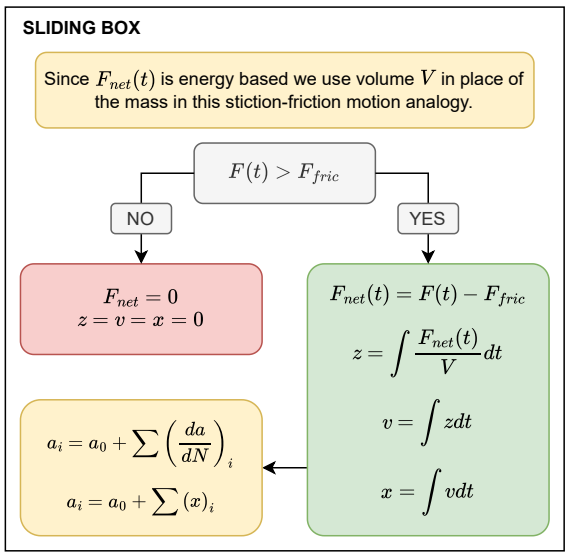

Figure 2.6: Overview of the relations applicable to the sliding box analogy in a flow diagram block

Overall, this analogy has the potential to provide a novel, physically grounded, framework for modeling crack growth. But, several aspects remain unclear or could be refined. In the indirect energy balance implementation of the sliding box analogy, the forcing function is scaled to the applied stress range $S_{\min}$ to $S_{\max}$. However, given that Kuijk [13] defines the friction component in terms of physically meaningful parameters such as the opening stress, it is not evident why the stiction term is treated as a constant. In particular, it is questionable whether a value of $F_{\text{stic}} = 0.99999999$ represents a realistic analogy, since it implies that crack propagation effectively occurs only at the maximum load and during unloading, which may not accurately reflect the continuous nature of fatigue crack advance over the loading cycle. Furthermore, the friction force, as it was defined [13] is based on the opening stress corrected initial energy term $U_{max,0}$. This energy value is then multiplied with the opening stress correction from Equation 2.26 again which stands out as a double-use of a similar correction. This may work for scaling the value of $U_{max,0}$ with a factor below unity but the physical base for this assumption is not clear.

2.3.3. Griffith Energy Range as an Approach to the Energy Balance

An approach to the energy balance to estimate fatigue crack propagation by Bian and Taheri [11] makes use of the Griffith linear-elastic energy principle to define the crack surface energy and plastic-elastic energy dissipation terms. They begin by expressing the energy balance from Equation 2.11 as,

$$G_{cr}db = G_{\max}db + G_{cr}dr_p \tag{2.28}$$

They argue that taking into account the stress range in the stress intensity factor creates a cycle dependency for G_{max} given by Equation 2.30 with ΔG_{max} based on $\Delta K = \Delta S\beta\sqrt{\pi a}$. The original equations were given in terms of Mode I and II loading (opening and shear modes) but since the focus of the investigation is for Mode I (pure opening), the following relationship for G_{max} has been simplified as such. Therefore, the following relations are given in terms of $K = K_I$.

$$G_{\max} = \frac{K^2}{E'} \tag{2.29}$$

$$\Delta G_{\max} = \frac{\Delta K^2}{E'} \tag{2.30}$$

where:

$$E' = \begin{cases} E & \text{for plane stress} \\ E/\left(1-v^2\right) & \text{for plane strain} \end{cases} \tag{2.31}$$

The change between the stress intensity factor based on the cyclic stress range, as it is implemented above, is how the relation changes from static to cyclic and is used to determine values of $G_{\max}$ per cycle. A similar analysis was made by Kuijk [13] who quantifies the energy absorbed by a specimen per cycle based on Hook's law instead but uses the stress range for cyclic analysis as well. Furthermore, the value of the maximum SERR defined above is also unit consistent and is employed as such for the determination of da/dN

$$\dim \Delta G_{\max} = \frac{(\mathsf{Pa}\sqrt{\mathsf{m}})^2}{Pa} \rightarrow \frac{\mathsf{kg}}{\mathsf{s}^2} \rightarrow \frac{\mathsf{J}}{\mathsf{m}^2} \tag{2.32}$$

First, on the topic of estimating plastic energy density, Bian and Taheri [11] equated the plastic storage energy to the product of the critical energy release rate G_{cr} and the increase in plastic zone size dr_p. The argument is made that since fracture happens at this energy level, the plastic zone should also approach this critical SERR value throughout, quantifying

$$G_{cr} = \frac{K_C^2}{E'} \tag{2.33}$$

This allows the expression of an infinitesimal change in crack length based on an energy balance as a function of the SERR, the critical SERR, and a term equal to the plastic zone growth in the direction of crack travel θ_0:

$$\begin{aligned} da &= \frac{G_{cr} f'\left(K, \theta_0\right)}{\left(G_{cr} - G_{\max}\right)\, S_y^2} \\ &\text{where:} \\ dr_p &= \frac{f'(K, \theta)}{S_y^2} \end{aligned} \tag{2.34}$$

The direct determination of $\frac{da}{dN}$ is then given directly with respect to the plastic zone growth dr_p as a function of ΔK and the crack growth direction θ_0. Thanks to the implementation of stress range in ΔK as described, Equation 2.34 is made cycle dependent in Equation 2.35 and creates a relation for the crack growth rate directly.

$$\frac{da}{dN} = \frac{G_{cr} dr_p\left(\Delta K, \theta_0\right)}{\left(G_{cr} - \Delta G_{\max}\right)} \rightarrow \dim \frac{da}{dN} = \mathsf{m} \tag{2.35}$$

This approach comes with some limitations, as Bian and Taheri [11] don't actually define an energy density per unit volume but instead the energy dissipation due to plasticity is defined with respect to a unit length. At the same time this energy per unit length of plasticity growth is also constant, defined as the critical SERR from Equation 2.33. The assumption that this energy term is constant with crack length has been shown to be incorrect by Quan [16] complicating this approach. Additionally, using the Griffith energy principle is limited to linear-elastic cases with perfect plasticity in the plastic zone definition, increasing plasticity and ductility, as could be realistically expected for material or environmental variation, would cause these assumptions to break down further.

2.3.4. Additional Plastic Energy Density Estimation

One more relevant alternative to define the plastic energy density by itself has been outlined by Stephenson [22] who quantifies the strain energy density W_o in a uniaxial case from the unloaded state as Equation 2.36. This approach is much more general and computationally complex. However, assuming a stress field such as that proposed by Irwin [23] [24] [22] in Equation 2.37, it may be possible to evaluate the elastic and plastic energy in the plastic zone using a parametric stress-strain curve.

$$W_o = \int_0^{\varepsilon} \sigma d\varepsilon \tag{2.36}$$

$$\begin{aligned} \sigma_1 &= \frac{K_I}{\sqrt{2\pi r}} \cos\frac{\theta}{2}\left[1 + \sin\frac{\theta}{2}\right] \\ \sigma_2 &= \frac{K_I}{\sqrt{2\pi r}} \cos\frac{\theta}{2}\left[1 - \sin\frac{\theta}{2}\right] \end{aligned} \tag{2.37}$$

The stress distribution at the crack tip that is evaluated can also be based upon Equation 2.37 or based on experimental data, making this approach to defining the plastic energy density applicable to the energy balance model as well as experimental analysis.

2.4. Plastic Zone at the Crack Tip

Broek [7] states the plastic zone at the crack tip plays a crucial role in fatigue crack propagation. It represents the region where plastic deformation occurs due to localized stress exceeding the yield strength of the material. The size and shape of this zone depend on whether the state of stress is classified as plane stress or plane strain. Under plane stress conditions, which typically occur in thin materials, the plastic zone is relatively large, allowing greater energy dissipation and potentially slowing crack growth relatively. Conversely, under plane strain conditions found in thicker materials, the plastic zone is smaller, leading to higher crack growth rates due to increased constraint and stress concentration, assimilating more brittle behavior [6].

2.4.1. Irwin Plastic Zone

Irwin's circular plastic zone model provides an approximation for the plastic deformation region surrounding a crack tip in linear elastic fracture mechanics (LEFM). The model assumes that the plastic zone forms a circular shape around the crack tip and helps account for energy dissipation due to plasticity.

The size of the plastic zone is estimated using the stress intensity factor K and the yield strength S_y of the material. In plane stress conditions the plastic zone radius may be given by Equation 2.38. In plane strain conditions the radius is smaller due to higher effective yield strength as given by Equation 2.39. This means that the plastic zone is larger in thin materials (plane stress) and smaller in thick materials (plane strain) due to increased constraint, leading to different fracture behaviors. [23][7]

$$r_p = \frac{1}{2\pi}\left(\frac{K}{S_y}\right)^2 \text{ plane stress} \tag{2.38}$$

$$r_p \approx \frac{1}{6\pi}\left(\frac{K}{S_y}\right)^2 \text{ plane strain} \tag{2.39}$$

Since plastic deformation extends the region affected by stress concentration, Irwin introduced a stress intensity correction factor to the crack length to account for this effect. The apparent crack length is adjusted as $a_{\text{eff}} = a + r_p$, where a is the actual crack length. This correction improves the accuracy of fracture toughness predictions by considering the effects of plasticity and is based on the Von Mises criterion in the line of crack propagation direction [24][23].

The circular plastic zone plays a crucial role in energy dissipation and fracture behavior. In brittle materials, the plastic zone is small, and cracks propagate rapidly, leading to sudden failure. In ductile materials, a larger plastic zone allows for stress redistribution, which delays crack growth and enhances fracture resistance. The dependence on K and S_y makes this model approachable and useful for further analysis. A drawback of this plastic zone is that it is heavily idealized based on the stress distribution along a line in the direction of crack propagation and therefore is a constant radius circle.

2.4.2. Dugdale Strip Yield Model

Wang [6] and Broek [7] summarize the work of Dugdale and Barenblatt. Their strip yield model provides a framework for representing the finite plastic zone that develops ahead of a crack tip in a ductile, perfectly plastic material under plane stress conditions. Instead of allowing an elastic stress singularity at the crack tip, the model assumes that a slender plastic zone of length ρ, acting like an fictitious crack tip extension, forms ahead of each crack tip. Within this zone the material yields at a constant stress equal to the uniaxial yield strength S_y. The plastic zone carries a closure stress that counteracts the applied loading such that the total stress intensity factor at the end of the plastic zone equals zero. This condition removes the classical $1/\sqrt{r}$ singularity and introduces a new effective crack length $c = a + \rho$.

To express this formally, the physical crack of length $2a$ is represented as an effective crack of length $2c = 2(a + \rho)$, with cohesive stresses acting across the yielded strip. The requirement that the net Mode I stress intensity factor vanish at $x = c$ is written as

$$K_\sigma + K_{S_y} = 0 \tag{2.40}$$

where K_σ is the stress intensity factor due to the remote tensile stress σ, and K_{S_y} is the opposing contribution generated by the cohesive stresses within the strip. Under plane stress, the applied remote stress produces

$$K_\sigma = \sigma\sqrt{\pi c} \tag{2.41}$$

Evaluating the stress intensity factor associated with the closure stress distribution leads to the classical Dugdale relation

$$\frac{a}{c} = \cos\left(\frac{\pi\sigma}{2S_y}\right) \tag{2.42}$$

which may be rearranged to obtain the plastic zone length

$$\rho = c - a = a\left[\sec\left(\frac{\pi\sigma}{2S_y}\right) - 1\right] \tag{2.43}$$

For small values of the stress ratio σ/S_y, where we can assume small scale yielding, a series expansion of the secant function gives the approximation

$$\rho \approx \frac{\pi}{8}\left(\frac{K}{S_y}\right)^2 \text{ for plane stress} \tag{2.44}$$

showing that the Dugdale plastic zone radius – technically a diameter – is comparable to, but slightly larger than, Irwin's estimate. Specifically, about $\pi^2/8 = 1.234$ times larger than Irwin.

Overall, the Dugdale model replaces the crack-tip stress singularity with a cohesive zone that sustains stresses up to σ_y. By imposing a closure condition on the total stress intensity factor and ensuring displacement compatibility across the yielded strip, the model captures the essential features of crack-tip plasticity in thin, ductile materials under plane stress, without requiring a full nonlinear analysis. It does however imply that the assumptions of linear elasticity are replaced with those of an elastic-plastic, singularity free, interaction in Dugdale's approach making it more generally applicable.

Both Irwin and Dugdale work with the assumption of perfect-plastic yielding but differ on the assumptions concerning the strain field. Irwin relying on the linear elastic assumptions and a strain field based on the stress intensity factor K while Dugdale enhances the assumptions with a cohesive zone and balancing stress states. A key criteria for linear elastic behavior is small scale yielding where $\sigma/\sigma_y << 1$ which may be true for both models in many fatigue cracks, but the main advantage of Dugdale is the lack of stress singularities and applicability to large scale yielding as well.

2.4.3. Yield Criterion Approach

Having looked at Irwin and Dugdale's approaches to the plastic zone, it is evident that they are primarily based on different levels of assumptions concerning the stress field around a crack tip. Based on linear elastic assumptions as in Irwin's approach it is possible to define more physically accurate plastic zones based on a two dimensional expansion of the stress intensity factor, given in the principal stress directions in Equation 2.37 [24] [7]. This enables the analysis through traditional yield criteria to develop a mathematically refined plastic zone approximation.

One of these yield criteria is the Von Mises criterion, with this relation it is possible to determine the the yielded zone of the stress distribution from Equation 2.37. An interesting note here is that the zone radius along the crack propagation direction, $\theta = 0$, correctly recovers the Irwin plastic zone as it uses the same Von Mises criteria just in one dimension [23] [24].

$$\text{Von Mises Criterion:} \quad (\sigma_y - \sigma_z)^2 + (\sigma_z - \sigma_x)^2 + (\sigma_x - \sigma_y)^2 + 6\left(\tau_{yz}^2 + \tau_{zx}^2 + \tau_{xy}^2\right) = 2\sigma_{vm}^2 \tag{2.45}$$

$$
\begin{aligned}
r_1(\theta) &= \frac{K^2}{2\pi S_y^2}\left[1 + \frac{3}{2}\sin^2\theta + \cos\theta\right] \quad \text{plane stress} \\
r_1(\theta) &= \frac{K^2}{4\pi S_y^2}\left[\frac{3}{2}\sin^2\theta + (1-2v)^2(1+\cos\theta)\right] \quad \text{plane strain}
\end{aligned}
\tag{2.46}
$$

An overall comparison of normalized plastic zones is given in Figure 2.7, demonstrating that due to their normalized size and shape variations they also vary in volume and rate of growth for a crack increment. The normalization of the plastic zones is important for this comparison to evaluate these definitions on the same scale without other effects.

In this comparison it is assumed that the Dugdale model may also be used as a circular plastic zone, while this does not align with the initial definition of the Dugdale radius, it presents a middle-of-the-road case, between Irwin and Von Mises, based on a different set of base assumptions. Additionally, for area comparison, another yield criterion approach is shown in Tresca from the definition for a constrained plane strain state by Sun and Jin [24].

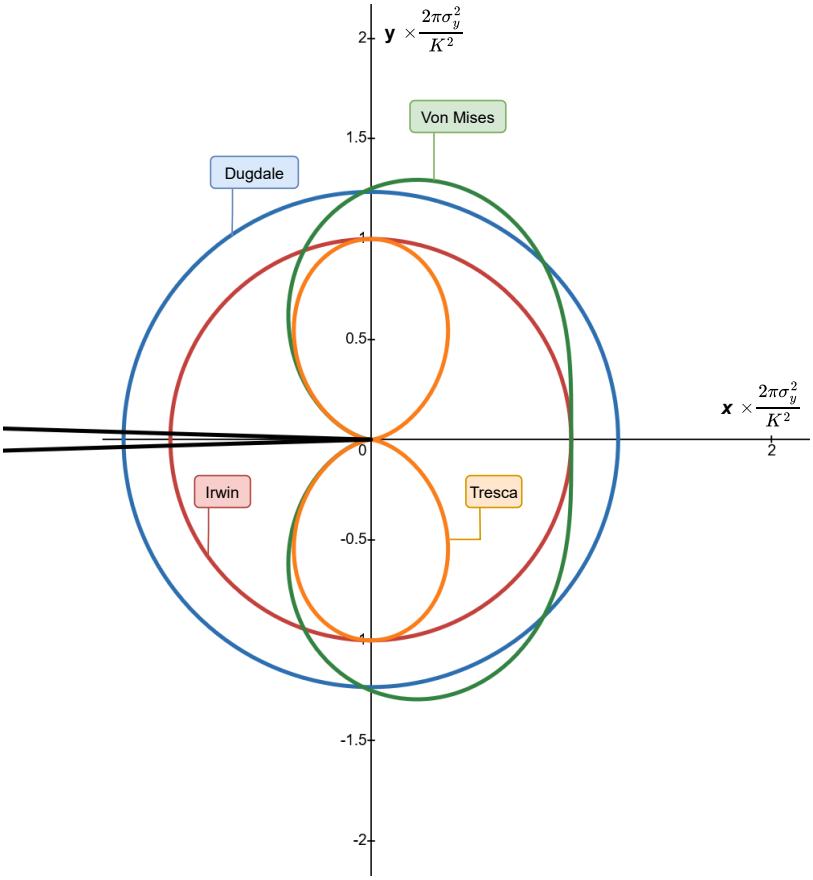

Figure 2.7: Comparison of plastic zones normalized with a factor $2\pi S_y^2 K^{-2}$.

2.5. Low and Cryogenic Temperature Effects

According to Duthil [25], at cryogenic temperatures, metals experience significant changes in mechanical properties. In most structural materials, both yield strength and ultimate tensile strength rise as temperature decreases. The extent of this increase ranges from approx. 10% in certain metallic alloys to more than 100% in some polymer-based materials [26]. This temperature-dependent strengthening is generally attributed to diminished thermal activation within the crystal lattice, which restricts dislocation mobility and thereby elevates the material's resistance to deformation.

In material tests at varying temperatures presented by Duthil [25] the elastic response shows a clear dependence on thermal conditions. The modulus of elasticity (Young's modulus) exhibits a slight increase at low temperatures, indicating higher stiffness as thermal motion is reduced. At elevated temperatures, however, Young's modulus decreases due to increased thermal excitation, which facilitates atomic movement and reduces the effective stiffness of the material. The effect on elastically stored strain energy with decreasing temperature may decrease due to the stiffening effect.

The plastic and ductile behavior is strongly governed by crystal structure. Materials with a face-centered cubic (FCC) lattice, such as Cu–Ni alloys, aluminum alloys and austenitic stainless steels, retain significant ductility even at low temperatures and therefore provide a greater margin of safety even beyond the yield point. This combination of strength and low-temperature ductility makes FCC alloys particularly suitable for cryogenic applications. The elastic and plastic strain energy absorbed by an FCC lattice material is consequently increased by the support of greater amounts of deformation.

In comparison, body-centered cubic (BCC) materials, including ferritic steels and carbon steels, undergo a ductile-to-brittle transition as temperature decreases. Below this transition temperature they lose plasticity and become susceptible to brittle fracture. Consistent with this behavior, fracture toughness, which relates to the resistance to crack initiation and growth, generally decreases with decreasing temperature. Titanium and its alloys can likewise exhibit increased yield strength but reduced toughness at low temperature due its hexagonal packed lattice structure. FCC materials tend to maintain comparatively higher fracture toughness under these conditions due to the observable increase in ductility and ultimate strength, observable in Figure 2.8 [25] [26].

The strength response follows a complementary trend. Yield strength increases at low temperatures, so materials can sustain higher tensile stresses before the onset of plastic deformation. This increase in yield strength is accompanied by a higher resilience modulus, which implies that more elastic strain energy can be absorbed before yielding occurs. However, the concurrent loss of ductility in BCC materials at low temperatures partially offsets the benefits of higher strength from a fracture and damage tolerance perspective. Reduced energy dissipation in the vicinity of cracks, combined with the inherently brittle response of BCC structures in the low-temperature regime, renders these materials more vulnerable to rapid crack propagation [25].

These temperature-dependent behaviors have direct implications for the design and material selection of cryogenic systems. In practice, alloys with FCC crystal structures are preferentially selected for components operating at very low temperatures because their combination of retained ductility, relatively high fracture toughness and predictable strengthening response under cooling is critical for structural integrity. Such materials are therefore widely adopted in aerospace structures, cryogenic propulsion systems, cryogenic storage tanks - such as those for hydrogen - and superconducting applications where reliable performance under severe thermal conditions is essential.

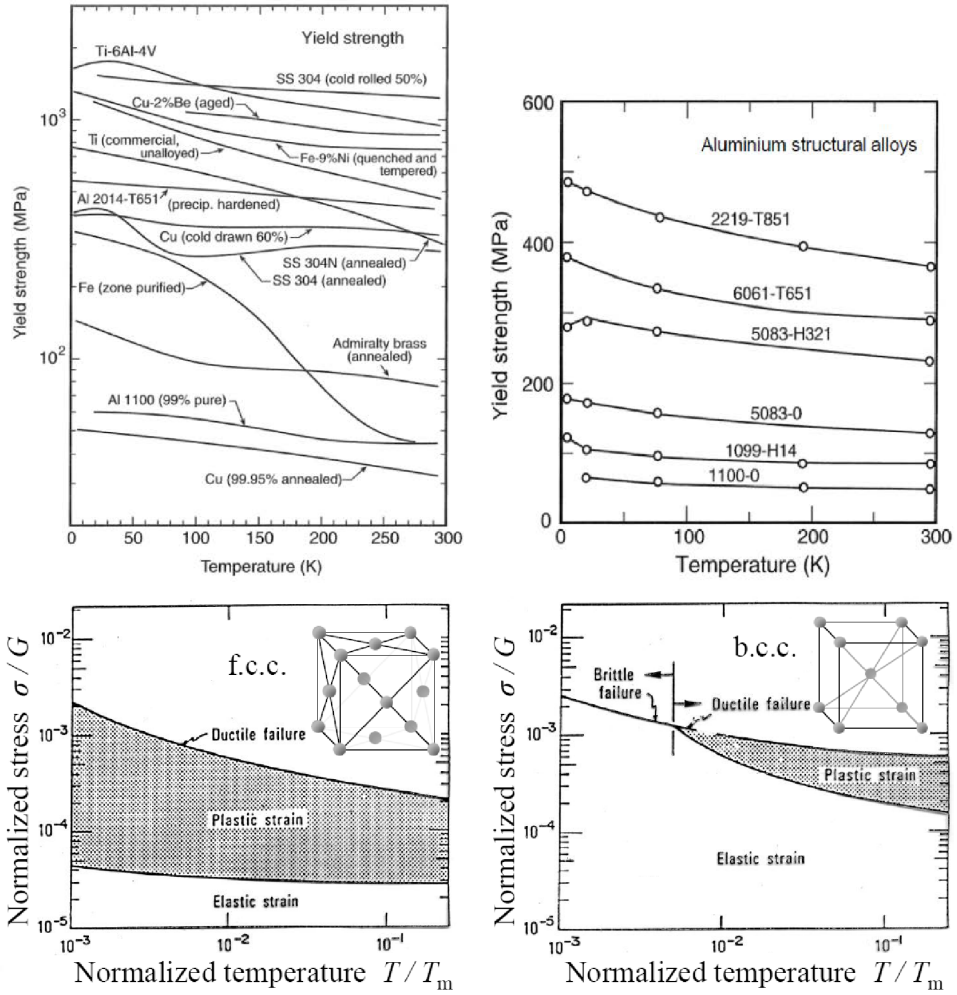

Figure 2.8: An overview of low temperature effects on yield strength and ductile behavior of various metals and metallic lattices. Stress is normalized by the shear modulus G. [25]

The effects described up to this point indicate that FCC materials including aluminum are most suitable to low temperature, so below freezing and including cryogenic, fatigue applications. Figure 2.8 taken from Duthil [25] shows in general the changes to mechanical properties at low temperatures for a wide range of materials. Focusing on aluminum, it is evident that the proportion of plastic strain before failure increases the lower the temperature is below the melting temperature, T_m. As a consequence so does the failure stress and, to a lesser extent the yield strength. Among the tested aluminum alloys the greatest increase is seen in 2XXX and 6XXX aluminum alloys without displaying a drop off close to absolute zero.

The greatest increase in yield strength is actually seen in iron, steel, and stainless steels. But, the BCC plot of normalized temperature versus normalized stress clearly shows the ductile-to-brittle transition temperature in the range $T/T_m < 10^{-2}$. As mentioned, this offsets the observed increase in elastic performance by nullifying the post yield regime and associated strain energy absorption ability.

3

Research Approach

Thus far, we have found a problem case in the introduction highlighting the cryogenic storage of liquid hydrogen driving the demand for new fatigue analysis methods for low temperature storage tanks and adjacent structures. The benefit of avoiding resource intensive controlled environment testing is substantial and predictive alternative models are promising.

In the literature review we have observed the simplicity but test-dependence of empirical software and Paris-law approaches as well as the predictive energy-balance framework using a sliding-box stiction/friction analogy. The consequence of low temperatures on aluminum alloys was determined to increase yield and ultimate strength as well as strain hardening and ductility, making this an optimal material for low temperature fatigue applications. To account for the variation in mechanical properties a variety of alternate definitions for the plastic zone were defined from literature which can be used to modify the energy balance's plasticity term.

Now, with an outline of relevant literature and theory concerning the energy balance approach to fatigue damage growth modeling, a method shall be determined to investigate the validity of applying this novel physics based model. Firstly, this chapter will delve into the exact research questions, objectives, and hypothesis that relate to this task. Secondly, the elements of the energy balance and constants of the sliding box analogy will be evaluated. Next, focusing on mechanical property related material variations, as well as the cold environment, component in an experimental study will result in comparison data. Finally, an analysis of the plastic zone related energy dissipation terms will be outlined and related to the experimental data collection.

Before continuing with the research objective and questions, the term "cold environment" and "low temperature" must be defined for the remainder of this thesis. The term "low temperature" will refer to temperatures below $0°$C (273K) which includes cryogenic temperatures [4] below $-150°$C or 120K. The term "cold environments" will be used almost interchangeably for the same low temperatures, but with an emphasis on the accompanying environmental conditions that may exist, in a climate chamber for example. The reason the temperature range is kept so large is that the mechanical material properties are monotonically increasing with decreasing temperature [25]. This implies that results at temperatures such as $-30°$C, in comparison with $21°$C (294K) room temperature, are likely to be indicative for the trends observed at cryogenic temperatures.

3.1. Research Objective and Questions

As stated above, from the literature review, we have learned the necessary background to formulate a research objective and a methodology in detail. The research objective is to expand and validate the application of a physics based energy balance with the sliding box analogy for modeling fatigue damage propagation at low temperatures by reviewing the energy balance and comparing the model to a range of varied experimental data. The following research questions have been defined as a result of the literature review and objectives for the outlined methodologies involved.

1. To what extent can a physics-based sliding box analogy approach to crack propagation capture the fatigue characteristics of aluminum metals at low temperatures?
   (a) How can stress range, material variations, and thickness effects at room temperature lead to conclusions about the validity of Van Kuijk's [13] energy balance with sliding box approach at low temperatures?
   (b) What effect does a low temperature environment have on aluminum in the context of quasi-static mechanical properties for fatigue loading?
2. To what extent can the plastic zone size and energy storage of a crack tip in aluminum be defined by using quasi-static mechanical properties at room temperature and $-30°$C?
3. To what extent do the fundamental assumptions made in the physics-based energy balance with sliding box analogy model agree with low temperature fatigue?

Evidently, these questions originate from the application of the predictive energy balance application to modeling fatigue damage growth. The literature review determined that the way Kuijk [13] defined the plastic energy dissipation term, including the function for dU_p/dV_p, is likely not going to account for the higher degree of plasticity and energy dissipation in low temperature fatigue. For this reason, this term is investigated specifically with reference to the plastic zone and, as a consequence, its energy storage. For this, a variety of alternate definitions were found, including Irwin, Dugdale, and yield criteria based approximations.

Additionally, an objective is also to gain insight into the extent of the model's validity as a reliable and transferable predictive tool for the application at low temperatures environments. This relates to the potential application to structural engineering in cryogenic conditions. The research questions mention changes in variables including thicknesses, stress range, and material which should all be accounted for in the energy balance and sliding box analogy.

3.2. Hypotheses

Let us now define some hypotheses based on the information gathered thus far for each research question. After presenting the methodology and results, these hypotheses will be reviewed again and compared to the testing and modeling outcomes. The numbering of the hypotheses will be matching the research question being answered.

1. Overall, the sliding box analogy combined with the defined energy balance is expected to capture the fatigue characteristics of aluminum only to a limited extent. The extent will likely be limited by the energy balance's accuracy as the amount of energy absorption in the post yield regime will be higher than expected.
   (a) The energy balance is expected to take into account the variation in stress ratio, material-related quasi-static properties, and the thicknesses. Based on the difference between predicted and measured crack growth rates, the extent of validity of the model when faced with similar variations caused by low temperature will be discernible.
   (b) At the low temperatures reached in testing, an aluminum alloy shall experience an improvement in yield strength as well as ultimate strength. Additionally, the amount of deformation before final failure will increase and the elastic stiffness increase will be insignificant.
2. The size of plastic zone size can be estimated analytically to determine the plastic energy storage, through the implementation of an energy density term, to a partial extent.
3. The assumptions made by Kuijk [13] will agree with fatigue tests at low temperature to a very limited extent due at least in part to the elastic-perfect-plastic assumptions of the plastic energy dissipation term.

3.3. Limitations of Validity on the Proposed Research

To confine the scope and honor resource constraints on this thesis, some of the following will not be given further attention after the previous chapters, even though they may occur to the reader. Hydrogen corrosion and other material effects resulting from the presence of hydrogen [5] will not be directly investigated but have been acknowledged as potential influences on fatigue behavior in cryogenic use cases. Thermodynamic analysis will not be developed; instead, the model will be based on broader physical principles outlined by Kuijk [13], with energy dissipation estimated using strain fields and quasi-static stress-strain response. Non-thickness-related geometric effects will be minimized by experimental design but not accounted for further than by finite width and standard geometry correction factors.

Crack initiation, nucleation, and final failure will not be explicitly modeled but final failure will be represented in the experimental datasets; conclusions on this aspect will be made. Opening stress corrections will be adopted from existing studies, such as Schijve [8], in relevant applications. Input data for the physics based model from elastic-plastic FEA simulations or other advanced sources will not be considered, with the model explicitly relying only on common engineering constants, which can be determined with a quasi-static tensile material test.

Finally, the minimum achievable temperature with the available testing methods is $-50°$C. In order to observe trends from the test environment with decreasing temperature, the difference to room temperature shall be maximized with a maximum temperature of $-30°$C being allowable. Furthermore, the deviation in test temperatures both at room and low temperatures shall be no more than $\pm 3°$C to ensure a realistic consistency between the material characterization and the fatigue tests.

3.4. Approaching the Problem

In order to reach any conclusions on the low temperature validity of the sliding box model based on an energy balance, it is necessary to devise a testing methodology. The response of the model to changes in the energy balance should be evaluated, and a variety of tests in consistent environments and consistent setups should provide a basis for analysis of the effect of property, geometry, and temperature variations on the predictive capacity of the model.

From the presented research questions (RQ), each should be answerable based on the results of the presented methodology in chapter 4. Relating to RQ 1, an experimental testing campaign relating to the variations mentioned by RQ 1a will help reach conclusions on the extent to which the model can capture the effects of a cold environment. This includes fatigue tests as well as quasi-static tests for property determination in the same environment and thickness as the corresponding fatigue specimen. The tests at room temperature ($21°$C) mentioned by RQ 1a can be enhanced with a test at a low temperature ($-30°$C) for more model-to-data comparison.

Next, the expected material properties at low temperatures in aluminum alloys, mentioned in RQ 1b, can be compared to experimental data using a quasi-static tensile test. Together, the data collected in relation to RQ 1a and 1b will yield crack growth rates and properties necessary to compare and confirm the predictive performance of the energy balance with the sliding box analogy for low temperature applications.

The model as described by Kuijk [13] can be modified with variations to the plastic energy terms relating to RQ 2. This results in a point of comparison showing the sensitivity and quality of the model depending on the chosen plastic zone approximation. The plastic zone can also be monitored during experiments as a further point of comparison.

Lastly, the results of all the models and experiments can be post-processed, and visible trends broken down to find answers relating to RQ 3. Based on the outcome from these tests and comparisons, it will be determined whether the changes observed due to varying alloy-related properties, thickness effects, and temperature effects show evidence of the energy balance based sliding-box analogy being valid also at cryogenic temperatures. A further outcome of the methodology may be the discovery of tuneable elements to the energy balance that improve the quality of prediction, such as the plastic zone.

4

Methodology

4.1. Theoretical Changes to the Energy Balance Model

Firstly, the application of the energy balance combined with the sliding box analogy, from now on labeled as the EBSB, needs to be defined for the application in this methodology. The code basis in MATLAB of Kuijk [13] is used and modified to represent the conditions and geometries of the tests described later in this section. An overview of the numerical process of the employed modeling simulation originally written by Kuijk [13] is given in Figure 4.1.

The model as it was also outlined in section 2.3 and subsection 2.3.2 can be used as a baseline to compare against experimental data. Subsequently though, the validity can be investigated by making changes to the currently arbitrarily defined sliding box analogy constant F_{stic}, as well as the plastic zone assumptions. These changes can be used to better understand the influence of characteristics such as yield and ductile properties, as well as low temperatures. If the model can be improved theoretically, with respect to collected data, while maintaining the physics based methodology it would show evidence that the EBSB is valid in the tested conditions. In the next subsection, the possible variations to the EBSB model are reviewed or defined.

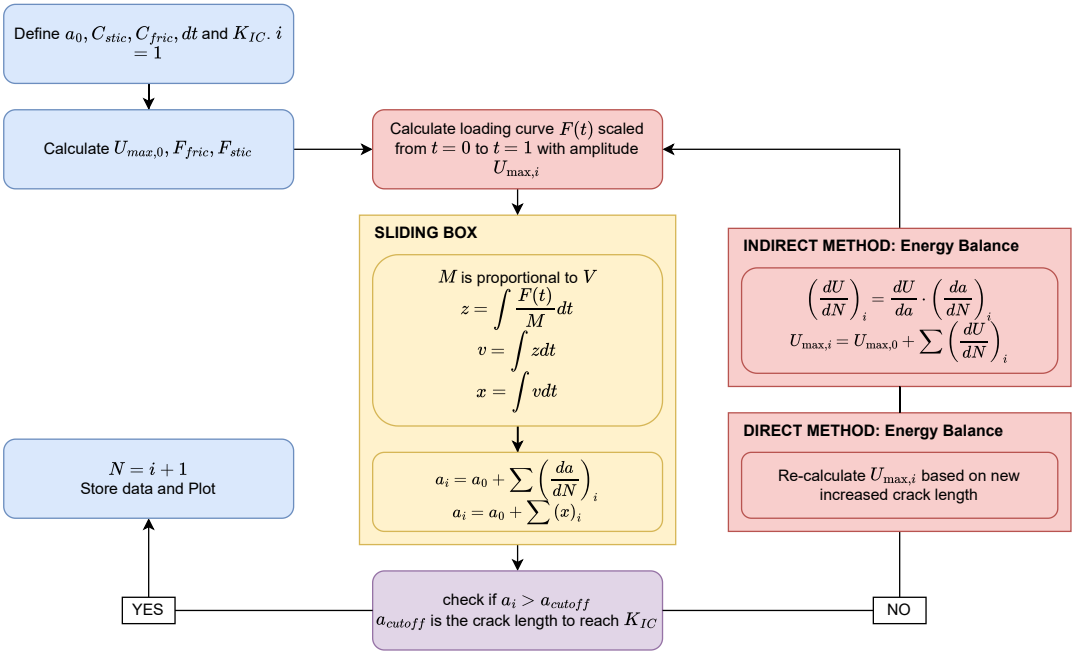

Figure 4.1: Complete overview of the EBSB application based on the MATLAB implementation of Kuijk [13]

4.1.1. Testable Building Blocks of the Model

The theoretical changes to the plastic zone that are being focused on can be implemented with the alternative methodologies from literature as will be outlined in subsection 4.1.2. Since the energy balance with sliding box analogy will be compared to experimental data to determine its extent of validity, an important step here is to choose modifications that will likely align with the collected data. The following building blocks will receive modifications;

1. Shear lip correction will be $\lambda = 1$
2. Constants of the sliding box analogy, specifically F_{stic}
3. Plastic volume will be modified by varying the plastic zone radius in the volume calculation. The variations will be a change from the original Irwin plastic radius to the Dugdale zone radius, and a comparison to a Von Mises yield criteria based plastic zone.

Concerning the assumption that $\lambda = 1$, the modifications of both λ and γ are trivial in the EBSB simulation. Therefore, they will initially be set to unity to ensure that in comparisons of any experimental results to modeling results, the variations due to the plastic zone approximations will be isolated. If the observations from final failures indicate that either correction should be adjusted to represent the real fracture conditions, then the values can be reviewed as a result.

The experimental data will first be compared to the unmodified EBSB model. Then the effect of changing the sliding box constants will be investigated. The listed varieties of the plastic zone estimations will be implemented in the energy balance, and their effect analyzed to determine if each improves the model in comparison with the experimental data. The focus of this analysis is to improve the model at low temperatures based on the observations of how varying specimen properties affect the model.

4.1.2. Energy Balance Plastic Volume Approximations

A potential point of improvement previously identified was the basic formulation of the plastic zone energy dissipation term based on Irwin's plastic zone. To test the change from this plastic zone estimation on the EBSB, and therefore the deviation from the experimental dataset, this section aims to implement a variety of different plastic zones for implementation into the energy balance. The change in plastic volume per change in crack length is calculated in Equation 4.1 for the Von Mises plastic zone and in Equation 4.2 for the Dugdale plastic radius. Both of these are still used under the assumption of plane stress.

$$
\begin{aligned}
V_p &= \frac{1}{2}\int_0^{2\pi} r_p^2(\theta)d\theta \cdot T \\
\frac{dV_\mathrm{p}}{da} &= \frac{d}{da}\left[\frac{23\pi}{32}T\left(\frac{S_\mathrm{max}}{S_\mathsf{yield}}\right)^4 a^2 \sec^2\left(\frac{\pi a}{W}\right)\right] \\
\frac{dV_\mathrm{p}}{da} &= \frac{23\pi}{16}T\left(\frac{S_\mathrm{max}}{S_\mathsf{yield}}\right)^4 \sec^2\left(\frac{\pi a}{W}\right)\left[a + a^2\frac{\pi}{W}\tan\left(\frac{\pi a}{W}\right)\right]
\end{aligned}
\tag{4.1}
$$

$$
\left(\frac{dV_\mathrm{p}}{da}\right)_\mathrm{MISES} = \frac{23\pi}{32}\left(\frac{dV_\mathrm{p}}{da}\right)_\mathrm{IRWIN} \approx 2.258\left(\frac{dV_\mathrm{p}}{da}\right)_\mathrm{IRWIN}
$$

$$
\left(\frac{dV_\mathrm{p}}{da}\right)_\mathrm{DUGDALE} = \frac{\pi^5}{256}\left(\frac{dV_\mathrm{p}}{da}\right)_\mathrm{IRWIN} \approx 1.195\left(\frac{dV_\mathrm{p}}{da}\right)_\mathrm{IRWIN} \tag{4.2}
$$

With these formulations it is now possible to plug each of the plastic zones into the energy balance within the Matlab simulation of Kuijk [13]. The effect can be compared to experimental results to determine whether an increase in plastic volume will improve the alignment with fatigue results.

4.2. Specimen selection for physical testing

Specimen were selected for performing physical testing based on an analysis of requirements for testing the validity of the sliding-box analogy for an energy balance with an emphasis on low temperature effects.

The author stipulates that by varying temperature, grain direction, and base material, such as 2000 and 7000 series aluminum, it would be possible to determine the range of validity of the EBSB model with respect to variations in a material's physical properties. The focus will be on the change in stiffness, yield point, ductility, and strain hardening behavior as outlined in section 2.5. Additionally, as a part of the tests, the grain orientation will be taken into account with the quasi-static properties determined experimentally. They will be compared to the EBSB just like specimen aligned with the rolling direction. This material aspect is detailed further in subsection 4.2.2.

Determining a final material selection was done by taking into account the available raw plate material in stock at the laboratory as well as the requirements for varied yield points and ductile behavior. The first aspect in this consideration relates primarily to the thickness selection, since conclusions about how through-thickness effects have an effect on the EBSB model would be valuable to determine its range of validity. Very thin specimens were avoided for property comparison and for maintaining consistent specimen outer dimensions for use on the 100 kN MTS machines. For these fatigue machines, the load cell, hydraulic actuation speed, and controller are all optimized for stiffer specimens at high loads, which may become problematic if small or very thin specimens were to be tested.

In this study, 7075-T6 – a 7xxx series Al–Zn–Mg–Cu alloy [27]– was selected as the base material because its mechanical response is relatively close to elastic–perfectly plastic behavior. Furthermore, Kuijk [13] reported the largest discrepancy for this alloy, making it particularly interesting for a detailed comparison with the other materials considered in this work. From a practical standpoint, 7075-T6 was the most readily available in multiple plate thicknesses. Additionally, plate stock in 1 mm and 4 mm thicknesses enables an assessment of thickness effects. Plates with a thickness of approximately 6.4 mm are adopted as the primary comparison basis. At this thickness, linear elastic assumptions and a plane stress approximation should remain valid, while the associated load levels are sufficiently high to make efficient use of the available test machines and the climate chamber.

Alloy 6061-T6 – a 6xxx series alloy based on an Al–Mg–Si–Cu system – was included in the test matrix primarily due to its availability in plates of about 6.5 mm thickness, providing an additional material with comparable geometry for direct comparison at the reference thickness. 6061-T6 is additionally also cheaper, excellent for welding, and commonly used for pressure vessels which may be relevant to hydrogen tank designs. Finally, a 2024-T3 aluminum – a 2xxx series Al–Cu–Mg alloy – was selected as a representative third alloy, allowing the behavior of a more conventional Al–Cu system to be contrasted with that of 7075-T6 and 6061-T6 under the same testing conditions [27].

In addition to the regular alloys noted thus far, one more measure was taken to investigate a material with large amounts of strain hardening. Based on the over-aging methods proposed by Tzamtzis and Kermanidis [28] to improve the fatigue characteristics of 2024 aluminum, one additional material was added to the selection henceforth described as 2024-A300. This is the same base specimen as made from 2024-T3 but was over-aged for 15 hours in a curing oven at 300°C. A stress-strain curve for this material as it was proposed by Tzamtzis and Kermanidis [28] is found in Figure 4.2 and it is noted that the improved damage tolerance is associated with higher crack closure levels compared to the regular 2024-T3 alloy.

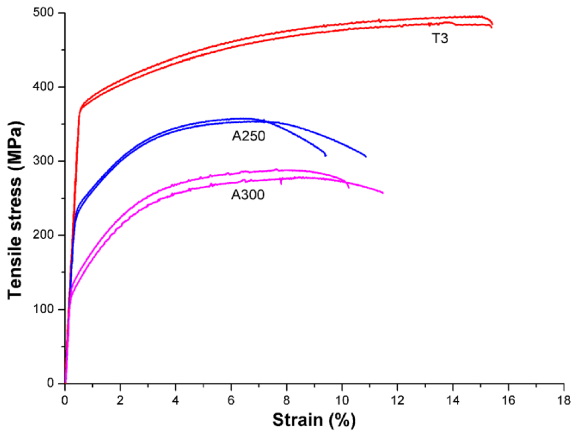

Figure 4.2: Over-aging effects on the stress-strain curve for aluminum 2024, A250 was over-aged at $250°$C and A300 at $300°$C - each for 15 hours. Taken from [28].

These material selections and ASTM standards led to the creation of two engineering drawings defining the exact fatigue and tensile specimen geometries, these can be found in Appendix A. Additionally, for both tensile quasi-static testing and fatigue testing specimen matrices are defined in Table 4.1 and Table 4.2.

Table 4.1: Quasi-static tensile specimen geometry and test temperatures matrix

#	Material	Thickness [mm]	Cross-sectional Area [mm^2]	Temperature [$\pm$3 K]
1	7075-T6	1.00	12.5	293
2	7075-T6	1.00	12.5	293
3	7075-T6	1.00	12.5	293
1	7075-T6	4.00	50	293
2	7075-T6	4.00	50	293
3	7075-T6	4.00	50	293
1	7075-T6	6.43	80.375	293
2	7075-T6	6.43	80.375	293
3	7075-T6	6.43	80.375	293
1	7075-T6	6.43	80.375	243
2	7075-T6	6.43	80.375	243
3	7075-T6	6.43	80.375	243
1	6061-T6	6.50	81.25	293
2	6061-T6	6.49	81.125	293
3	6061-T6	6.49	81.125	293
1	2024-T3	6.36	79.5	293
2	2024-T3	6.36	79.5	293
3	2024-T3	6.36	79.625	293
1	2024-T3-TL	6.36	79.5	293
2	2024-T3-TL	6.36	79.5	293
3	2024-T3-TL	6.36	79.5	293
1	2024-A300-TL	6.36	79.5	293
2	2024-A300-TL	6.36	79.5	293
3	2024-A300-TL	6.36	79.5	293

Table 4.2: Fatigue test matrix with material, thickness, stress ratio, loading, and temperature variables.

Variable	Material	T [mm]	R [-]	Temp. [± 3 K]	Load [kN]	Max. Stress [MPa]
Thickness	7075T6	1.00	0.1	293	4.5	45.00
	7075T6	4.00	0.1	293	16.5	41.25
	7075T6	6.43	0.1	293	26.0	40.44
Material	6061T6	6.50	0.1	293	26.3	40.46
	2024T3	6.50	0.1	293	38.0	59.75
	2024A300	6.36	0.1	293	52.0	81.76
Stress Ratio	7075T6	6.43	0.5	293	38.0	59.10
	6061T6	6.50	0.5	293	50.0	76.92
	2024T3	6.36	0.5	293	52.0	81.76
Temperature	7075T6	6.43	0.1	243	42.0	75.08

4.2.1. Specimen Thickness and Surface Roughness

Thickness effects as described by Suh et al. [29] may have a relevance to the properties of a specimen's material. The authors investigated the effect of surface roughness as well as thickness on the tensile properties of an aluminum dogbone. Equation 4.3 shows the grain size d to find the parameter ψ which is the relative grain size to specimen thickness. This relation can then be expanded to include the effect of the volume fraction of metallic grains with a free surface, α, in Equation 4.4 when including the specimen width W as well.

$$\psi = \frac{T}{d} \tag{4.3}$$

$$\alpha = 1 - \frac{(W - 2d)(T - 2d)}{WT} \tag{4.4}$$

In order to account for these effects in the physics-based approach it is necessary to test each fatigue specimen thickness in a quasi-static test as well. This will ensure that the effects described above are captured by the measured properties and show their effects on any fatigue simulations. Furthermore, it would be possible to show to what extent the thickness effects do exist and to observe the effect on fatigue properties.

Additionally, surface roughness is also a critical aspect in the function for metallic grains with free surfaces and rougher. When α decreases, the effect of the surface on the material's mechanical properties is enhanced [29]. For fatigue, increasing surface roughness facilitates crack nucleation but also has an effect on the crack propagation. More and greater imperfections on the plate surface may help the crack propagate or create deflections of the crack front. Surface treatments that work harden the surface on the other hand have an improving effect on fatigue properties [8]. For this reason, this parameter was kept the same across all tested specimen, the rolled plate faces were kept as-is. Conventional machining was limited to the outer contours of the specimen, and the pre-crack in fatigue specimen is created by the wire electric-discharge-machining (EDM) to avoid work hardening the crack initiation point.

4.2.2. Raw Plate Material Grain Direction

In general, the assumption is made that since aluminum is mainly an isotropic material, one can assume its material properties do not vary with any directional dependency. This assumption is likely true in the comparison with more severely directional materials such as fiber reinforced plastics. But when a rolled plate of raw aluminum stock is observed up close a rolling direction can be observed visually on the material's surface. Nečemer et al. [30] found that in a rolled aluminum 5083 plate the microstructure was similar in the rolling and transverse directions. The larger precipitates however were observed to elongate more in the rolling direction. Subsequent tensile and fatigue tests showed that there is a discernible difference in strength and fatigue life for specimen cut in rolling or transverse directions.

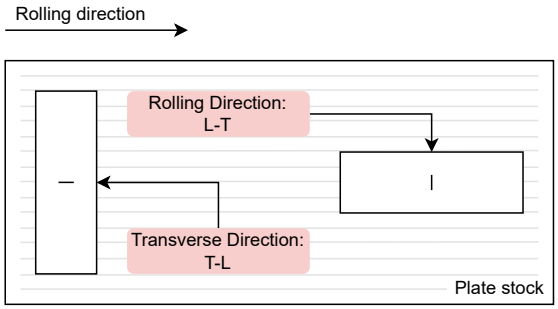

Figure 4.3: Specimen direction notation definition. Specimen that were cut in to align their major axis with the transverse material direction are notated with ”T-L”.

In order to evaluate the ability of the EBSB modeling approach to capture the material properties accurately based on the material properties determined with quasi-static tests, the 2024T3 and 202A300 alloy specimen were cut in transverse direction instead, indicated with T-L as in Figure 4.3, for all tests. This feature will be notated as in Table 4.2 with the T-L label in the material description.

4.3. Physical Testing Methodology

Physical testing will encompass two test setups. The first is a quasi-static test setup used with a dogbone specimen. The second setup will be the fatigue setup with a center cracked plate.

The quasi-static loading test will be used to gather material data on the quasi-static properties of the materials that will be tested. Table 4.3 shows all measured or recorded quantitative and qualitative variables. In order to ensure that the test conditions are as they will be in the fatigue tests, the temperature and the thickness of the quasi static specimens were matched to each fatigue specimen. This means that the two setups are dependent on each other for specimen and environmental consideration. For both, digital image correlation (DIC) was employed to use ”virtual extensometers”, image based strain gauges, and map the deformation field - particularly relevant to the fatigue tests.

Table 4.3: An overview of the measured and recorded variables in each of the quasi-static and fatigue tests.

Test Type	Outputs
Quasi-static Test	Average engineering stress-strain curve Ultimate tensile strength Yield strength Young’s modulus 10 stress/Strain pairs beyond the yield strain Displacement/strain field
Fatigue Test	Crack length versus cycles data Loading data Virtual extensometer data Displacement and equivalent strain field

4.3.1. Quasi-static Testing Method

In order to extract meaningful data from the fatigue tests that will be touched upon later on, the exact physical properties of the tested material plates is necessary. This will allow the EBSB (Sliding box with energy balance) Model to use the real material properties for accurate validation in comparison to the fatigue tests. The methodology for the quasi-static tests is described below with the aim of determining Young’s modulus, yield strength, and sampling yielded stress strain points.

To begin with the specimen geometry and measurement process must be defined. To get robust specimen that will function as intended with a low risk of non-representative behavior, the choice was made to go with ASTM E8M (Metric) guidelines for their design [31]. The relevant variations in thickness need to be accounted for, and to achieve the highest level of similarity to the plates used in the fatigue experiments, the same plate stock should be used in both tests. This necessitates the use of flat dog-bone specimen according to the standard.

Based on the constraints of the Delft Aerospace Structures and Materials Laboratory (DASML) the use of test machines is limited to Zwick branded quasi static testing machines.

The testing methodology for tensile testing of the specimen outlined in the quasi static test matrix in Table 4.1 was based on ASTM E8M guidelines. The testing was conducted primarily at room temperature ($23 \pm 3°$C) using a Zwick universal testing machine, with additional low-temperature testing for 7075-T6. Test specimens were prepared from sheet materials according to the test matrix below. Cutting was done with an aluminum saw from larger plate stock and with a guillotine cutter for plates less than 4 mm thick. A total of three specimens was tested for each material-thickness-temperature combination.

Prior to testing, specimens were machined to ASTM E8M specifications for sheet-type specimens, ensuring they were free from defects that could influence results. Each specimen was measured (thickness, width, gauge length) and labeled. A speckle pattern was applied to the gauge section using matte black spray paint to facilitate DIC measurements, see section 4.4 for the process. The speckles were of medium size to allow easy correlation between images even on the small gauge section with good accuracy but without specific displacement field resolution requirements.

Testing began with mounting the specimen in the Zwick machine, ensuring proper alignment. For the $-40°$C tests, a temperature chamber was installed around the specimen and grips on the 250kN MTS machine instead, with temperature monitoring to ensure stabilization before testing began. The DIC system was positioned to capture the entire gauge length with appropriate lighting conditions, with special consideration for viewing through the temperature chamber window for the low-temperature tests. See the setup images from room temperature and low temperature testing in Figure 4.4, while the schematic climate chamber testing setup is shown schematically in Figure F.1, as it was essentially the same as the low temperature fatigue setup.

For each test a pre-load of approximately 10N was applied to eliminate slack, followed by zeroing the extension. The tests were started at a displacement controlled rate of 0.01 mm/s during the elastic region, transitioned to 0.03-0.05 mm/s after yielding, and continued until complete specimen fracture. Data acquisition occurred at a frequency of 10 Hz, capturing the load, test time, total travel, and DIC images throughout the test. The fractured specimens were photographed and all data were compiled with proper specimen identification, and average values were calculated for each property across the sets of three trials.

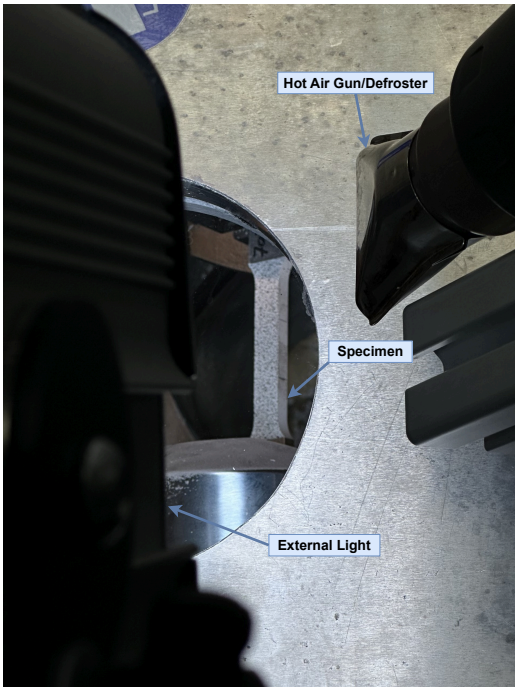

(a) Closeup of the specimen in the climate chamber at -30C

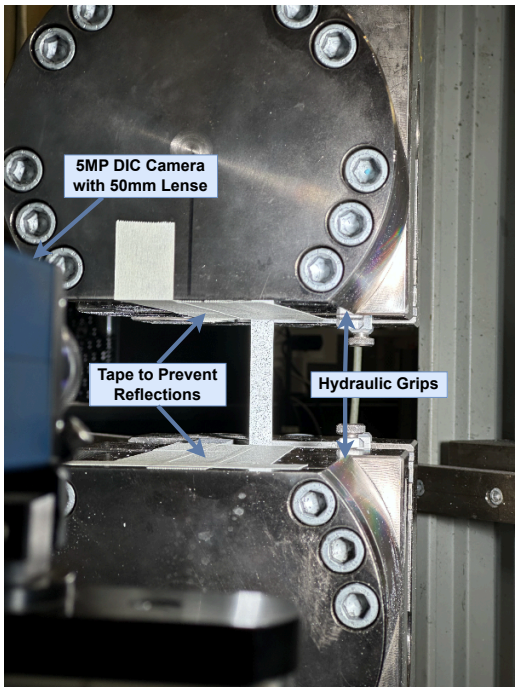

(b) Closeup of the specimen clamped in the testing machine and fully illuminated

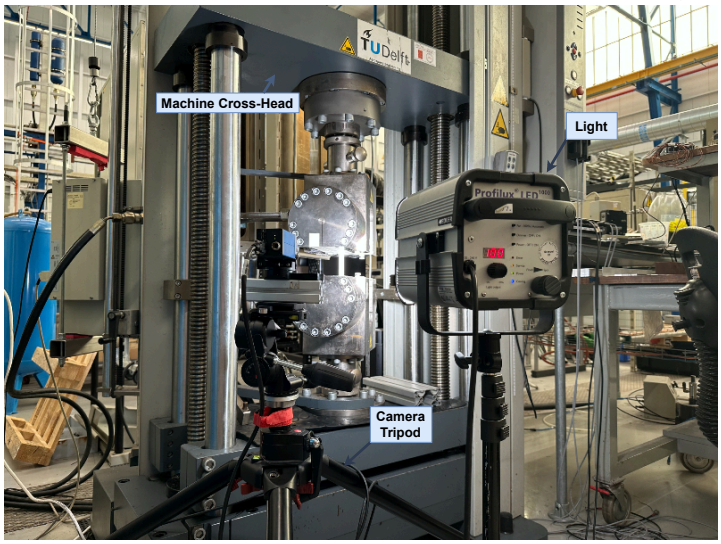

(c) Testing setup on the Zwick tensile testing machine to evaluate the quasi-static mechanical material properties.

Figure 4.4: Images of the quasi-static tensile testing setup on the Zwick machine and MTS machine for the low temperature trials.

4.3.2. Fatigue Testing Method

The testing methodology for fatigue damage growth testing of the aluminum alloys shown in Table 4.2 is based on ASTM E647-24 standard using Middle(cracked)-Tension M(T) specimens [32]. This choice was made to eliminate some variability in loading and testing. Using the middle tension specimen removes loading asymmetries that may be present in a comparable edge cracked specimen, this isolates the loading of the crack plane in the pure normal direction, also known as mode I. Using the M(T) specimen with a bolted steel clamp plate that is attached to the fatigue machine with a pin joint will then further isolate the loading conditions, being only able to transfer tension loads.

The majority of testing will be conducted at room temperature ($21 \pm 3°$C) using the 100kN and 250kN MTS fatigue testing machines. Test specimen will be prepared according to the engineering drawing in Figure A.2. Cutting will be done with an aluminum saw from thicker plate stock and with a guillotine cutter for plates 1 mm thick. The center crack is pre-drilled to 4 mm and then pre-cracked by 6.5 mm per side by wire-EDM. Only 1 specimen will be tested for each material-thickness combination.

Each specimen will be measured (thickness, width, initial crack length) and labeled with a unique identifier. A speckle pattern will be applied to the specimen surface using matte black and white spray paint to facilitate DIC measurements; this process is, again, outlined in section 4.4. The fully prepared specimen and camera setup is shown in Figure 4.6a, while the entire process of setting up a fatigue test run is shown schematically in Figure 4.5, including the necessary zeroing and reference image recording. Using Paris constants determined by Quan [16] for 7075-T6 and 2024-T3, as well as Tzamtzis and Kermanidis [28] for 2024-A300, and Ribeiro et al. [33] for 6061-T6, the maximum stress in the nominal section for each trial was determined with the goal of reaching $150,000$ to $200,000$ cycles for all trials.

The backside of each fatigue specimen is covered with a 50 mm wide white contrast strip centered on the crack. Figure 4.6b shows this strip quite clearly. It's made of only one to two coats of Rust-oleum 2700 RAL-9010 with the purpose of creating a very clean and white surface for high contrast images of the crack front. In addition to the two painted sides, each gets a 5 MP camera and a bright studio light for consistent exposure even when the lighting conditions in the lab were to change.

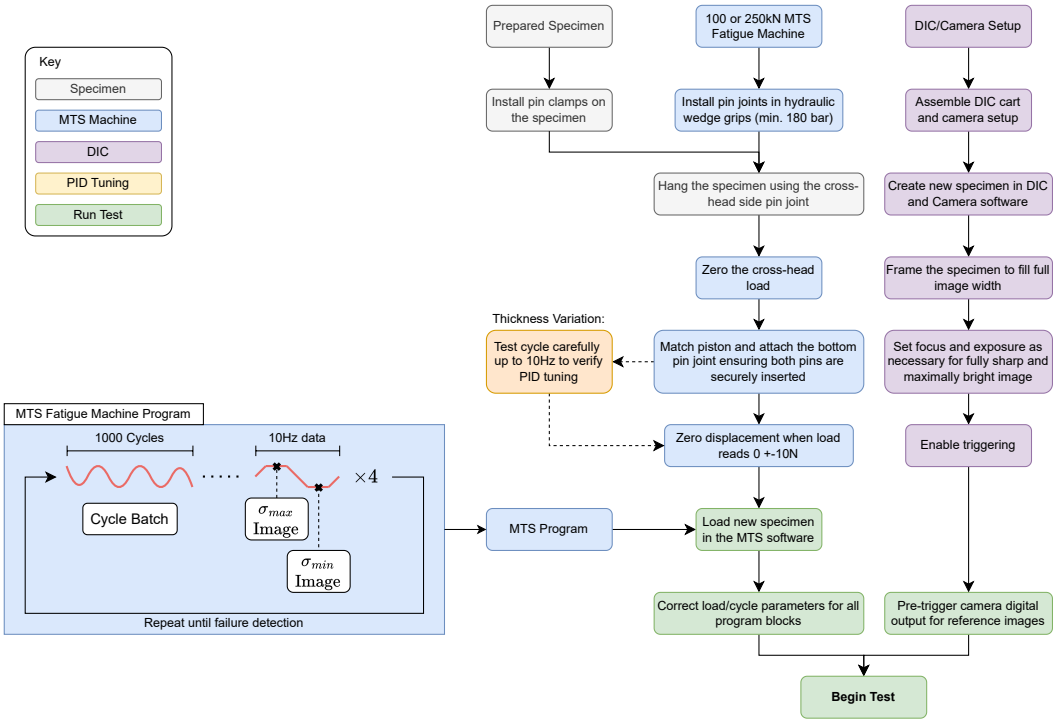

Figure 4.5: Workflow of setting up the start of a fatigue test with pre-prepared specimen

The DIC system will be positioned to capture the crack growth region with appropriate lighting conditions. DIC measurements will be taken every 1000 cycles during the majority of the test. As the crack approaches critical length (determined by preliminary analysis), the DIC measurement frequency may be increased to every 500 cycles to better capture increasingly rapid propagation phase.

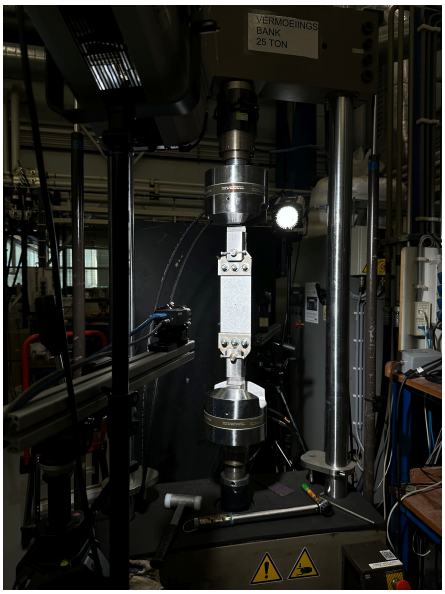

(a) Front side of the specimen displaying the speckle pattern for DIC.

(b) Rear side of the specimen, displaying the 50 mm white strip for high contrast crack images.

Figure 4.6: Fatigue testing setup at room temperature on the 250 kN MTS machine. Clearly visible are the bolted clamps which transfer loads to a tension isolating pin connection.

Post-test analysis will involve processing the DIC data to determine strain and displacement fields. Additionally, crack images will be processed to determine crack length versus cycles, calculating crack growth rate da/dN versus stress intensity factor range K_{eff} as outlined in subsection 4.5.4. The fractured specimens will be photographed and fracture surfaces examined to verify crack growth mechanisms. All data will be compiled with proper specimen identification, the appendix will include notes on specific observations per experimental trial. The processed data will be formatted for input into Matlab for EBSB comparisons.

4.3.3. Low Temperature Fatigue Testing

The general fatigue testing methodology has been outlined now. But in addition to the general methodology, the low temperature testing setup requires additional explanation. Figure 4.7 Displays the experimental setup for low temperature testing. The goal of this methodology is to achieve the lowest achievable temperature on the 250kN MTS machine which fits a climate chamber large enough for the fatigue specimen using the CTS climate control system.

The experimental setup could fit inside the climate chamber, but to preserve the pin-jointed boundary conditions and minimize the thermal mass within the chamber, the clamps were extended using double pin-joint connections. This configuration also helped to ensure that the specimen was subjected to purely uniaxial tension. Temperature control was achieved using a reference thermocouple, which was relocated from the internal CTS chamber to the fatigue chamber. To verify that the specimen reached a uniform and stable temperature, an additional thermocouple was attached to the backside of the specimen directly above the center crack. The specimen temperature was monitored and maintained within a range of ± 3K. With insulation applied around the double pin-joint connections, the minimum attainable temperature in the chamber was $-30°$C, as shown in Figure 4.7b.

During trial runs, fogging of the viewing window due to temperature and humidity differences proved problematic. This was mitigated by using a heat gun at its lowest temperature setting, directed at the viewing window to provide a defogging effect. Another issue encountered was friction in the pin joints, which could cause thermal runaway inside the chamber and raise the temperature to above $-10°$C. This was resolved by thoroughly cleaning and lubricating the joints, which maintained stable operation for approximately 6 hours, corresponding to a maximum of 140,000 load cycles. For test recreation, the test setup is shown schematically in Figure F.1.

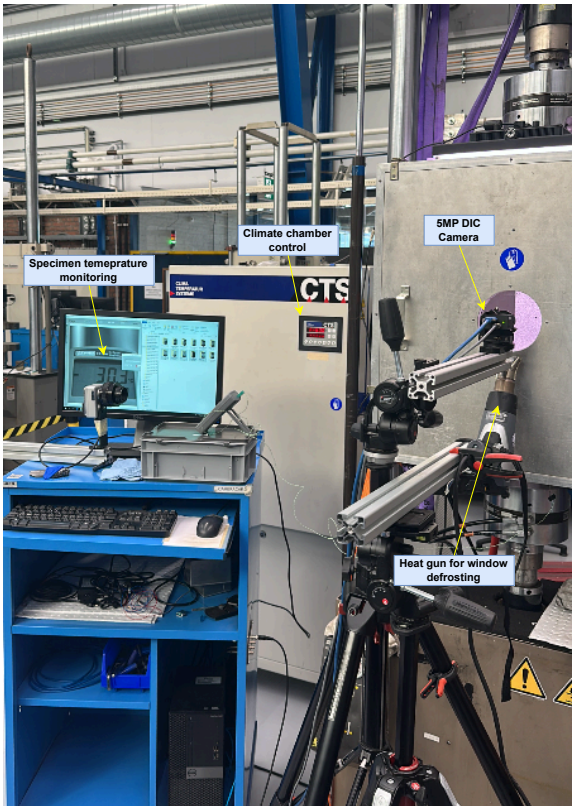

(a) Low temperature climate chamber test setup. Note the use of a heat gun at minimum temperature to defroster the viewing window.

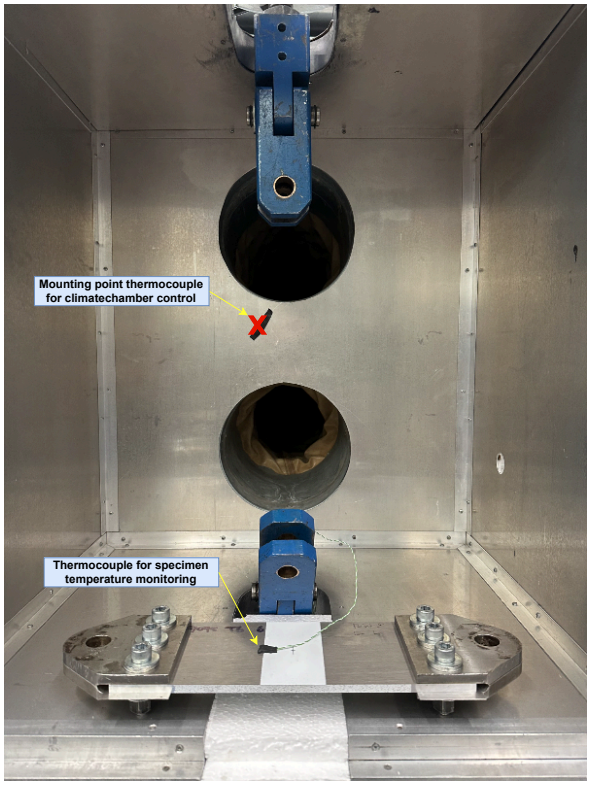

(b) Inside the climate chamber. Visible are the double pin joint extensions to work within the climate chamber as well as climate chamber and specimen thermocouple locations.

Figure 4.7: Fatigue testing setup at $-30°$C or 243K

4.4. Speckle Pattern Application

The first step in preparing for image correlation data processing later on is to cover the specimen in a speckle pattern. A speckle pattern in the context of this methodology refers to a fine, random, black and white pattern that is applied to the face of a specimen for image correlation. The standard manner to do so in the DASML laboratory is by spray painting the specimen in a paint booth. The steps for this process are rather straight forward and the same for both the quasi-static dog-bone specimen as well as the center cracked fatigue specimen. In general, this process was completed up to 48 hours prior to testing such that the paint was sufficiently dry but not negatively impacted by any storage conditions yet.

1. Enable all air extraction and lighting features of the paint booth
2. Clean the surface of the specimen from any debris or residue. This is done with acetone and paper wipes unless there is some persistent residue. In that case 3M Scotch-Brite pads are used to carefully abrasively remove local residue.
3. Use masking tape to completely cover the clamping areas as well as any area that isn't within the gauge section. Ensure that the tape is clean at the exact intersection between mask and paint area.
4. Clean the surface with acetone again.
5. Apply 3 coats of white spray paint, Rust-oleum 2700 RAL-9010 , ensuring that the specimen is coated with the paint evenly and that the entire area is saturated evenly.
6. Clean the nozzle of a black spray paint can, Rust-oleum 2700 RAL-9005, and clear the nozzle with a test spray.

7. Hold the spray can slightly tilted back, $30cm$ away from the specimen and off to one side for a test spray, slowly pressing the nozzle until only a mist comes out. Find the pressure point and exact distance from the specimen at which the mist creates a sufficiently fine speckle. Roughly Diameter $= 0.2mm$ order of magnitude.
8. Clean the nozzle and repeat the previous step. This time when the speckle is correct, begin to move the can to cover the specimen in speckle. evenly distribute the paint speckle until the ratio of speckle dots to white background approaches between 40:60 and 50:50. Multiple passes and repeats area allowed until this is achieved.
9. Lay the painted specimen to the side for drying, taking care not to touch any painted surface. Let dry for at least 2h, max 48h,
10. Once dried remove the masking tape carefully to avoid ripping any paint flakes off.
11. Correct mistakes and irregularities in the speckle pattern by breaking up over-sized black speckle with dabs of white spray paint from point 5. Adding new speckles to fill empty areas may be done with a matte permanent fine-liner pen such as Edding 1800 0.3.

4.4.1. Camera Setup for Digital Image Correlation

For DIC, it is evident that maintaining consistent lighting and maximizing the resolution of the speckle pattern is vital to get the best results on later image correlation. In order to achieve this with an experimental setup a process was developed to maximize the camera setup potential. Firstly, the camera setup was limited to a 5 MP camera with a square field of view (FOV) and a 50 mm lens was chosen to reduce distortion. To maximize the resolution of the specimen, it was framed to fill 90% of the width of FOV - ensuring the border is visible throughout the full cycle range. Secondly, the exposure was maximized while minimizing the aperture. This has the effect that the depth of field remains large and all of the speckle pattern is within focus even when out of plane movement occurs due to any clamping or loading related issues. The exposure is then set to avoid large over-exposed regions but retaining a uniformly distributed lighting setup based on the exposure finder in the Vic-2D recording software. Lights were positioned above the camera with an angle to avoid reflection and glare while staying in line with the specimen for an equal distribution. This strategy also avoids blinding the camera on the backside of the crack which captures the crack growth. Lastly, the focus is set based on the noise finder in the Vic-2D recording software. When the average noise and noise distribution is uniform and low, below 0.01μ across the speckle area, the setup is concluded. The image recording software was then armed to receive trigger signals.

4.5. Data Processing

In this section the processes for extracting final data from the various quasi-static and fatigue experiments is presented. The first step is to give an overview of the vision based analysis that was employed in both test types, namely two dimensional digital image correlation. Then the machine sensor data processing and results processing is covered.

4.5.1. Digital Image Correlation

The analysis of imaging data that was done for this step was completed with Correlated Solutions' Vic-2D 6 software. For quasi-static experiments the required output is only virtual extensometer data, providing what is essentially a very adaptable engineering strain processing method. Fatigue experiments used a combination of displacement and strain field outputs as well as virtual extensometer that are later used for interpolating missing crack length data when necessary. First off the basic aspects of DIC will be presented and then the exact application will be outlined. To establish a basic understanding of the image matching process mathematically the basics will be described first.

DIC determines surface displacements by tracking the displacement of small image regions, or subsets, between a reference image and a deformed image. Because a single pixel does not contain sufficient unique information to identify in a see of similar pixels, DIC relies on a textured, non-periodic speckle pattern to ensure that each subset contains enough gray-value variation for stable matching. The image-matching process is founded on the principle of intensity conservation, which assumes that for a material point originally located at pixel coordinate $\mathbf{x}$, the gray value is preserved under deformation,

$$G(\mathbf{x}+\mathbf{d}) \approx F(\mathbf{x}) \tag{4.5}$$

where F and G are the reference and deformed intensity distributions on an object and $\mathbf{d}$ is the displacement vector to be determined. The displacement is obtained by minimizing a similarity metric such as the sum of squared differences,

$$\overline{\mathbf{d}}_{\text{opt}} = \operatorname{argmin} \sum |G(\mathbf{x}+\overline{\mathbf{d}}) - F(\mathbf{x})|^2 \tag{4.6}$$

where $\overline{\mathbf{d}}_{\text{opt}}$ is then the optimal displacement vector. Alternative normalized correlation measures may become necessary when illumination variations must be accounted for. Minimization is carried out iteratively by linearizing the deformed image through a first-order Taylor expansion, resulting in a Newton–Raphson update of the Lucas–Kanade form,

$$\Delta\overline{\mathbf{x}} = -\left(\mathbf{G}^T\mathbf{G}\right)^{-1}\mathbf{G}^T\mathbf{g} \tag{4.7}$$

where G contains spatial intensity gradients within the subset and $\mathbf{g}$ is the gray-value residual vector.

Subsets are essential because they localize the correlation process and permit estimation of spatially varying deformation fields. When deformation cannot be represented solely as rigid translation, the mapping between reference and deformed coordinates is expanded using a subset shape function,

$$\boldsymbol{\xi}(\mathbf{x},\mathbf{p}) = \mathbf{p}_0 + \mathbf{A}\,\mathbf{x} \tag{4.8}$$

in which the parameter vector $\mathbf{p}$ includes both displacement components and local deformation terms, and the matrix $\mathbf{A}$ captures normal strain, shear, and rotation components. Such shape functions allow subsets to stretch, rotate, or shear in a manner consistent with the underlying deformation. Increasing the number of parameters, however, enlarges the associated Hessian system and acts as a spatial low-pass filter, reducing measurement resolution if subset sizes become large. Overall, DIC image matching relies on intensity conservation, local subset-wise optimization, and deformation-compatible subset mapping, enabling accurate displacement field measurement when appropriate speckle quality and subset parameters are selected. [34]

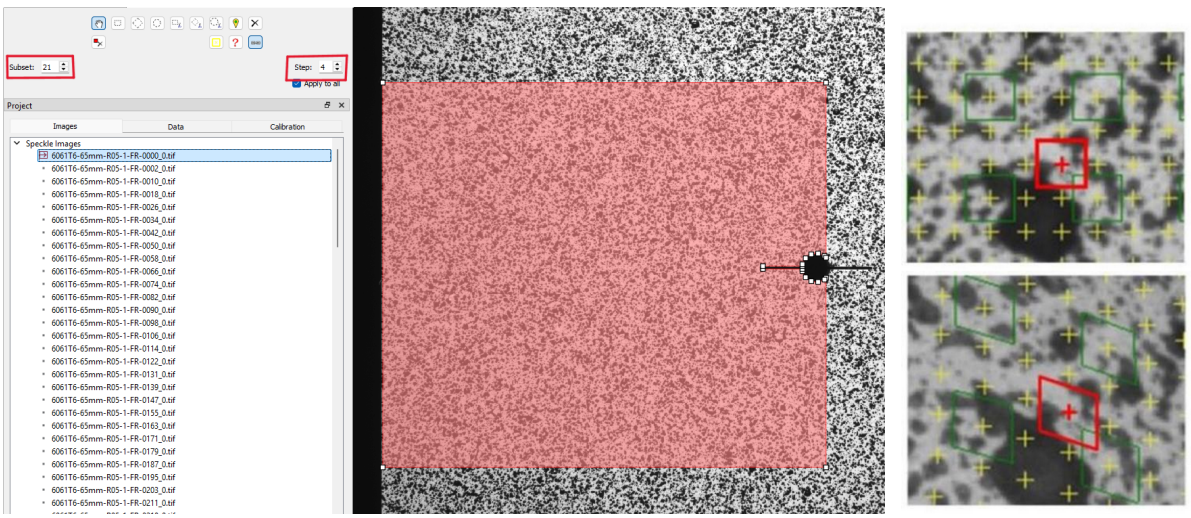

(a) (b)

Figure 4.8: Subfigure (a) shows the area of interest in red, subset of 21, and step size of 4 in Vic-2D 6. Subfigure (b) shows a visualization of step and subset sizes [35].

Overall based on the achievable speckle pattern with the available equipment, the subset size for fatigue specimen was best kept between 20 and 25 depending on Vic-2D's recommendation and the size of speckles in the area of interest. The step size for calculation within each subset was defined as ⅕ of the recommended subset size, which is a slightly finer mesh than the rule of thumb given by Lovaas [36], and was generally 4 or 5 pixels. The filtering window was kept to 15 steps which is the default setting and is center weighted.

4.5.2. Quasi-static Data Processing

This experimental run produced DIC imaging data as well as machine displacement and load readings at 10 hertz. Since the tensile testing machines do not have functional digital outputs, the syncing of the camera with the machine measurements was not possible. Instead measurements are started by simultaneous mouse clicks. Since in DIC the failure is clearly visible, the virtual extensometer data is aligned time-wise with the failure measurement of the machine. From this point given the known test length the shorter dataset determines the starting measurement moment. Overall, these steps yield raw stress-strain data to be used in subsequent steps.

For determining the stress strain plots, which will be used for all further quasi-static material property determination, engineering stress and strain were employed. This was done with intent as it matches the assumptions made for use with the EBSB approach. Since models including Irwin's plastic zone as well as generally linear elastic assumptions hold, this choice will be the best approach for further analysis.

An important aspect to determining valid quasi-static property data from each of the three trials for every martial and thickness combination is repeatability and consistency. The slope of the elastic portion of the stress-strain plot, to determine stiffness E, as well as the determination of the yield point σ_y, should be completed in the same manner for all data plots. The approach for this task is to determine the stress-strain curve for each test and then calculate an average curve. This average curve is used to determine the final mechanical properties as well 15 equally spaced stress-strain coordinate pairs extracted after the failure strain.

Since not all datasets are exactly aligned in order to determine an average curve between all data points as well as intersects, they are shifted to intersect at the origin and re-sampled to 10,000 points. The interpolated value at each sampling point is based on a shape-preserving piecewise cubic interpolation of the values at neighboring grid points, this way the maximum amount of information is conserved. Following this step the average curve can be plotted and based on curve intersects defined by the user the slope of the elastic portion is determined. A linear line through these intersects is plotted and then offset by 0.2% strain to determine the most common variety of the yield strength, $S_y = R_{p0.2}$. Figure 4.9 shows all these processing steps on an example average stress-strain curve.

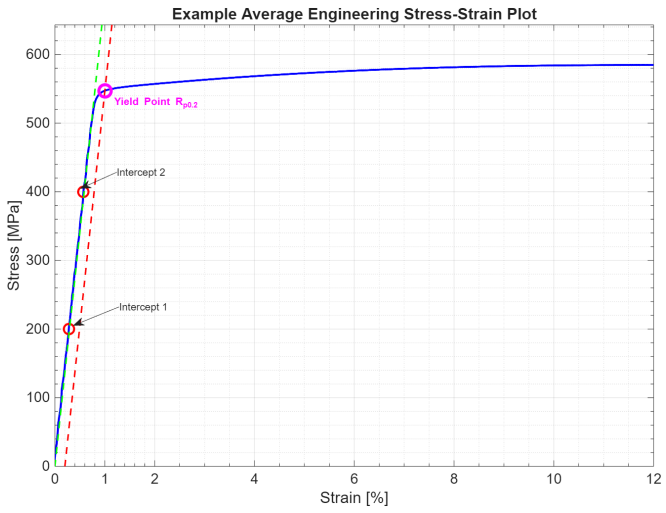

Figure 4.9: Example stress strain plot. The green dashed line is the elastic slope based on intercepts 1 and 2, while the red line is a 0.2% strain offset from the linear elastic portion of the stress-strain curve.

4.5.3. Fatigue Data Processing

Fatigue data processing begins with DIC to determine strain fields as well as virtual extensometers to aid in the interpolation of missing crack length data based on a strain measurement across the crack. This process starts with extracting every 8th maximum load image taken of the speckle pattern and running Vic-2D 6 on these images. Complications in this step arose when the 250kN MTS machine didn't reliably trigger the camera triggering digital output signal, so the majority of tests were sorted manually. In DIC, the analysis was done on the half crack on whichever side showed the least noise from the speckle pattern. Here the half crack analysis, as it is used in most fatigue models, is assumed valid due to the observed symmetric crack propagation. More detail on this choice is given in subsection 4.5.4. The area of interest (AoI) for this step is shown in an example in Figure 4.8a, note the pre-drilled hole and machined pre-crack being excluded from the AoI to improve convergence and avoid false measurements at the crack front due to noise. The height of the AoI is kept to approximately W/2 to ensure all of the crack tip plasticity is captured and visible within the AoI, even for large cracks. Lastly, after processing DIC data according to subsection 4.5.1, a strain computation to determine the equivalent Von Mises, as well as principle, strain values which are exported per pixel into a sheet. This data may be used later to re-create the strain fields of various sorts for plastic zone analysis.

The remaining fatigue data is processed as outlined in the process flow diagram Figure 4.10. The most important data comes from the crack growth measurements covered in subsection 4.5.4. The DIC analysis will be used to find missing low temperature crack data and for the analysis of crack tip plasticity which will be outlined later.

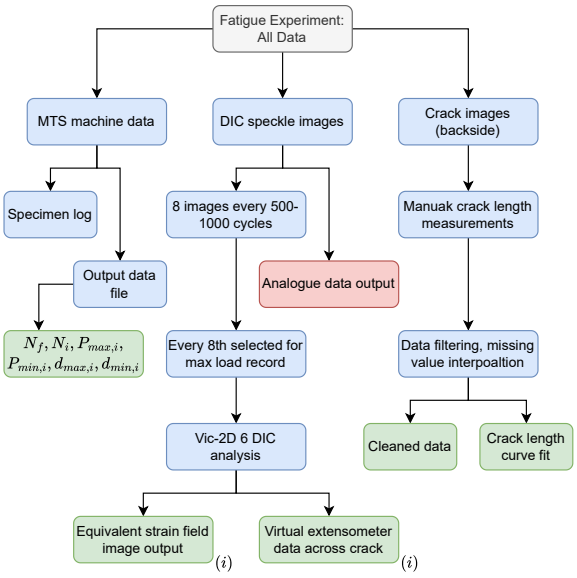

Figure 4.10: Breakdown of data produced by each fatigue experiment. Final outputs for results processing in green.

4.5.4. Crack Growth Rate Measurement

For the evaluation of crack growth, custom MATLAB code was developed to enable manual crack length detection from the recorded fatigue images. Only crack images acquired from the back side of the fatigue specimen were analyzed, starting from $0.5N_f$. Prior to measurement, all images were cropped such that only one half of the crack was visible. This approach follows the common fatigue analysis assumption in which only half of the crack is modeled or measured, with the crack front taken to be symmetric about the specimen centerline. Although this introduces an inherent loss of accuracy, visual observations during testing indicated that the crack propagated in a highly symmetric manner in the region of interest, which supports the validity of this simplification. The cropped region used for the measurements is shown in Figure [placeholder]. For each specimen, the crack initiation point was selected once, and for all subsequent images the manually selected crack front position was referenced back to this initial point to obtain crack length as a function of load cycles up to final failure. The resulting crack length versus cycle data were then smoothed using the MATLAB "rloess" filtering method.

In MATLAB, the “rloess” method implements robust local regression smoothing, where each smoothed value is obtained by fitting a low-order polynomial to data within a local span using distance-based regression weights, then iteratively down-weighting outliers via robust weights derived from the residuals [37]. With a window (span) of 10 points, the algorithm repeatedly fits a locally weighted regression over the 10 nearest neighbors of each sample and suppresses the influence of points whose residuals exceed several times the median absolute deviation, producing a smooth curve that follows the underlying trend while greatly reducing the impact of noise and isolated spikes [37].

For plotting da/dN versus ΔK_{eff} results the rate of change becomes important between each data point. This leads to very noisy and sporadic data points that are difficult to compare to those generated by the EBSB model. To combat this effect, the data points are fit to a second order exponential function least squares curve fit. The idea with the second order exponential is that it can somewhat capture the inflection point that would relate to the transition into the unstable final failure damage growth regime.

The value for ΔK_{eff} is determined with the following function:

$$\Delta K_{eff} = (S_{\max} - S_{\text{op}})\beta\sqrt{\pi a} \tag{4.9}$$

Using ΔK_{eff} is a valuable strategy because this effective stress intensity factor is meant to represent only the part of the loading cycle that actually opens and drives the crack. In many metals including aluminum, plasticity-induced closure, roughness, and oxide debris can keep the crack faces in contact for part of the cycle. If you plot da/dN vs. ΔK, two tests with different stress ratios (R), thickness related constraint, or surface condition may look artificially different because the amount of crack closure differs [8]. Using ΔK_{eff} removes the non-driving part below the opening level, so curves often collapse better across conditions. The opening stress used to define the magnitude of S_{op} is often defined by Schijve [20] [13] with the following relation:

$$\left.\frac{S_{op}}{S_{\max}}\right|_{\text{Schijve}} = 0.45 + 0.22R + 0.21R^2 + 0.12R^3 \tag{4.10}$$

4.5.5. Method for DIC Strain Field Analysis

An interesting approach has been made by Lemmen [38] who measured the plastic zone in a fatigue crack propagation experiment with DIC. Instead of plotting continuous interpolated strain fields for analysis though, Lemmen plotted iso-lines which were used for plotting the plastic zone contours.

The strain field output from 2D DIC analysis includes an equivalent Von Mises strain output, this value should be able to determine the in-plane strain magnitudes for comparison with the failure strain determined from quasi-static analysis. The Von Mises strain definition is given by Equation 4.11.

$$\varepsilon_v = \frac{2}{3}\sqrt{\varepsilon_1^2 - \varepsilon_1\varepsilon_2 + \varepsilon_2^2} \tag{4.11}$$

Earlier in the quasi-static mechanical material property definition, subsection 4.5.2, a variety of post-yield equidistant stress-strain data pairs were extracted between the yield point and ultimate stress. When using a number of these steps to define idealized strain magnitude iso-lines, it will be possible to extract the strain magnitude levels within the plastic zone from DIC strain field data. Next, the areas of various strain magnitudes, quantized to the determined plastic strain levels, can then be used to define the strain energy density when combined with the stress values. The strain energy density is then defined as in Equation 4.12, as proposed by Stephenson [22]. We recall from subsection 2.3.4:

$$W_o = \int_0^{\varepsilon} \sigma d\varepsilon \tag{4.12}$$

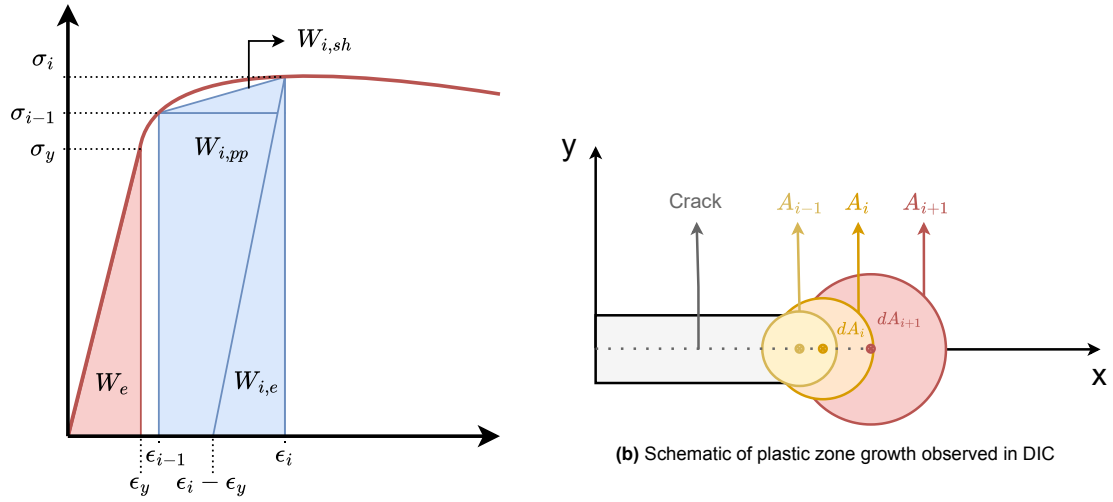

(a) Bi-linear cumulative approximation for strain energy density used for determining W_p

(b) Schematic of plastic zone growth observed in DIC

Figure 4.11: Plastic zone growth and plastic strain energy density schematics to illustrate the calculation of dU_p/da from DIC and how to replicate this calculation with analytical methods.

Using this relation in a discretized fashion on the stress-strain curve determined from quasi-static tensile testing, the plastic strain energy W_p can be determined. Figure 4.11a shows the process schematically. For every i^{th} pair of n total offset yield ($\sigma_{y,0.2}$ and $\epsilon_{y,0.2}$) and post yield stress (σ_i) and strain values (ϵ_i) the strain energy density (SED) is defined by the increment in stress level multiplied by the increment in strain. Then the elastic portion is subtracted again in an idealized fashion to attain the plastic portion only. Working with the polygons shown in the figure, the discretized plastic strain energy density can be defined. Here $W_{i,pp}$ is the perfectly plastic SED, $W_{i,sh}$ the strain hardening related SED, and $W_{i,e}$ or W_e the elastic portions of the SED. Let the 0.2% offset yield point be defined as $i = 1$.

$$W_{p,i} = \left(\frac{1}{2}\sigma_1 \cdot \epsilon_1 - W_e\right) + \sum_{i=2}^{n} (W_{i,pp} + W_{i,sh} - W_{i,e}) \tag{4.13}$$

The importance of using the 0.2% offset yield stress and strain becomes evident here. It allows measuring at least a small, non-zero, plastic strain energy density even for the iso-strain area between the yield iso-line and the first sampled stress-strain pair post-yield.

To find the total plastic energy, the energy density can be applied to a plastic volume increment. This can also be calculated in a discretized fashion for DIC applications. Figure 4.11 shows the growth of the plastic zone in an exaggerated schematic fashion. Again the i^{th} increment of the plastic zone is related to an increase in the incremental area growth term dA_i. In this application however each increment is defined by a batch of cycles, 1000 for example. The batch of cycles is related to a growth of the crack which results in an increment in the plastic zone. For an energy formulation with DIC derived iso-strain areas, the value of the plastic area $A_{p,i} = A_i$ may be determined for each strain magnitude by taking only the area between iso-lines in the DIC strain field into account. The plastic volume at each strain level ϵ_i is determined with the growth increment with respect to the previous DIC image as $dA_i = \Delta A_i$. This area increment can be related to the crack length increment to quantify $dV_{p,i}/da \approx \Delta A_i/\Delta a \cdot T$ as a locally linearized estimate.

5

Results

We recall from the previous chapter that the research objective is to expand and validate the physics-based sliding box analogy for modeling fatigue damage propagation at low temperatures by reviewing the energy balance and comparing the model to a range of varied experimental data. The path to this objective has been outlined, and a large range of comparable fatigue test results have been produced. With this collected data, the next step is to evaluate the energy balance with the sliding box analogy model as it is applied to the collected datasets.

The quasi-static material properties have been determined for the raw material and are used as inputs to the EBSB. With the aim to validate the sliding box analogy, all of the data is presented to investigate the error between the EBSB and testing data for material, stress ratio, and thickness variations. Next, the sliding box analogy is manipulated with the F_{stic} term to determine how sensitive the model is to this term.

In order to find a way to expand on the EBSB, a variation of plastic zones was undertaken. By changing plastic zones between Irwin's, Dugdale's, and Von Mises' criterion plastic areas, the effect of the plasticity assumptions is investigated. An additional approach is presented on how to implement a simplistic approach to accounting for work hardening in the plastic zone in an effort to improve on this energy term.

First, the results for the quasi-static testing are presented, followed by an analysis of the fatigue results. Secondly, the EBSB model is run for all tested property variations as well as with variations of the model itself. This includes reaching additional conclusions on the EBSB model with different plastic zone approximations. For this the root mean square error (RMSE) between experimental data and the model is compared across the specimen variations. The most important metric for determining the validity of the framework's application will be the comparison of slope, offset, and limit cases with the crack growth rate testing results.

Next, the temperature dependency and error are investigated more closely by comparing the room temperature fatigue test to the $-30°$C fatigue run. This is done by comparing 7075-T6 aluminum experimental data in each environment with the EBSB model. Lastly, to strengthen the analysis and verification of testing results, the recorded DIC displacement fields are processed. This allows analyzing the plastic zone volume and strain field around the crack tip.

5.1. Quasi-static Tensile Testing Results

This section presents the processed results of the quasi-static tensile tests. For each material and thickness and temperature a total of three trials were done, and the average of the three curves was calculated to determine the mechanical properties. Figure 5.1 shows the final failure surfaces for each experiment.

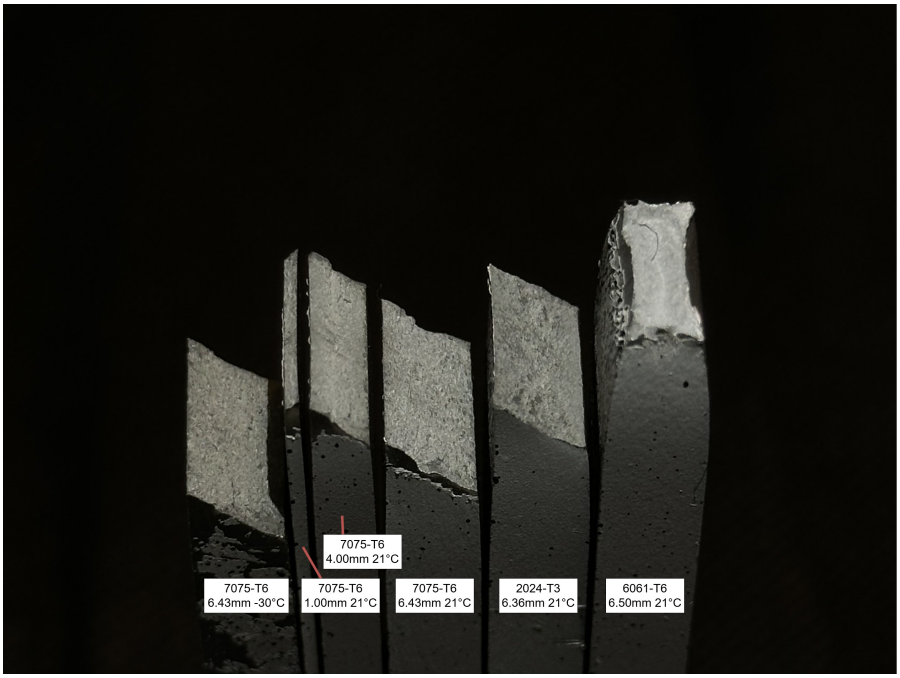

Figure 5.1: Fracture Surfaces of representative specimen for most materials, thicknesses, and the low temperature trials. 2024-T3 in T-L grain alignment.

The fracture surfaces in this tensile dog-bone set appear predominantly ductile with slant, shear-type rupture, which is a common macroscopic outcome for thin and intermediate-thickness ductile metals under tensile loading. Slant fracture is observed in thin sheet geometries and is associated with a plane-stress dominated state in strong materials with low ductility and potential mixed-mode contributions through the thickness [39]. In that context, the 7075-T6 1 mm specimen can be expected to show the strongest plane-stress character and also displays a pronounced slanted failure plane, while increasing thickness toward 4 mm and 6.43 mm typically increases constraint, a reduction in the dominance of the thin-sheet slant morphology is not observed. The 7075-T6 6.43 mm at 30°C likely retains the same overall ductile mode but with reduced macroscopic ductility relative to room temperature, consistent with the well-documented increase in strength of aluminum alloys at lower temperatures while maintaining ductile failure [25]. When comparing alloys at similar thickness near 6.4–6.5 mm, the macroscopic appearance is consistent with the expected property ranking in these tempers, where 7075-T6 is generally higher strength with lower elongation than 2024-T3, and 6061-T6 is lower strength with comparatively higher ductility. This higher ductility can be seen in the right most specimen which shows a bathtub shaped rupture that is typical to pure Mode I loading in weaker, ductile metals [39].

The results of quasi-static tests showed 6061-T6 to be the most ductile with the least amount of hardening in Figure 5.2. The fracture surface differs from the rest and this is likely due to the behavior toward final failure where at very constant stress there is a lot of deformation. In practice, the failure for this material also wasn't sudden and after releasing the hydraulic clamps it was necessary to pull the top and bottom half of the dog-bone apart from each other.

5.1.1. Average Quasi-Static Testing Results

Figure 5.2 shows the engineering stress–strain response for the four aluminum alloy variations (6061-T6, 2024-T3, 2024A300, and 7075-T6 tested at both $21°$C and $-30°$C), all with thicknesses of approximately 6.4-6.5 mm. All materials exhibit the usual initial linear elastic regime with similar stiffness, followed by yielding and subsequent work hardening up to a peak stress. The 7075-T6 curves clearly reach the highest yield and ultimate stresses, with the $-30°$C curve lying slightly above the room-temperature 7075-T6 curve, indicating an increase in strength and work-hardening capacity at lower temperatures. The 2024 alloys occupy an intermediate range in both yield strength and work hardening, while 6061-T6 shows the lowest yield strength and a more gradual hardening behavior. At larger strains, all curves display some softening in engineering stress, consistent with the onset of necking, highlighting the combined influence of alloy type and temperature on yield strength, work hardening, and overall ductility. The resulting quasi-static mechanical properties that can be extracted from this graph are shown in Table 5.1.

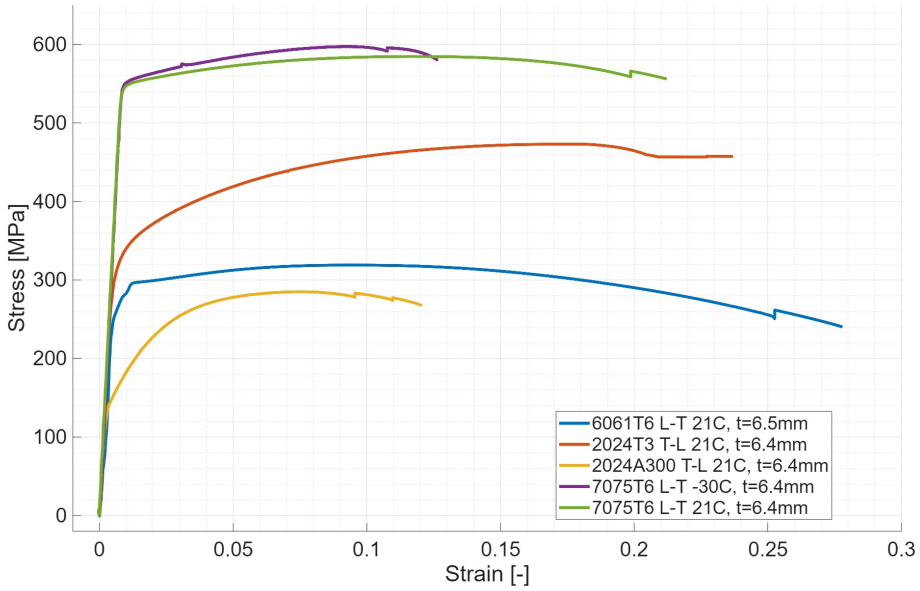

Figure 5.2: Quasi-static tensile test engineering stress-strain curves from the average of each set of trials for material and temperature variations. Steps towards the end due to different final failure strains between trials.

In the second graph, Figure 5.3, the engineering stress–strain curves are shown for the same alloy and orientation, 7075-T6 L–T at $21,°$C, while the specimen thickness is varied between $t = 1, 4$, and $6.4, \mathrm{mm}$. All three curves nearly coincide in the elastic region and through the onset of plasticity, indicating that the initial stiffness and yield strength are essentially independent of thickness in this range. The subsequent work-hardening behavior is also very similar, with all curves reaching comparable peak stresses of about 580 MPa and only minor differences in the shape of the curves at larger strains. Small deviations appear near the onset of necking, where the thicker specimen shows a slightly smoother softening response and marginally higher uniform elongation, but overall the results suggest that, for 7075-T6 under quasi-static loading, thickness has only a minor influence on yield strength and work-hardening characteristics.

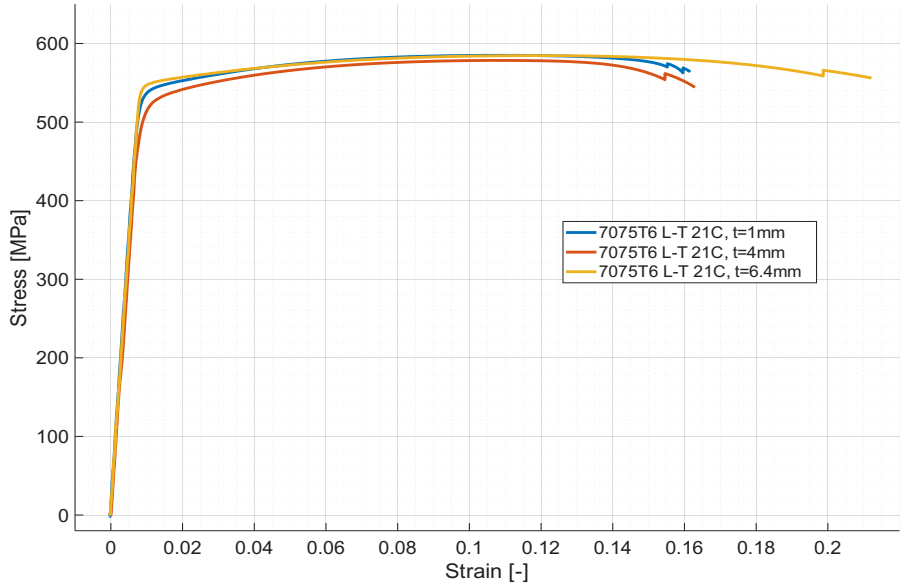

Figure 5.3: Further engineering stress-strain curves from the average of each set of trials for thickness variations of the base material 7075-T6. Steps towards the end due to different final failure strains between trials.

Table 5.1: Quasi-static tensile properties for different aluminum alloys, all tested at a temperature of $21°$C. All grain rolling directions are L-T unless otherwise specified.

Material	E [GPa]	$\sigma_{y0.2}$ [MPa]	$\epsilon_{y0.2}$ [%]	σ_{ult} [MPa]	ϵ_{ult} [%]	T [mm]	Temp. [°C]
6061-T6	57.21	263.13	0.6599	318.98	9.3482	6.50	21
2024-T3	66.92	315.59	0.6716	473.08	17.5533	6.36	21
2024-A300 (T-L)	57.48	148.83	0.4589	285.02	7.5448	6.36	21
7075-T6 (T-L)	68.28	547.21	1.0015	584.66	11.6425	6.43	21

Table 5.2: Quasi-static tensile average properties of 7075-T6 (L–T) for thickness and temperature variation.

T [mm]	E [GPa]	$\sigma_{y0.2}$ [MPa]	$\epsilon_{y0.2}$ [%]	σ_{ult} [MPa]	ϵ_{ult} [%]	Temp. [°C]
1.00	67.77	536.42	0.9916	585.04	11.1633	21
4.00	66.27	511.49	0.9719	578.47	10.7625	21
6.43	68.28	547.21	1.0015	584.66	11.6425	21
6.43	68.56	558.00	1.0070	597.40	9.3564	-30

5.1.2. Outliers and Corrections

The datasets from the 7075-T6 4 mm plate, 6.4 mm plate, and $-30°$C trials each had an issue in the 2nd or 3rd trial with the DIC pattern or some grip slippage. The consequence of this being that it caused erroneous stiffness and yield values. An example of the error that was encountered was a zero displacement stress likely caused by a bad reference DIC image. These trials were skipped as outliers and the average curve calculated from the two remaining trial runs instead. The test matrix Table B.1 in the appendix gives an overview of all trials and the removed outliers.

In addition to the outlier removal all tests were artificially zeroed. Since the DIC data is not synchronized to the start of the test, they were aligned using the failure moment instead. Both the load data and DIC images were recorded at a frequency of 10 Hz. This means that by finding the moment of failure, the start of the experiment can be determined in time by comparing the number of measurement points and then offsetting any displacement errors. Measurements with a synchronized mechanical extensometer would have been beneficial in this regard.

5.2. Fatigue Testing Results

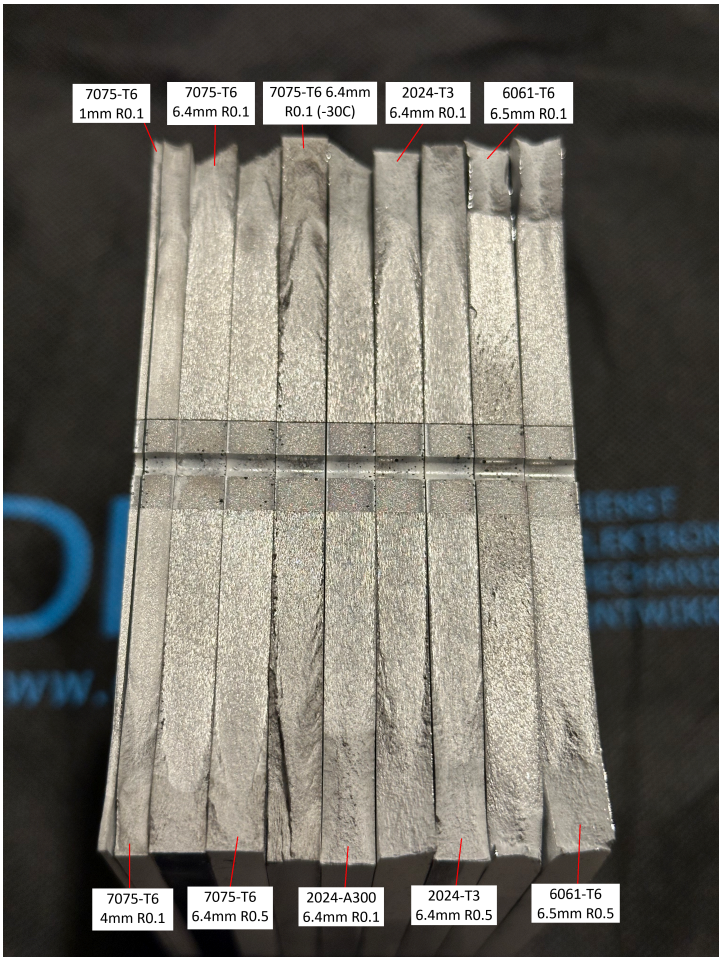

Figure 5.4: Fatigue crack surfaces of the top plates for each thickness, material, temperature, and R-ratio variation.

The crack plane surfaces shown in Figure 5.4 look broadly similar across the set. The surfaces are predominantly flat and planar through the initial crack-growth region with modest variations in roughness between alloys, thicknesses, and stress ratios. At the scale shown, one cannot see clear beach marks or distinct multi-site initiation features, so the failure mode looks like dominant single-crack growth to final failure at constant amplitude loading, matching the test conditions. Most specimens display pretty clear development of single or double shear lips in the last third, or less, of crack growth.

The room temperature 7075-T6 specimens appear to show the most uniformly planar and less topographically rough fracture appearance compared with the 2024 and 6061 specimen. In aluminum alloys this kind of smoother, more featureless macroscopic fatigue surface is often consistent with lower crack-tip plasticity and less tortuous crack paths. This behavior can be correlated with higher crack-growth efficiency once a crack is established [40]. This is due to the increase in created surface energy leading to an increase in energy required per unit of crack growth. Angling of the crack tip line through the thickness also reduces the effective driving force for crack growth since local stress intensity at the tip decreases [41]. This context helps explain the improved fatigue life of the 2024-T3 and low temperature 7075-T6 tests. They show some increased tortuosity indicating increased crack shielding and a higher energy dissipation per crack growth stemming from the $\frac{dU_a}{da}$ term in the energy balance.

Across the stress-ratio pairs, any visual differences are subtle in Figure 5.4, but the R = 0.5 specimens do look slightly more uniformly flat with a less pronounced transition to final failure. This would be consistent with the typical effect of a lower relative ΔK and potentially lower amounts of crack tip plasticity. Similarly, the thickness variations in 7075-T6, specifically the 4 mm specimen, shows small changes in

surface texture through the thickness that hint at shifting constraint, perhaps to plane strain conditions. In general though, at the tested thicknesses the macroscopic features are not starkly different indicating consistent load introduction and no major differences in the stress state in and out of plane.

At this point it may be interesting to note that the 6061-T6 at R=0.1 fatigue test ran over 900,000 cycles due to an erroneous loading calculation. The test was removed from the upcoming analysis due to this and sporadically missing crack tracking images. Nonetheless, the fracture surface shows some clear differences in the crack surface. In the crack initiation regime a darker color is visible due to increased surface roughness. This is likely due to the very slow initial crack growth rate promoting plasticity and allowing the crack front to propagate slowly rather than in larger increments typical of brittle materials.

The 2024-T3 and 2024-A300 specimens appear to present slightly more surface texture and irregularity than 7075-T6, while 6061-T6 looks and felt more ductile in the final fracture region which was also evident when dismounting the specimen from the fatigue machine. This impression helps support the finding that these materials presented increased ductility and therefore had improved crack shielding mechanisms that improved their fatigue damage tolerance. Appendix B presents the result matrices, including the fatigue lives that were determined from testing. Comparing the results matrix with the test matrix Table 4.2 shows the increase in maximum nominal stress (without crack geometry corrections) which resulted in the same cycle life that the 2024-T3 and 6061-T6 specimen displayed.

5.2.1. Shear Lip Development

Shear lips developed in single or double shear in essentially every fatigue test shown in Figure 5.4. The same was also observed in Figure 5.1 where all but 6061-T6 display a close to pure single shear plane. Zuidema et al. [42] explains the shear lip process as being dependent on the crack growth rate as well as the plane stress condition. Generally, they state that the related change in fracture mode for 7075 and 2024 alloys can begin in the range of 0.1 μmm/cycle and complete transition may occur at 1 μmm/cycle. Given that at higher K_{max} there is more plane stress [42] the results shown in subsection 5.2.2 as well as Figure 5.4 align, showing that after the 1 μmm/cycle of crack growth point, a thickness and stress state dependent plane stress condition is reached to allow formation of full shear lips.

The formation of shear lips will be ignored for the energy balance calculations in the coming sections as assumed in the methodology already. This is supported by about two thirds of the crack growth region not showing significant shear lips for most materials. This implementation has already been covered in subsection 4.1.1 and will be used in the coming sections covering the EBSB. In opposition to this choice, Kuijk [13] accounted for fully developed shear lips likely due testing plates with lower thickness at similar maximum stress conditions. This could have led to the shear lip formation conditions being reached at an earlier stage which was not observed in the fatigue tests presented in the results presented here.

5.2.2. Crack Growth Rate Results

This section will cover the experimental results of the crack growth measurements. Recalling from subsection 4.5.4 the crack length was determined from images taken of the rear side of the specimen accounting for half of the total crack starting at 6.5 mm for each fatigue test. For all tests except the one performed at low temperature, the crack is only tracked after half the cycles to failure ($0.5N_f$). At this stage the crack was clearly visible but still short, since the crack length of the low temperature fatigue test was interpolated from measurements and displacements it was calculated for the entire life.

The complete results with plots of filtered data, curve fit data, and EBSB can be found in section D.1 for all of the tests with $a - N$ curves as well as da/dN versus ΔK plots. First the filtered raw crack length per cycle data, determined according to subsection 4.5.4, is shown in plots such as Figure 5.5a where the second order exponential curve fit is applied. Then the crack growth rates are determined with experimental data this can be done by taking the derivative, with respect to cycles, of the curve fit function or by dividing each successive crack length increment by its cycle increment. An example of this data is shown in Figure 5.5b. All comparisons and plots in the upcoming results are analyzed on linear axes in contrast to the popular Paris curve to avoid collapsing details onto a log-log scaled plot as outlined by Alderliesten [43].

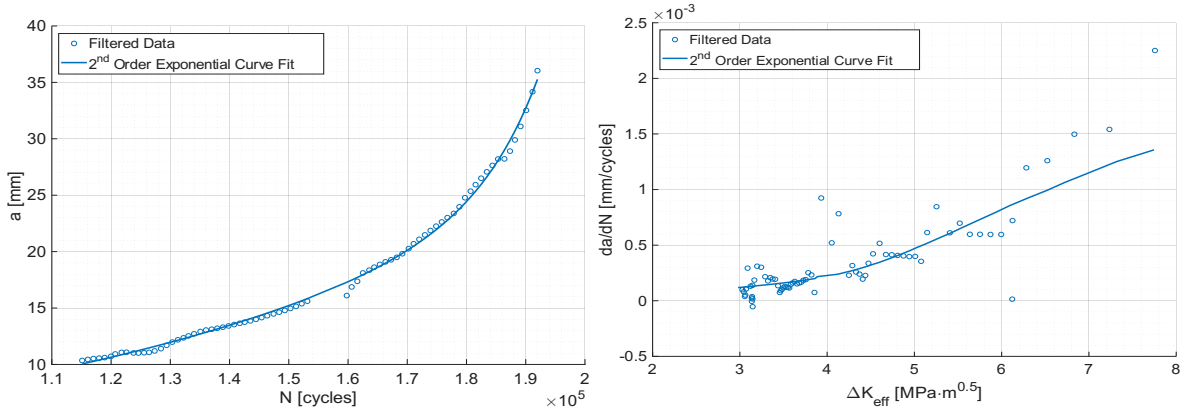

(a) Crack length versus cycles plot for 2024-T3 fatigue tested at $R = 0.5$

(b) Crack growth rate versus the effective stress intensity factor curves from data and EBSB model for 2024-T3 at $R = 0.5$

Figure 5.5: Example figures showing the exponential curve fitting for crack length and the effect on the crack growth curve

5.3. EBSB Modeling Results

The results in this section pertain to determining how well the sliding box analogy can represent the real damage growth rate for a fatigue crack growth case. As discussed, this will be done by comparing the modeled curves, using an energy balance, to the experimental testing data. The qualitative and quantitative criteria that will be used for this comparison are listed below.

1. Qualitative slope of the curves da/dN versus ΔK_{eff}
2. Average RMSE to quantify the deviation between model prediction and experimental data.
3. Limit case performance in the initiation and final failure regimes.
4. Plastic zone analysis with DIC data.

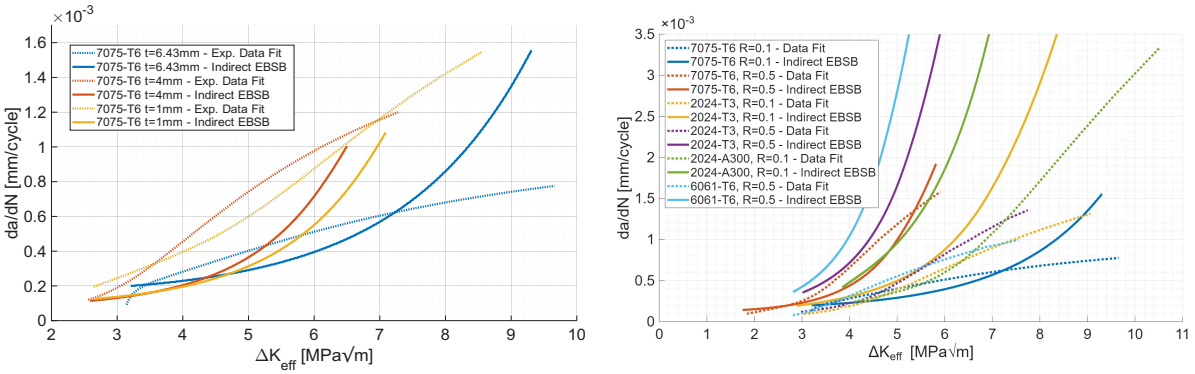

(a) 7075-T6 thickness variation crack growth rate results versus the EBSB model.

(b) Material and stress ratio variation crack growth rate results versus the EBSB model

Figure 5.6: Overview of all experimental data plotted over the EBSB results based on the original state of the model by Kuijk [13] (Irwin plastic zone).

General observations on the deviation of the EBSB modeled results from the experimental data, at room temperature only at this point, can be separated into thickness, and material variations. Figure 5.6a shows the results from varying the thickness between 1 and $t = 6.43$ in 7075-T6. A clear thickness dependence in how the solid curves (Indirect EBSB) predictions depart from the dashed experimental-fit curves can be identified. For the thickest specimen ($t = 6.43$ mm), the model begins reasonably close at low–moderate ΔK_{eff}. Then it exhibits strong upward curvature and progressively over-predicts da/dN at higher ΔK_{eff}, ultimately diverging well above the dashed fit. At intermediate thickness ($t = 4$ mm), the deviation is smaller and the model tends to be slightly lower than the dashed trend through much of the mid-range, with only a modest convergence or crossover near the upper end of the available

ΔK_{eff} data. For the thinnest specimen ($t = 1\,\text{mm}$), the model generally remains below the dashed experimental fit over most of the plotted range, indicating an under-prediction of the experimentally inferred growth rates. Overall, increasing thickness amplifies the tendency for the model to overshoot the experimental-fit curve at higher ΔK_{eff}, whereas decreasing thickness shifts the mismatch toward under-prediction and reduces the high-ΔK_{eff} divergence.

Across the different materials in Figure 5.6b, the deviation between the dashed experimental-fit curves and the solid Indirect EBSB predictions is clearly material dependent and is primarily expressed through differences in curvature and growth-rate acceleration with increasing ΔK_{eff}. For 7075-T6, the solid curve remains relatively close to the dashed fit at low-to-moderate stress intensity but becomes increasingly higher at larger ΔK_{eff}, indicating an over-prediction that grows with the stress intensity. In contrast, the 2024 alloys show larger divergence and earlier onset of strong upward curvature: both 2024-T3 and 2024-A300 exhibit model curves that rise more rapidly than their experimental counterparts over much of the mid-to-high ΔK_{eff} range, with the A300 variant showing the most pronounced high-ΔK_{eff} overshoot relative to the experimental trend. The 6061-T6 case displays the strongest mismatch overall, where the model response accelerates sharply and departs above the corresponding dashed fit at comparatively low ΔK_{eff}, suggesting that the present parameterization does not capture the more gradual experimental growth-rate evolution for this alloy. Overall, the deviation between collected data and the EBSB model increases when moving from 7075-T6 to the 2024 alloys and becomes most severe for 6061-T6, implying that the current formulation is not fully material transferable without more explicitly accounting for alloy-dependent energy dissipation or perhaps crack-tip constraint behavior.

5.3.1. Sliding Box Stiction Variation

In the previous section we observed some concerning deviation between the EBSB model and experimental results in the crack growth rate to ΔK_{eff} relationship. To ensure that the sliding box analogy itself remains sound with property variations, the assumption for the stiction coefficient, C_{stic}, needs to be investigated. Kuijk [13] used different varieties of this constant with values differing between $1-10^{-5}$ or 0.9999 and $1-10^{-8}$. To evaluate the effect of this constant the effect on the crack growth rate da/dN a range of C_{stic} is run through an otherwise identical simulation.

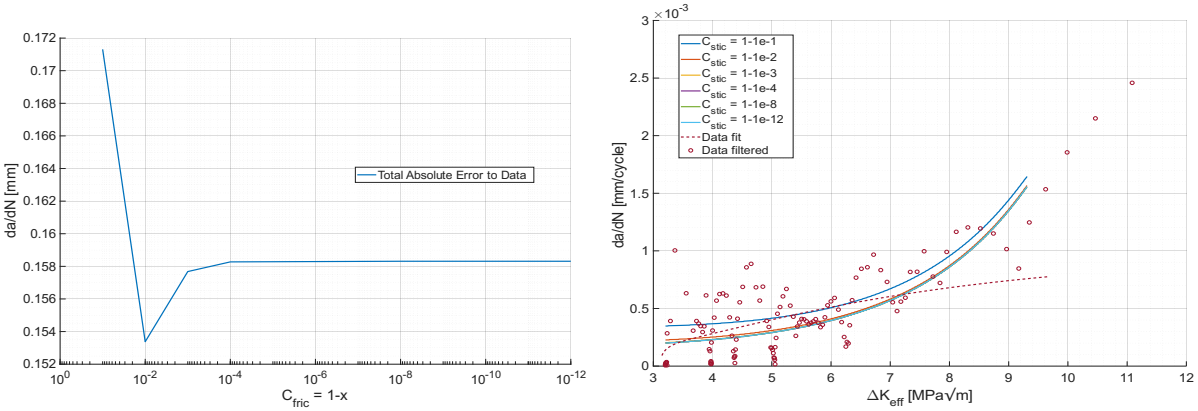

(a) Convergence study, with logarithmic x-axis, on the value of the constant C_{stic} applied on 7075-T6, 6.43 mm thick, at R=0.1. The value of C_{stic} is given as a function of $1-x$ on the x-axis.

(b) A comparison of C_{stic} variation between 0.9 and 0.999999999999. For context, the raw experimental data is also shown for the baseline 7075-T6 experimental run

Figure 5.7: EBSB sensitivity to C_{stic} variation analysis plots.

The investigation of the friction coefficient from the sliding box analogy is shown in Figure 5.7, where Figure 5.7a shows the crack growth rate converging for values of C_{stic} close enough to unity and diverging for values of 0.9 or smaller. This is expected but clarifies the cutoff, on the other hand the question arises, is this converged value the best choice for the constant or can it be varied as a scale factor for example. Looking at Figure 5.7b the effect on the da/dN-ΔK_{eff} curve is evident where a decrease in the stiction coefficient causes a shift up and left, increasing the crack growth rate at a value of the effective stress intensity factor. All curves, from dark to light blue are still very similar in shape,

with the gap seemingly only closing towards the highest stress intensity factors. Overall, as long as $1 > C_{stic} \geq 0.9999$, the EBSB model results in the lowest crack growth rates. The analysis shows this remains the correct value range to use for at least the analysis of the test results in this study as the trend, seen in most plots in section D.1, is generally that the EBSB overestimates da/dN. Therefore, minimizing the crack growth curve is beneficial to improve results and the value in the model is kept to 0.99999999 for all EBSB model runs in the coming sections.

5.3.2. Energy Balance Plastic Zone Variation

One way to determine a straightforward method for measuring the amount of deviation between the EBSB crack growth curve and the experimental data, is to use an error metric such as the root mean square error (RMSE). The RMSE is deemed a fitting metric as taking the square root preserves the relative ordering of model performance while expressing the error in the same units as input data. Because the residuals are squared prior to averaging, RMSE is also more sensitive to large deviations than the mean absolute error (MAE), placing greater weight on data points with large discrepancies [44]. Mathematically, the RMSE is defined as:

$$RMSE = \sqrt{\sum_{i=1}^{n} \frac{(\hat{y}_i - y_i)^2}{n}} \tag{5.1}$$

where $\hat{y}_i$ is a model predicted da/dN value for a ΔK_{eff} and y_i is a testing data point. The value of n is simply the total number of modeled or measured data points and $i = [1, n]$. The application of this error quantification metric to determine the performance of each plastic zone variation on the model output is displayed in Figure 5.8 below.

For 7075-T6 thickness variations, the RMSE shows a distinct, model-dependent sensitivity to thickness. At $t = 1$ mm, all three plastic-zone variants yield similar error levels, whereas at $t = 4$ mm the Irwin and Dugdale RMSE increases slightly while the Von Mises RMSE decreases. At $t = 6.43$ mm the trends diverge strongly: Irwin and Dugdale RMSE drop noticeably, but the Von Mises RMSE increases sharply and becomes the dominant outlier. Overall, increasing thickness affects the Von Mises-based approach most adversely, while Irwin and Dugdale appear more consistent at the highest thickness.

The RMSE results vary systematically with both material and stress ratio, and the observed trends are consistent with the differing plastic characteristics of the alloys. For 7075-T6, which behaves close to an elastic–perfectly plastic material, all three model variations achieve the lowest RMSE and exhibit only a modest sensitivity to R, indicating that the underlying assumptions in the plastic-zone approximations remain reasonably representative. In contrast, the 2024 alloys show a marked increase in RMSE and a clearer dependence on R, with higher stress ratio generally worsening the fit. This is put into perspective by the lower yield level and appreciable strain hardening of 2024, which alters the crack-tip constraint and plastic dissipation relative to the idealized perfectly plastic formulations. The deviation becomes most pronounced for 2024-A300, where the errors rise substantially and the separation between model variants increases, suggesting that material-specific hardening and ductile crack-tip behavior are not fully captured by the present energy balance formulation. For 6061-T6, which combines a low yield level, reduced strain hardening, but the greatest ductility, RMSE remains elevated. Across all conditions, the Von Mises-based variant tends to produce the highest RMSE, while Irwin and Dugdale generally perform better, but the overall degradation in accuracy from 7075 to 2024 and 6061 highlights the need to account for material properties in a different way rather than simply enlarging the plastic zone to account for increased energy dissipation when transferring the model between alloys.

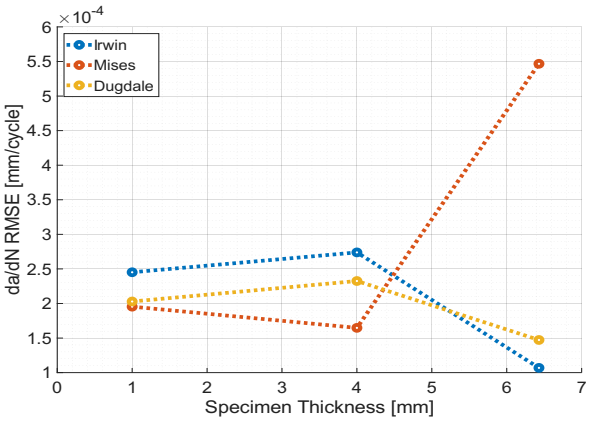

(a) RMSE across tested specimen thicknesses of 7075-T6 for Irwin, Von Mises, and Dugdale plastic zones.

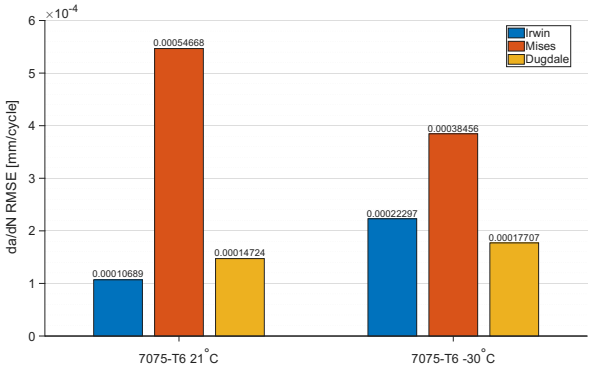

(b) RMSE - 7075-T6 Temperature Variations

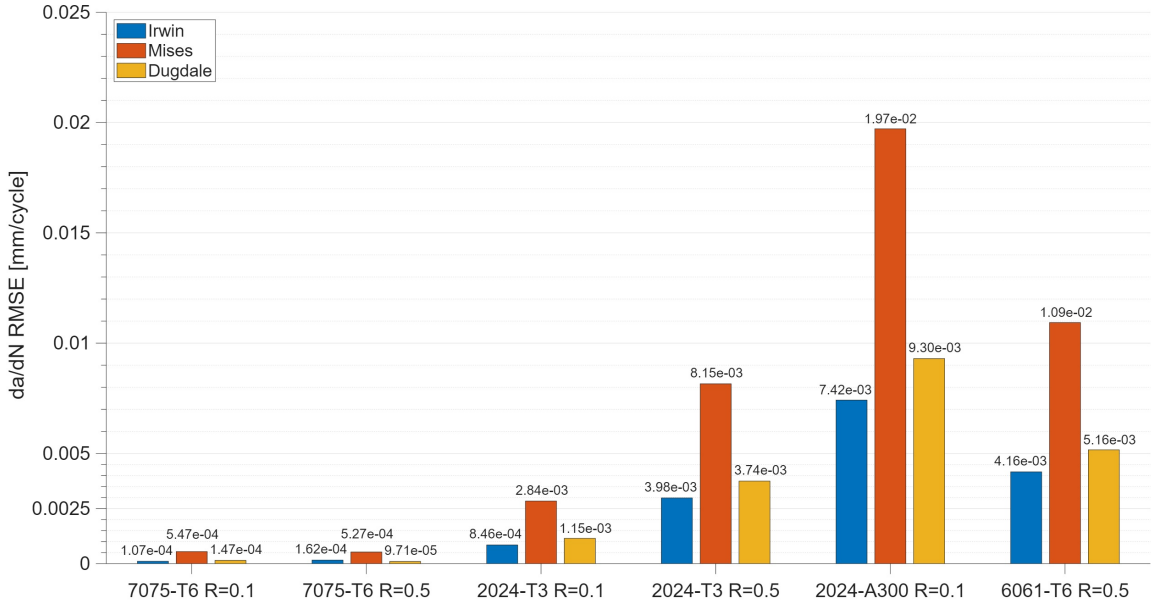

(c) RMSE across tested specimen materials and stress ratios for all compared plastic zones.

Figure 5.8: RMSE based overall error data for

5.3.3. EBSB at low temperatures

In order to evaluate the ability of the EBSB model, at low temperatures, to capture the fatigue properties of aluminum the model is compared to experimental results. The baseline test is the 7075-T6 plate which is 6.43 mm thick and tested at a stress ratio of $R = 0.1$. The results of the 21°C and -30°C fatigue tests are shown in detail in Figure E.3c and Figure E.3e respectively. The measured crack length versus cycle data was fit with a second order exponential curve to determine a smooth experimental crack growth rate curve. The $a - N$ curves and the exponential fits for the low temperature test are presented in Figure D.1a. The smoothed curve fit is shown for low and room temperature tests, to compare with the EBSB model employing the Irwin plastic zone, in Figure 5.9.

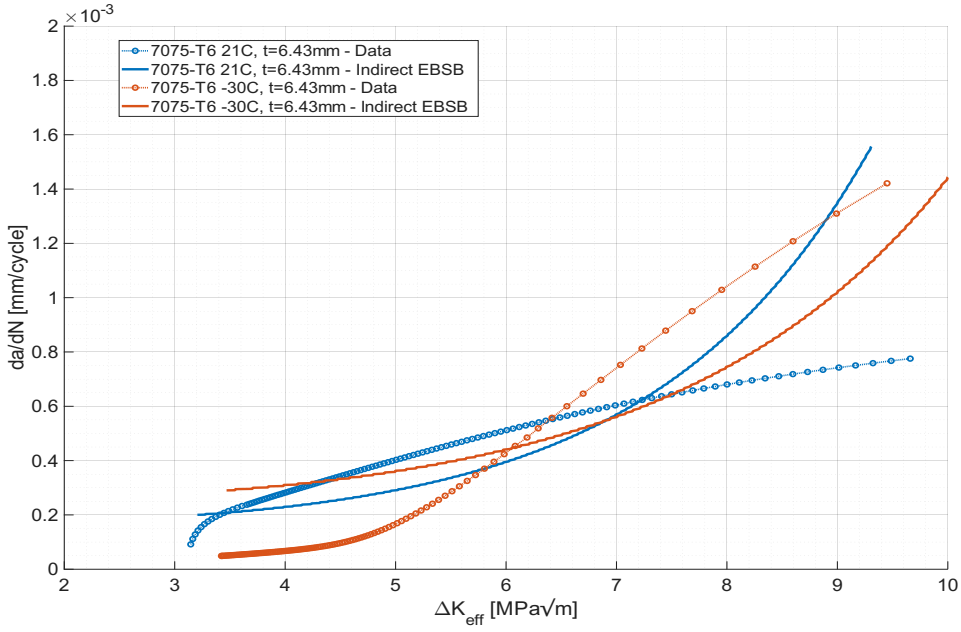

Figure 5.9: 7075-T6 temperature variation experimental crack growth rate results versus the EBSB model.

The differences between models is most comparable using the initial offset and slope of the curves. The order of magnitude of the EBSB remains correct between the room temperature and low temperature tests. The initial offset is very comparable for the room temperature curves where the initial slope of the experimental curve is greater but has a decreasing rate. The corresponding EBSB data has a greater rate of change of slope exceeding that of the experimental curve. At lower temperatures the initial offset is very large, with the EBSB overestimating crack growth rate. The crack growth regime after $\Delta K_{eff} > 6$ shows a more similar slope after the experimental results actually show a larger crack growth rate.

A reason that could cause this difference is that the dataset for crack growth rates at low temperature actually begins at the first cycle while the dataset for room temperature only once a crack has formed. This would imply that the EBSB initially overestimates crack growth rates if a time history from the before crack initiation is taken.

To further investigate the reasons for the offset and slope errors found in Figure 5.9, the plastic zone was evaluated from DIC imaging and compared to the EBSB plastic zone model. Figure 5.10 shows the progression of the total plastic volume with crack growth. Taking into consideration the incremental area method covered in subsection 4.5.5 the plastic volume can be extracted from DIC strain magnitude fields from processed image data.

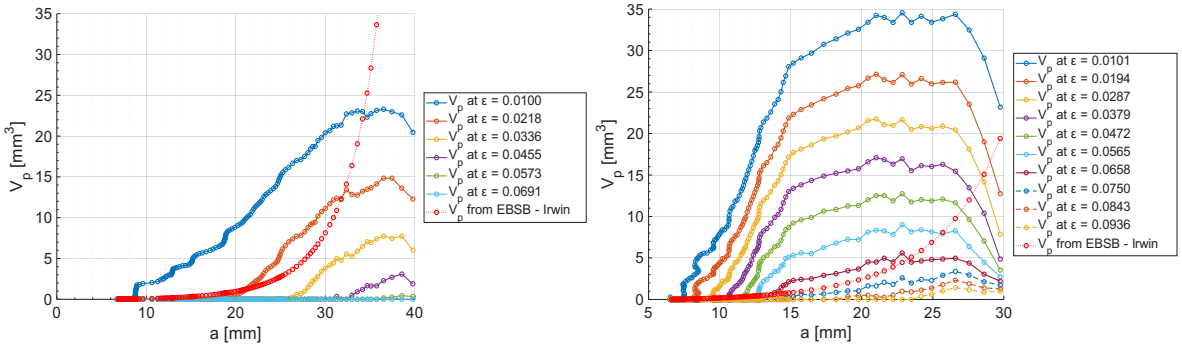

(a) 7075-T6, 6.43 mm thick, at room temperature.

(b) 7075-T6, 6.43 mm thick, at -30°C.

Figure 5.10: Total DIC plastic volume versus crack length at room and low temperature. Various curves are given at sampled strain points from the stress-strain curves of the materials above 0.2% offset yield.

To compare and contrast the plastic volume for experiments at room and low temperature we can plot the DIC strain field area for each test. From the strain field the measured plastic volume is given as a function of $V_p = A_p \cdot T$ at each iso-strain level. The process to determine the area at each iso-strain level was to sum up all pixels at the cut-off strain level or above and scale the area found in pixels by the scale factor determined for the specimen from the crack length measurement methodology. Therefore, the curves in Figure 5.10 show the cumulative plastic volume at or above each iso-strain level shown in the legend. An extension of this process would be to subtract the curves from each other to find the plastic area for each strain interval instead, this could be useful for determining the energy density of the intervals for example. The Irwin curve shows the modeled approximation for the plastic area growth, as it was used in the EBSB framework, of plastic area above the yield strain only.

In Figure 5.10a, the room-temperature test (7075-T6, $t = 6.43$ mm), the DIC-derived plastic volume V_p generally increases with crack length a once yielding is exceeded, and higher sampled strain levels produce larger V_p, consistent with progressive growth of the plastic region as the crack advances. For the low-temperature test in Figure 5.10b (7075-T6, $t = 6.43$ mm, $-30°$C), the same qualitative dependence on a is observed, but the $V_p(a)$ curves reach higher values and exhibit a steeper rise, implying larger dV_p/da and aligning with the expected change in material response due the higher tested nominal stress level. Differences in the stress intensity factor evolution between the two tests also influence the plastic-zone size and therefore the magnitude and growth rate of V_p, and this dependence is qualitatively reflected by the Irwin-based reference trend through its explicit dependence on K and the yield stress. The denser set of strain levels shown in the low-temperature plot may also be influenced by increased DIC sampling density employed for that dataset. Nonetheless, it is clear that the underestimation of the plastic zone is greater for the low temperature test when compared to the stress level adjusted Irwin plastic zone size.

In addition to these observations the saturation, and following decrease in apparent plastic volume, needs to be addressed. The reduction in V_p at larger a, and the earlier change from increasing to decreasing slope, is most plausibly a measurement artifact caused by the advancing crack producing zero strain ”holes” in parts of the DIC mesh, which reduces the effective area contributing to the V_p calculation. This topic will be addressed again in section 5.4. The phenomenon is related to the failure of the DIC mesh to adapt to the increasingly open crack at maximum cyclic load, where the DIC images were taken. Consequently, the valid portion of this plot is the region before $a = 25$ mm for the room temperature plot, and $a = 15$ mm in the low temperature plot.

5.4. Strain Field Analysis

As a result of the DIC measurements that were taken during fatigue testing it was possible to extract the displacement fields at $S_{\max}$. Using the Vic-2D postprocessing software it was possible to extract equivalent Von Mises strain values across the DIC mesh based on the formulation given by Equation 4.11. These can now be used to plot a sample of displacement fields to qualitatively look at the shape of the plastic zone and how it progresses. An important note on the DIC analysis in general is that the Von Mises strain calculation in Vic-2D uses a principal plane strain formulation, with $\epsilon_z = 0$, as out of plane deformations are not measured. This means that the values of strain magnitudes extracted in this manner are going to be conservative and may cause lower than expected values. However, although these values may be conservative, the stress state experienced by the material in the DIC images is still governed by the physical phenomena that are present. Therefore, their strain state will still be considered representative of reality.

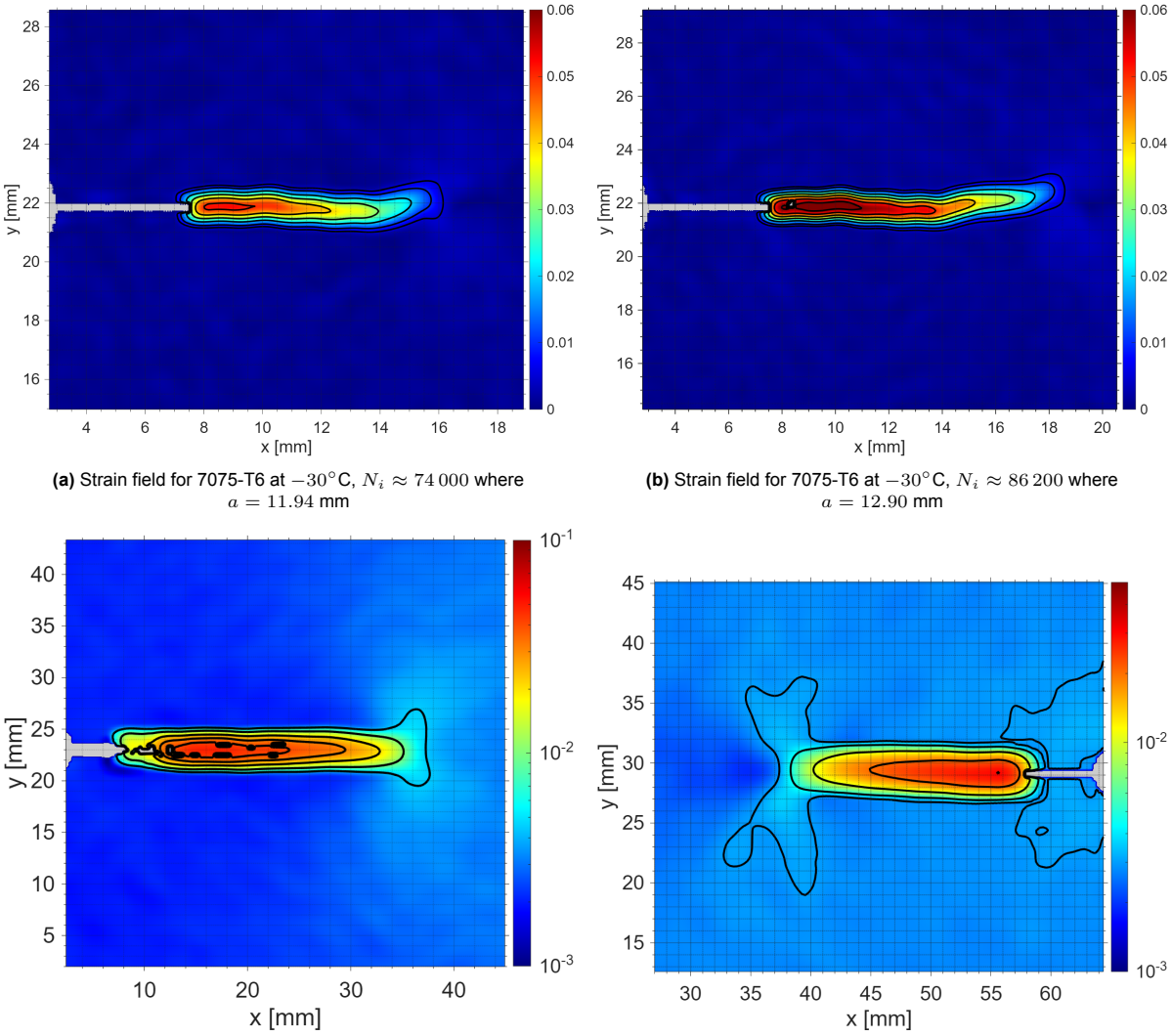

(a) Strain field for 7075-T6 at -30°C, $N_i \approx 74\,000$ where $a = 11.94$ mm

(b) Strain field for 7075-T6 at -30°C, $N_i \approx 86\,200$ where $a = 12.90$ mm

(c) 7075-T6 6.43 mm thick at room temperature, $N_i \approx 189\,000$ where $a = 33.57$ mm

(d) 2024-T3 at room temperature, $N_i \approx 141\,000$ where $a = 20.69$ mm

Figure 5.11: Relevant strain fields determined from DIC. Figures (a) and (b) are on a linear scale, and figures (b) and (c) are on a logarithmic color scale

For all strain field images, the iso-lines correspond to fixed strain levels. The first iso-line is set to 0.5% of the yield strain, the second iso-line corresponds to the yield strain assuming full yielding occurs with an 0.2% offset (i.e., $S_y = R_{p0.2}$), and the subsequent iso-lines are placed at full percent strain increments to improve visual differentiation of the color gradients (0.02, 0.03, 0.04 strain, and so on).

The progression of the plastic zone at low temperature is shown in Figure 5.11a and Figure 5.11b. These strain fields are presented on linear color scales and are therefore directly comparable. A bend is visible where the crack path deviated; similar deviations are also visible in Figure 5.4 and are commonly associated either with obstacles in the crack path, such as inclusions, or with the development of shear lips at the surface.

Strain fields on a logarithmic color scale are shown in Figure 5.11c and Figure 5.11d. The logarithmic scaling emphasizes low strain magnitudes, and in both cases the expected butterfly-like plastic zone shape is visible. The observed zone outlines are consistent in form with plastic-zone perimeters obtained from DIC reported by Lemmen [38], and the plastic zone thickness is again generally about 4 mm. The field in Figure 5.11d was recorded during the steady crack growth regime and shows a straight propagation direction, as well as stress concentrations around the machined pre-crack geometry.

The strain field in Figure 5.11c was captured close to the final cycle. The shown 7075-T6 specimen ($t = 6.4$ mm) at room temperature failed at 193,289 cycles, and an intensified strain field is visible around the un-cracked ligament. Multiple regions of opening are also visible along the crack, and the crack opening becomes sufficiently large that the DIC calculation no longer converges, resulting in zero values. This behavior is important for the later plastic zone size quantification. Another example of holes appearing in the mesh due to loss of correlation is shown in Figure 5.11b.

Overall, the plastic zone progression strip is visible in all strain fields. The Irwin plastic zone was overall the best assumption and appears to aligns with the consistent plastic zone strips as well as the blunt tip, visible in all the strain fields. The general resolution of these DIC images is in the range of 0.042 to 0.051 mm per pixel. The characteristic butterfly-shaped stress distribution is shown to be recreated on the images with logarithmic scales. They are similar to the findings of Lemmen [38] and Hogeveen [15].

6

Discussion

This chapter discusses the results presented in chapter 5. The discussion first addresses testing methodology and data processing, then reviews experimental crack-growth behavior and deformation constraint effects. It subsequently evaluates room temperature model performance and discusses comparisons with the low temperature results. The chapter then uses DIC-based plastic-zone and strain energy observations to investigate the plasticity terms of the energy balance. It closes with a critical review of the model assumptions and the limitations of the conducted research.

6.1. Discussion of the Testing Methodology

Using the same plate stock, specimen geometry, and test methodology throughout the quasi-static tensile property experimental campaign improved internal consistency and helped ensure that the resulting dataset is representative of the chosen specimen configurations. At the same time, the lack of repeated trials for fatigue tests eliminates the ability to quantify statistical variability and identify occasional anomalies. A larger number of repeated tests per condition, such as 5 or more, would therefore strengthen confidence in the trends by enabling a more robust assessment of scatter and repeatability.

The decision to vary the maximum stress in order to target approximately 200,000 cycles per test was effective in controlling total test duration and maximizing throughput, which was particularly important given the high demand on the fatigue equipment in the lab. However, this approach reduces direct comparability between tests because the loading levels are not held constant across the dataset. As a result, isolating the effects of individual changes, such as the influence of reduced yield stress between 2024-T3 and 2024-A300, becomes less straightforward than it would be with a fully comparable, constant-nominal-stress test matrix. Furthermore, the effects of each tested variable are not directly relatable to the fatigue performance of any specimen with relation to expectations from literature or physics. This decision was known and consciously taken in favor of a much improved spread of variations in the tests to be compared to the EBSB model. The research objective was limited to the ”expanding and validating the application” of the EBSB framework, which means at this stage the determination of an accurate finalized model based on isolated parameter adjustments is beyond the scope.

The DIC speckle pattern enabled strain estimation at the pixel scale, achieving a nominal strain resolution in the order of 0.05 mm [36]. In practice, however, the effective spatial resolution is limited by the selected subset and step sizes, which act as spatial averaging filters and reduce sensitivity to small-scale gradients, such as those close to the crack tip. Consistent with this limitation, the characteristic butterfly-shaped plastic zone reported in the literature [6][38] was only clearly resolved in the late stages of crack growth, close to final failure. However, the observed plastic zones in Figure 5.11 do align well with the results found by both Lemmen [38] and Hogeveen [15]. Their research showed an initial ”blob zone,” which eventually approximated a butterfly-like shape close to failure as well.

To obtain smooth and comparable crack growth rate data, second-order exponential fits were applied to the measured crack length histories prior to differentiation. While this approach improves legibility and reduces the dominance of point-wise scatter, it was observed that local changes in crack growth rate can be masked or distorted when the fitted curve deviates from the underlying measurement trend. This effect is most apparent near final failure, where crack growth accelerates and small differences in crack length tracking can lead to disproportionate changes in the derived da/dN.

The combination of limited spatial resolution in the DIC-derived fields and sensitivity in crack growth rate extraction highlights the potential value of more automated crack length measurement techniques. Approaches such as potential drop measurements, as employed by Kuijk [13], or higher-fidelity image capture combined with automated object tracking could reduce operator-induced variability and improve temporal consistency. Nevertheless, the visual crack tracking method adopted in this thesis, applied once the crack is clearly visible, represents a robust and pragmatic methodology for generating reliable crack length histories within the constraints of the experimental setup.

6.1.1. Changes to the Testing Methodology

During the experimental program, several modifications to the methodology were required due to limitations identified during setup and testing.

An initial target temperature of $-50°$C could not be achieved because the climate chamber's liquid-nitrogen cooling loop was non-functional. Instead, a stable test temperature of $-30°$C, $\pm 3°$C, was maintained using the chamber's high-voltage auxiliary cooling system. Mechanical constraints also affected the applied loading, as vibration within the clamping system imposed a maximum permissible load of 52 kN. The effect of these changes is likely not detrimental. The monotonic increase of properties shown in literature [4][25][26] implies that the trends seen in those properties between $21°$C and $-30°$C will be comparable, albeit less pronounced, to those observed at $-50°$C. The step in temperature in the low temperature experiment also remains significant at $-51°$C, which is almost 30% of the way to the cryogenic regime at $-150°$C.

Further adjustments were required when it was clarified that the 100 kN MTS fatigue machine is not large enough to fit any of the available climate chambers. As a result, the test setup was relocated to the 250 kN MTS machine, and the cold-temperature quasi-static tests were subsequently performed under displacement control on this setup as well. The setup for cold tensile tests remained identical to the one for low temperature fatigue and is shown in Figure F.1.

The material configurations of the 2024-T3 and 2024-A300 specimens were opposite to the initial L-T specification due to an error that was made in cutting up the stock plate. Therefore, the rolling direction was perpendicular to the loading axis, as in the T–L configuration described in subsection 4.2.2. This was used as an additional variation to compare to the EBSB model. Concerning the orientation change to T-L in comparison to the regular grain orientation in the direction of rolling, L-T, the assumption was that the effects can also be captured by the EBSB model. A fundamental assumption of the EBSB framework is that the quasi-static properties of the material will capture the alloy, grain orientation, and thickness-related material inconsistencies, as well as other environmental and temperature effects. These case-specific properties are then represented by the yield stress and stiffness variables used in the energy balance and were presented in Table 5.1 and Table 5.2. The exact difference between the two grain orientations is shown in Figure 6.1, where it is evident that the only significantly affected property was the yield regime behavior of the T-L specimen.

Finally, although quasi-static testing was originally intended to employ extensometers, these instruments were damaged shortly before testing commenced. Consequently, digital image correlation was also used in all quasi-static tensile tests to ensure reliable deformation characterization. This choice will increase the post-processing workload but will be unlikely to affect the measurement resolution significantly. The specimen-to-specimen material variation, which is visible for the T-L specimen in Figure 6.1 for example, is already bigger than the order of magnitude to which a typical DIC virtual extensometer is accurate to, i.e., 100 micro-strain [36].

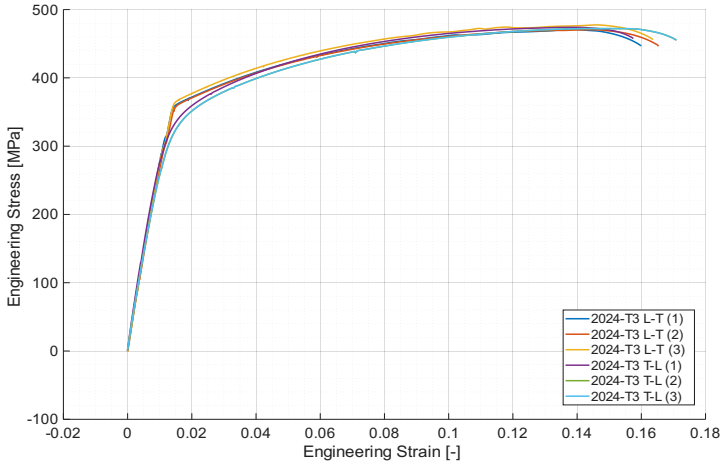

Figure 6.1: Engineering stress-strain curve comparison for 3 trials each of 2024-T3 with rolling direction L-T and T-L for comparison. Cross-head displacement based strain calculation was used here due to lack of DIC data for L-T specimen.

6.2. Discussion of Experimental Results

In interpreting the experimental results, it is useful to first frame the expected low-temperature mechanisms and then relate them to the observed variability across the test program. In general, low-temperature property effects were broken down into increased strain hardening and increased yield, while some materials such as aluminum may also show changes in ductility [25]. To account for these effects, a variety of materials were tested that successfully showed variations in all of these aspects, producing a corresponding range of results.

Appendix B presents the test matrices for each of the tensile and fatigue tests, showing that there were quite a few outliers. The removed outliers necessitated repeated experiments to recreate some of the missing data. This section will give an overview of the outliers and what caused the specific problems, followed by a discussion of the plotting methods, the low-temperature tests, and the observed trends relating to the stress state assumptions.

All fatigue tests were designed to reach a target of 200,000 cycles, with a small number of deviations arising from limitations in using Paris-curve predictions based on imperfect material data. The 6061-T6 test at ($R = 0.1$) was not completed for this reason, although the ($R = 0.5$) case provides a representative baseline, and its model–data deviations are shown in Figure 5.8c. Additional deviations occurred for 2024-A300, which terminated after 40,000 cycles. A further outlier was the removed 1 mm 7075-T6 trial: an accidental overload was followed by 550,000 cycles without crack initiation, whereas a repeat test at a slightly increased constant load failed at a more typical 120,000 cycles. Worth mentioning in this context is that the current EBSB framework is not capable of capturing overload or variable-amplitude loading effects.

Collectively, these outcomes also highlight the sensitivity of the data-fit-dependent approach to the Paris parameters. All tests were sized according to Paris constants that were obtained from various sources, see subsection 4.3.2, to attempt to size the constant amplitude load. The deviations show that a more repeatable methodology, grounded in directly measurable mechanical properties under the relevant environmental conditions, would improve the predictive modeling capability. This frames the strength and goal of the energy balance with the sliding box framework well.

6.2.1. Plotting of Results

Figure 6.2 provides an overview of how using a linear–linear plot for analysis differs from the conventional log–log representation of crack growth rate versus ΔK_{eff}. In both example plots, a Paris-type curve fit is shown using a least-squares approach. On the linear scale, deviations that lead to overestimation of da/dN become more apparent, while small variations at low da/dN that do not follow an exponential trend appear less pronounced. Conversely, the log–log plot linearizes the Paris relationship, making curvature less evident and reducing the visual impact of vertical offsets between curves,

but it also amplifies scatter in the measured crack growth data. To better assess how the slopes of the model and experimental curves evolve, and to quantify the true offset between them, presenting the data on a linear scale is therefore the more informative choice for the comparisons of any results.

Additionally, with regard to experimental results, during analysis, strong variations in calculated growth rates were sometimes introduced by noise attributed to the manual crack front selection process. This motivated the use of a least-squares second-order exponential fit to crack length versus cycles data to stabilize the derived da/dN. In retrospect, this smoothing step may not always have been optimal, since several comparisons indicate that the model can track the raw data trends closely when the pointwise values are retained. This is illustrated in Figure 5.7b, where the model alignment with the measured data points actually appears stronger than the alignment with the fitted curve. The reason for this is that the initial fit was done on the crack length data rather than the crack growth rate da/dN in an attempt to reduce noise. As a result, it is important to look not just at the plots of the continuous fits that display awkward curvatures with respect to the EBSB and collected data. This is most true for 7075-T6 tests at 4 mm, 6.43 mm, and 6.43 mm at $-30°$C.

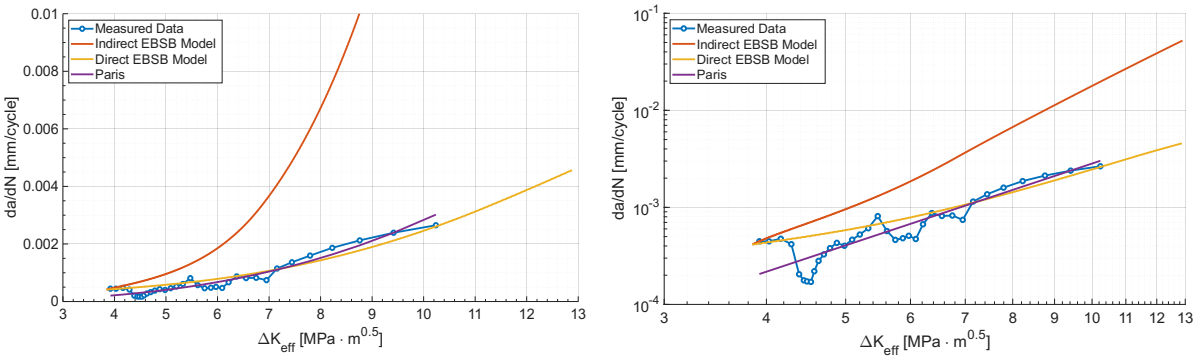

(a) 2024-A300 crack growth data on linear axes

(b) 2024-A300 crack growth data on log-log axes

Figure 6.2: Comparison of crack growth plots on linear axes and log-log axes as is common for analysis of the ”Paris curve”

6.2.2. Transition Between Plane Stress and Strain Conditions

The assumption has been made from the start that the assumptions of the stress state in a thin pre-cracked plate would be one of plane stress. For simplicity this assumption was applied throughout the period of crack propagation in an unchanged manner. The results gathered from experimental testing, however, indicate that transitions were present, as was discussed in section 5.2.

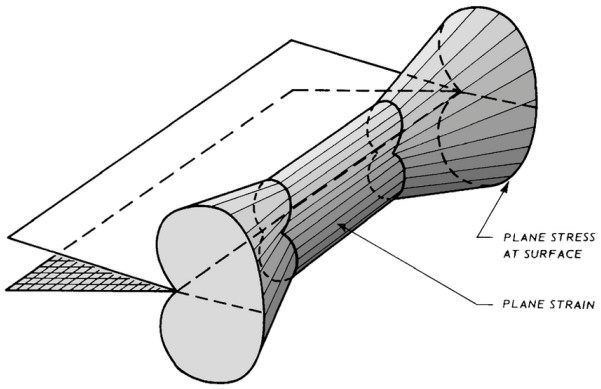

Figure 6.3: Changing conditions through a plate’s thickness from plane stress to plane strain. Illustrated by Janssen et al. [45].

Accounting for the coexistence and transition between plane strain and plane stress conditions is also consistent with independent observations of the fracture surfaces. In particular, the emergence of deformations similar to shear lips toward the latter stages of crack growth and fracture provides some evidence of a transition from plane strain-dominated behavior to plane stress-dominated fracture near

the specimen surfaces. This suggests that the current modeling framework, which relies primarily on plane stress assumptions throughout crack growth, likely overestimates crack growth rates during the early stages of propagation when constraint effects are strongest. Improving the stress state assumptions would therefore improve the physical fidelity of the crack growth predictions, especially in the early and transitional crack growth regimes. Especially the 7075-T6 tests showed evidence of the mentioned transitions with late-stage improvements of the model similarity with collected data in the plots of da/dN versus ΔK_{eff}.

6.3. Discussion of the Room Temperature EBSB Model Results

In the analysis of the EBSB model against experimental data, the focus primarily was on the plastic zone energy terms and the F_{stic} since those are the terms identified in the methodology for investigation. To recap, the forcing function from Kuijk [13] is a sensible approach with an opening stress correction, but the definition of F_{stic} appeared arbitrary. The plastic zone size was also adjusted, as it is an assumption-based term. There are many options and corrections available for the plastic zone size, making it straightforward to manipulate. Additionally, the function for dU_p/dV_p is based on an energy density curve fit as well. The crack surface energy creation term is easy to adjust but already clearly defined and likely to be close to reality.

In general, the test results show that the EBSB model, using the indirect approach to incorporate the energy balance, was not consistent and usually severely overestimated crack growth. The approach that was given in the methodology was to adapt the assumptions on the plastic zone to attempt to increase plastic energy dissipation, which was expected for cold environments. The result of manipulating the plastic zone between Irwin, Dugdale, and Von Mises did not improve the modeling accuracy for any material or stress ratio variations.

An exception to the worsening trend for plastic zone replacements was the 7075-T6 thickness variation between 1 mm and 6.43 mm. In this comparison from Figure 5.8a both Dugdale and Von Mises plastic zones were found to decrease the error between model and experimental data for the 1 mm and 4 mm thick specimens. The opposite relationship is observed at 6.43 mm thickness, with Irwin becoming, by an RMSE error margin of almost 0.45 μm/cycle, the best approximation versus Von Mises. A possible reason for this change-up could be the transition from plane stress to plane strain, which has been briefly discussed in subsection 6.2.2.

As shown later in section 6.5, the measurable plastic volume growth per increase of the crack length is even higher in the experimental than the modeled volumes. This implies that currently the average plastic energy density defined by Kuijk [13] is likely being overestimated to account for the low plastic volume. Using bilinear stress-strain relations or implementing nonlinear elastic-plastic models for the plastic energy density seems promising to develop an energy density that depends on material properties in isolation. An example of this is the derivation done for Equation 6.9 as well as DIC data extracted to define the plastic volume in Figure 5.10.

6.3.1. Comparison with a Paris Curve

As stated previously in this report, the Paris curve is likely the most well-known method for calculating constant amplitude fatigue crack growth behavior. For this reason it is of interest how well the EBSB model approach lines up with this empirical method.

The observation across tests showed that the indirect EBSB model was not consistently suitable to accurately model fatigue, as mentioned in the previous section. We can relate the model to the characteristics of a Paris curve fit, however. An example is shown with the EBSB model and data in Figure 6.2, representing the differences between models with respect to the most unfavorable room temperature test. This was the fatigue test of 2024-T3 overaged for 15 hours at $300°$C to 2024-A300.

Before comparing the curves, we will quickly go over the process for determining the Paris constants. Simply apply a linear regression using a least squares approach when plotting $\log(da/dN)$ against $\log(\Delta K_{eff})$ [46]. The output formula will be in the format:

$$\log\left(\frac{da}{dN}\right) = \log(C) + m\ \log(\Delta K_{eff}) \tag{6.1}$$

where the Paris constants are given by the values C and exponent m. They may be quantified as $C = 4.83 \cdot 10^{-13}$ and $m = 2.80$ for this plotted example using the Paris relation:

$$\frac{da}{dN} = C\left(\Delta K_{eff}\right)^m \tag{6.2}$$

The curves produced by the EBSB model and the fitted Paris curve in Figure 6.2a show the surprising accuracy of the direct sliding box results. The nature of curvature of all curves matches in the linear plot where a non-linear relationship is visible that is monotonically increasing. This indicates that in general the EBSB model, regardless of its specific accuracy, produces curves with the correct nature of curvature. This was observed for all fatigue tests, which also showed the model to start and progress in the same order of magnitude. The logarithmic plot of Figure 6.2b confirms this. By nature, the Paris curve is a straight line here, but also the EBSB model curves follow a largely linear trajectory. The fact that both EBSB model curves transition from an initial linear slope to a secondary one reveals that a transition occurs. This change in slope could indicate the ability for the EBSB framework to capture the change from the Paris growth regime to the stable tearing regime of fatigue.

6.4. Discussion of Low Temperature Results

The room-temperature results were used to motivate and simulate the expected trends in material behavior at low and cryogenic temperatures; in addition, one fatigue experiment and one quasi-static tensile test were performed at $-30°$C, and the differences observed in this test are discussed in this section.

A key research question posed in section 3.1 concerns the extent to which a physics-based EBSB approach to crack propagation can capture the fatigue characteristics of aluminum alloys at low temperatures. This question can be addressed using the low-temperature test results and by evaluating whether the EBSB framework can adapt to the associated property changes in aluminum, including trends expected toward cryogenic conditions.

Experimentally, the $-30°$C tensile test in Figure 5.2 showed an increase in work hardening of approximately 20 MPa, a similar yield strength, and a significant decrease in ductility. The reduction in ductility contrasts with the behavior often reported at cryogenic and even at moderately low temperatures, where studies such as Duthil [25] and Wang et al. [47] describe and show a dual-enhancement effect. The effect is associated with higher strain hardening rates and improved dislocation motion during deformation, allowing greater deformation before failure. The fact that this observation was not recreated in the tensile experiment is concerning. The only difference between the room temperature tests and the low temperature test is the change of testing machine. Alternatively, other environmental factors may have affected the results, such as humidity, which the climate control system did not have any control over. In spite of the difference in the ductile failure point, the yield stress and strain hardening effects were confirmed. Given that DIC showed a large portion of the plastic zone being in the strain range of 1% to 10%, the effect of reduced deformation before failure was likely minimal. For future research, the quasi-static tensile test results should be recreated and alignment with the effects found in literature ensured.

In the results, Figure 5.9 shows a comparison based on the exponential crack length curve fit to reduce the noise in the experimental data. However, this exponential fit to the a-N curve, shown in Figure D.1a for the temperature variation, does not capture the crack growth rate well for room temperature 7075-T6 at 6.43 mm thickness. For this reason, it is better to visually compare the effects at low temperature using the plots shown in Figure E.3 using sub-figures c and e. Surprisingly, in contrast to the material variations that represent property effects similar to those at low temperatures, the indirect method with the full energy balance was a better fit at both room and low temperatures. Furthermore, the final failure point between low temperature and room temperature also differs. The value of ΔK_{eff} already takes into account the difference in maximum nominal stress between the two tests, yet the last cycles before failure happen a whole 2 Mpa$\sqrt{\text{m}}$ of stress intensity apart. The discrepancy indicates a lower value for K_C, the fracture toughness, which is the opposite of the expected result at low temperatures. This finding would indicate an effect of the reduced failure strain observed in the quasi-static test.

The detailed fatigue results at low temperatures and the original Irwin-based EBSB model are presented in Figure 6.4. At low temperature specifically, the indirect EBSB approach appears to more accurately capture the crack growth rate in the ΔK_{eff} range of $[7, 9.2]$. Both the direct and indirect models show an initial overestimation of the crack growth equivalent to a difference of approx. 2.5 mm/cycle. The direct model keeps this offset more or less until failure. A potential explanation for the offset can be seen in the crack length calculation method and the modeling starting point, which will be discussed next.

A distinguishing aspect of the $-30°$C experiment is that crack growth was not measured based on the visual crack front. Instead, it was interpolated from specimen compliance using a DIC virtual extensometer placed across the crack at the center of the plate. The virtual extensometer allows connecting the reduction in effective stiffness to crack length. Five measurement sample points (including the starting length of the pre-crack and the final failure crack length) were taken where the crack was clearly identifiable on the visible side inside the climate chamber. These were used as fixed reference points to interpolate between. Based on this method, the data and the EBSB model results were determined starting at the initial machined pre-crack length of 6.5 mm. The initial guess for crack driving energy from the EBSB framework is the value $U_{\max,0}$ and assumes immediate crack propagation. This assumption will only be valid if a measurable crack is already visible and the crack has reached the stable Paris regime (as used to determine the Paris constants as well).

This limitation of the initial energy guess, made in the EBSB framework, defines the lower bound interval of its validity. For future investigation, this validity bound requires starting the modeling process after the first visual crack measurement point to ensure a comparison with data begins in the stable crack propagation regime (Paris region [8]). An inflection point on log-log scales is present around $\Delta K_{eff} = 7$, indicating the stable tearing regime described by Paris [8], and indicates that in the presented low-temperature test, the EBSB framework is likely valid in this region as well.

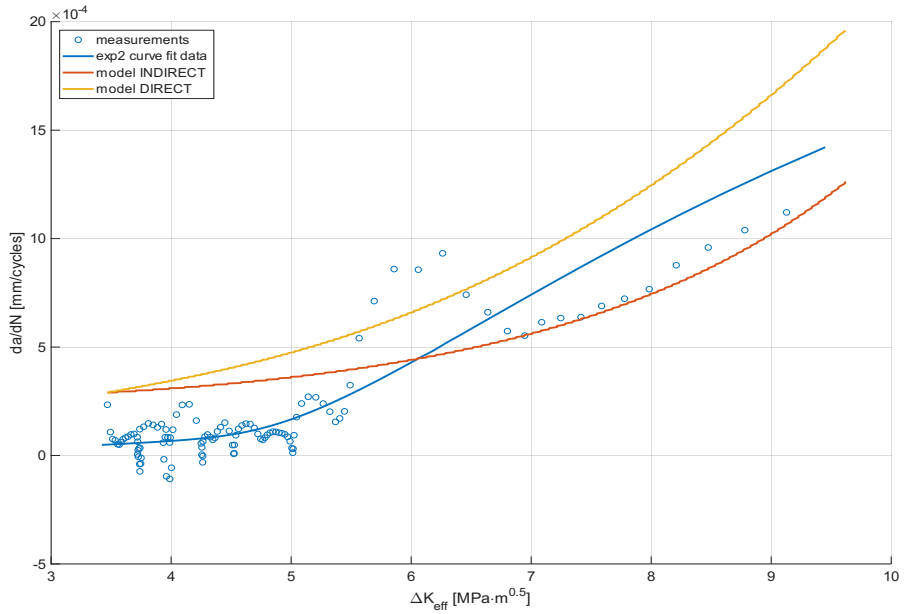

Figure 6.4: 7075-T6 R=0.1 t=6.43 mm at low temperature ($-30°$C) - da/dN versus ΔK_{eff} with experimental data, indirect, and direct EBSB model with Irwin plastic zone.

Overall, it can be stated that the EBSB framework was able to capture the fatigue characteristics, as they were present in the low-temperature test of this thesis, to a large extent. Initial offset for 7075-T6 remains an issue but was also present in the results shown by Kuijk [13]. However, the energy balance-based model, using the Irwin plastic zone, was able to recreate the exponential growth curve measured in the low-temperature experiment at larger effective stress intensity factors. The changes expected in the fatigue characteristics at low temperature were not conclusively demonstrated. While the stress level had to be increased significantly for the low-temperature test, the number of cycles

to failure was also reduced, and the critical stress intensity factor was reached earlier than at room temperature. These aspects make it difficult to make conclusive statements about visible effects due to increased yield strength and strain energy absorption of the material. Furthermore, the tests indicate that the interval where the EBSB model can realistically model the fatigue damage growth lies within the Paris region and the stable tearing region.

6.5. Verifying the Plastic Zone Size with DIC

From the DIC captures made during the experiments, we have already extracted strain fields and the related plastic volumes with the assumption of no through-thickness effects. The next step would be to attempt to relate and make comparisons between the measured plastic volume growth rate dV_p/da with the rate modeled using varied plastic zone formulations in the EBSB framework. The volume growth rate is calculated with the relation $dA_p/da \cdot T$ from the plastic area determined with DIC.

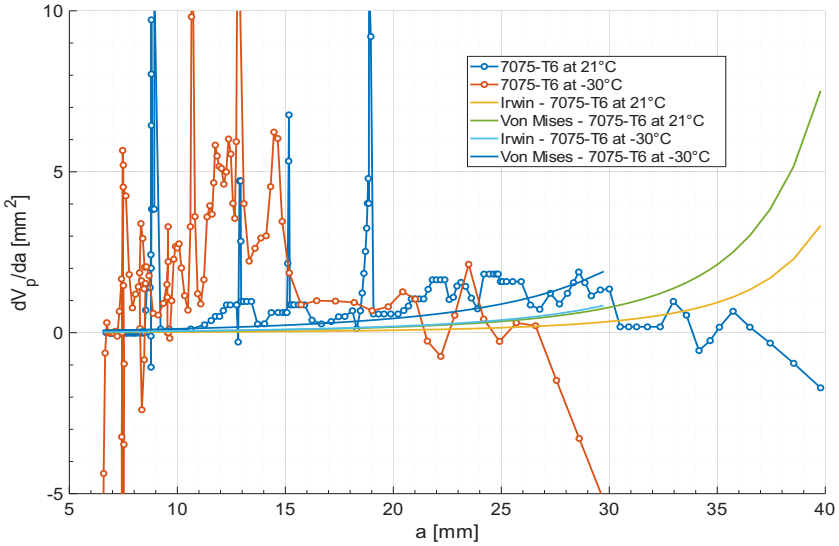

Figure 6.5: Comparison of the measured volume growth rate for 7075-T6 (T=6.43mm R=0.1) at room temperature and $-30°$C. The Irwin and Von Mises model approximations are from the energy balance.

Figure 6.5 shows, in more detail, the actual effect on the energy balance term dV_p/da of changing the plastic zone assumptions between Irwin and Von Mises. Dugdale is left out at this stage since it lies between the upper bound Von Mises and lower bound Irwin zones. In the plot, a clear cumulating positive offset is observed for the low-temperature test, yet while the Von Mises curve is the closest approximation to DIC data, it performs the worst in the EBSB model. The room temperature specimen actually shows some similarity to the growth rate of the Von Mises plastic zone growth approximation, as was initially predicted, but still underestimates overall.

As in Figure 5.11, the holes identified in the DIC mesh, due to the crack opening displacement, caused some cells in the mesh to stop converging to a displacement value and resulted in a standard zero strain. As in the plastic volume shown in Figure 5.10, the $-30°$C trial is affected by 14 mm of crack length, and the room temperature fatigue test by approximately 25 mm. The effect is the rapid decrease in volume growth rate, even to negative values. In opposition to this observation, the expectation is that the actual variation in the plastic volume would be less severe than the recorded exponentially growing $-30°$C curve of dV_p/da. This may also indicate that the interval of $a = [16, 25]$ could be a more realistic measurement interval of plastic growth rate. However, the beginning of DIC-related hole appearances can be shown to correlate to the decreasing growth trend in Figure 5.11b, which shows low strain spots appearing at approx. $a = 13$ mm, providing evidence to the DIC measurement problems.

Overall, this leads to the likely conclusion that the energy density curve is not attuned to the present test conditions or plastic zone formulations other than the one from Irwin. For this reason, the method appears to be the one that produces the least amount of deviation from the collected data. Again,

this is adjusted for by the average plastic energy density term from the EBSB framework dU_p/dV_p. All in all, the arguments presented in this discussion continue to indicate that crack growth for 7075-T6 is modeled closely to data in spite of an underestimated plastic zone size and growth. In the case of other materials, the model consistently overestimates crack growth, while using increasing approximations of the plastic zone only worsens this trend, as seen in Figure 5.8.

6.6. A Detailed Look at the Energy Balance

In this section we move on to discuss the implementation of the energy balance in the EBSB model. From a modeling perspective, the choice among basic plastic zone formulations primarily introduced constant scaling differences in the predicted dV_p/da, and therefore has a limited influence on the overall response compared with other plastic modeling assumptions. The error analysis in section 5.3 indicates that the Irwin-based plastic zone provides the most consistent agreement with the proposed plastic energy density formulation, while the Dugdale and Von Mises variants offer comparatively less improvement for the tested conditions. We also found in the previous section that the plastic zone size isn't being overestimated; rather, the opposite. This all leads to a similar conclusion: there is likely a discrepancy in the remaining term dU_p/dV_p.

Based on the process presented in subsection 4.5.5, we can determine an alternative value to the average plastic energy density that was curve fitted by Kuijk [13]. Using the plastic strain energy density instead, we would then have a parametrically defined and measurable new value. The consequence of choosing this formulation will be covered in the next section and is related to the lack of a sort of "damping" term to account for the crack shielding aspects of plastic zones.

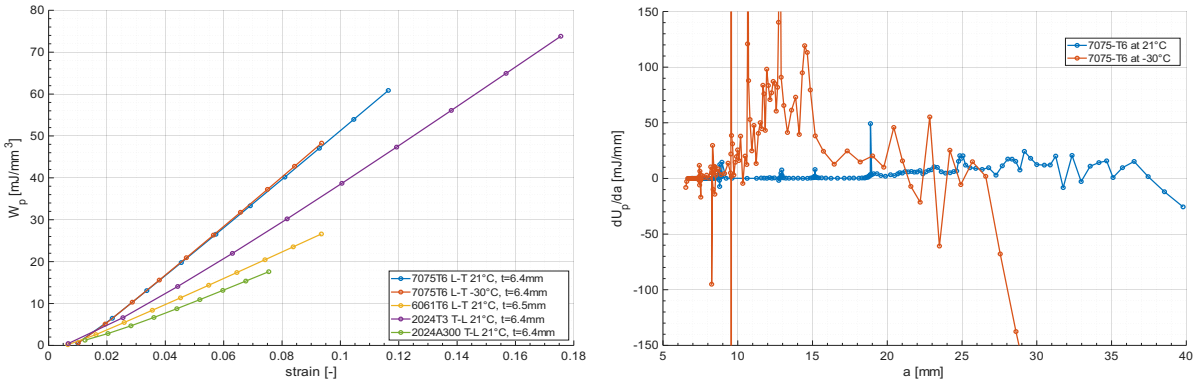

(a) Plot of purely plastic strain energy density W_p versus strain to get an overview of the plastic strain energy density under the stress strain curve.

(b) Plot of versus crack length to get an overview of the plastic strain energy density under the stress strain curve.

Figure 6.6: Figures relating the DIC plastic zone to the strain energy density.

The plastic strain energy density is shown in Figure 6.6a. The trend for most curves is a monotonically increasing, almost linear line. The greater the amount of strain hardening, the greater the initial curvature should be, as seen with 6061-T6 and 2024-A300. The ultimate stress and post-ultimate stress behavior relate to the slope of the closely linear portion of the curves. A clear example of this is shown by the low-temperature 7075-T6 curve. Initially, it matches the room temperature curve almost exactly, then at a strain over 0.06 or 6%, the curve departs to capture greater strain energy due to the increased strain hardening observable in the stress-strain curves shown by Figure 5.2.

The value of the plastic energy dissipation increment related to crack growth dU_p/da was calculated with the values for $[dV_p/da]_i$ from Figure 6.5 at the various iso-strain intervals listed within the figure. The following equation is used together with the plastic strain energy density from Figure 6.6a calculated for the same number (n) of iso-strain levels.

$$\frac{dU_p}{da} = W_{p,n} \cdot \left[\frac{dV_p}{da}\right]_n + \sum_{i=1}^{n-1} W_{p,i} \cdot \left(\left[\frac{dV_p}{da}\right]_i - \left[\frac{dV_p}{da}\right]_{i+1}\right) \tag{6.3}$$

Effectively, this is a close, but conservative, approximation of the actual energy present by summing up the intervals between each iso-strain curve for the increasingly energy-dense strain zones from DIC. Since the input value of the plastic volume growth dV_p/da has been differentiated with respect to the noisy experimental data for the crack length a, it inherits the noise but has been filtered with another "rloess" function with a low smoothing interval of 6 points. This is the case for both low-temperature and room-temperature 7075-T6 ($T = 6.43$ mm and $R = 0.1$) curves.

Overall, the process shown above is an example of how the plastic energy can be calculated from DIC images without the use of FEA or other tools. It shows that due to the monotonically increasing, almost linear W_p curve, the value for the plastic strain energy dU_p/da is also only increasing for larger plastic zones as a consequence of the increasing value of dV_p/da. An improvement to this method would be the use of a formulation that uses a continuous function for W_p to apply to each measured strain element in the strain field individually. A predictive capacity can be developed using, for example, the continuous stress distribution from Irwin given in Equation 2.37. This stress field was coincidentally also used to define the Irwin and Von Mises plastic zones, but more accurate representations exist in literature.

6.6.1. A New Formulation for the Plastic Energy Dissipation

In this chapter we have already mentioned that the difference between the plastic volume in reality and the plastic volume that is calculated is significant. This holds true in magnitude as well as in the growth rate of the crack length; this was especially true for the low-temperature test of 7075-T6 in the interval $a = [6.5, 15]$. This is shown in Figure 6.5, comparing the test data to Irwin and Von Mises plastic zones. In spite of this, a much higher than expected crack growth rate was predicted by the EBSB model, similar to reality. As a result, there is a motivation to outline an alternative new implementation of plastic energy density, which can be combined with other plastic zone definitions in future studies.

The concept of the new formulation is to define a strain energy density based on the quasi-static stress-strain curve and properties. The strain energy density can then be implemented with any plastic zone approximation (A_p) to calculate a more advanced version of the plastic energy dissipation term, dU_p/da. We can start by reiterating the strain energy density defined as such in the methodology Equation 4.12.

$$W_o = \int_0^{\varepsilon} \sigma d\varepsilon = \int [d(\sigma\varepsilon) - \varepsilon d\sigma] = \sigma\varepsilon - \int_0^{\sigma} \varepsilon d\sigma \tag{6.4}$$

From here on we will be working with the notation σ and ϵ for stress and strain tensors. The strain energy density can be combined with a parametric Ramberg-Osgood stress-strain curve [48] [24]. The Ramberg-Osgood equation is given in Equation 6.5 and can be easily matched with the empirical terms α and n to the quasi-static tensile results.

$$\varepsilon = \frac{\sigma}{E} + \alpha \left(\frac{\sigma}{E}\right)^n \tag{6.5}$$

Which, assuming a 0.2% yield offset for σ_y as it was used in the quasi-static data analysis, simplifies this relation to Equation 6.6. The only remaining parameter to determine here is now "n."

$$\varepsilon = \frac{\sigma}{E} + 0.002 \left(\frac{\sigma}{\sigma_y}\right)^n \tag{6.6}$$

Combining Equation 6.6 with Equation 4.12 is now possible. To contextualize this calculation for the equivalent Von Mises strain components determined from DIC, for example, we can find values of measured equivalent plastic strain, ϵ_v, that correlate to a stress level as determined from Ramberg-Osgood. As a result, defining the plastic energy density per infinitesimal volume at a stress level σ_v as:

$$W_p = \frac{dU_p}{dV_p} \approx \sigma_v \epsilon_v - \int_0^{\sigma_v} \left[\frac{\sigma}{E} + 0.002 \left(\frac{\sigma}{\sigma_y}\right)^n\right] d\sigma - \frac{1}{2}\sigma_v(\epsilon_v - \epsilon_y) \tag{6.7}$$

$$\frac{dU_p}{dV_p} \approx \frac{1}{2}\sigma_v(\epsilon_v + \epsilon_y) - \frac{1}{2}\sigma_v \left(\frac{0.004 \left(\frac{\sigma_v}{\sigma_y}\right)^n}{n+1} + \frac{\sigma_v}{E} \right) \tag{6.8}$$

Now, for example, for a constant stress and strain area from a DIC plastic zone strain field divided into iso-strain regions A_i, we can define the plastic volume for a constant thickness T:

$$U_p \approx \sum^{A_i} \left[\frac{1}{2}\sigma_{v,i} \left(\epsilon_{v,i} + \epsilon_y - \frac{0.004 \left(\frac{\sigma_{v,i}}{\sigma_y}\right)^n}{n+1} + \frac{\sigma_{v,i}}{E} \right) \cdot A_i \right] \cdot T \tag{6.9}$$

This is the summation across i steps of plastic iso-strain regions; as $i \to \infty$, this becomes the analytical total strain energy. The process of using this energy summation step is similar to the one defined in subsection 4.5.5. Finding the incremental version, dU_p/da, of this newly formulated plastic strain energy is easily done by comparing the volume of consecutive DIC strain fields. We can state that in general when measured after $N_i = N + N_{step}$ cycles, the associated crack growth Δa increases plastic strain energy by $[dU_p/da]_{N_i} = U_p(a + \Delta a) - U_p(a)$ based on the definition in Equation 6.9.

6.6.2. On the Discrepancy between the Strain Energy Density and the Effect of Plastic Zone Growth

Plastic zone growth is currently directly and positively related to the crack growth rate da/dN. An increase in plastic zone size in the energy balance will induce an increase in crack growth rate, which is not directly observed in reality. This relates to the use of ΔK_{eff} and the opening stress corrections, which are based on the effect of crack closure due to plasticity. Schijve [8] states that generally a quarter of the plastic zone is involved in a reversed plastic zone, which is sufficiently deformed to close the crack front until a tensile load up to $S = S_{op}$ is achieved in the nominal section.

This closure effect is accounted for in the sliding box analogy in the friction force term. Additionally, the initial base for the crack driving energy term, $U_{\max,0}$, is also corrected for the opening stress, which is important, as it is the starting point definition. However, the energy balance by itself does not contain further corrections, and the use of an opening stress correction when starting with a machined pre-crack is not valid, as shown initially by Elber [21][8]. This was done in this thesis for the EBSB model of the 7075-T6 low-temperature test and could help explain the initial crack growth offset at $\Delta K_{eff} = 3.5$.

The consequence of this effect, and other plastic deformation and damping effects that do not contribute to a crack driving energy, are contained in the energy balance as a part of the golden ratio-based fit (Q). This fitted function scales the mean plastic energy density term dU_p/dV_p and was determined by Kuijk [13]. To get a look at the decreasing trend described by this term, one can look back at Figure 2.3. The decreasing formulation based on Q was defined for experiments with aluminum 2024-T3 at 6.1 mm thickness, which is similar to the specimen tested in this thesis, as well as Fe 510 Nb steel and 7075-T6 at 3.2 mm thickness. The implication is that the specimen thicknesses were similar to the ones in the experiments presented here, but the width was generally higher at 160 mm for the aluminums.

The decreasing trend of Q stands in opposition to the more analytical definition of the plastic strain energy density defined in subsection 4.5.5 and shown by Figure 6.6a. The value for W_p, the plastic strain energy density, increases with strain depending on the yield point and the amount of strain hardening. In the context of low-temperature applications, this makes logical sense, as the greater the deformation and strain hardening the material experiences in the plastic regime, the more energy it captures. This is also in line with the low temperature effects we first defined in section 2.5 [25]. Looking at Figure 6.6b, within the increasing region of dU_p/da ($a = [6.5, 14]$ for low temperature), the energy increase is reminiscent of an exponential trend, which would align it with the dependency on the crack length and accumulating energy based on increasing iso-strain zones observed from DIC.

Overall, the plastic energy density from Kuijk [13] takes into account more than just the plastic strain energy density and is therefore a decreasing trend for a more complex phenomenon. However, the formulation appears to fail to account for the stress ratio and material variations applied to experiments in this thesis. So, to move forward in a methodological manner, a parametric strain energy density, and

therefore a consistent plastic energy term, was defined in Equation 6.9. The author suggests at this point that in order to define the crack closure, crack blunting, and other effects, without influencing the accurate modeling of the plastic energy term, an additional term is necessary. The new term would reformulate the energy dissipation for crack growth by removing the plasticity-related effects that do not drive crack growth as an additional reducing term. An example is presented by Equation 6.10 with a damping term dC_p/da. Calculating this value based on experimental data and developing a parametric relation requires more statistically meaningful data based on multiple trials. This was beyond the reasonable scope of this thesis.

$$\frac{dU}{dN} = \left[2 \cdot \frac{dU_{\mathrm{a}}}{dA}\gamma\lambda T + \frac{dU_p}{dV_p}\frac{dV_p}{da} - \frac{dC_p}{da}\right]\frac{da}{dN} \tag{6.10}$$

Quantifying a function for C_p, which is dependent on the crack length, may be done in the same manner as Kuijk [13] defined the original dU_p/dV_p. The exception is that now the new damping term is independent of the strain energy dissipated in the growth related to the plastic zone.

6.7. A Review of the Sliding Box Analogy

The sliding box analogy as it was introduced by Kuijk [13] is used as a physical analogy to simulate the process of crack propagation for each cycle. This allows a predictive relation between the number of continuous amplitude load cycles and the crack growth. The analogy is based on physics and remains unit consistent, which are both powerful attributes. Through the course of testing, a variety of materials and mechanical properties were input into the EBSB model, and the outcomes were varied. Some materials were modeled very close to experimental results, but most showed quite severe deviation in crack growth rates. What stood out among the data processing is that the direct model, which does not rely on the energy balance and is therefore very dependent on the analogy, was generally robust. We can recall the energy term for the direct method that is used as the forcing function for the sliding box analogy from Equation 2.22, relating the increase in energy dissipation to the change in stiffness due to the Feddersen correction $\beta(a)$.

In all tests at room temperature and at a stress ratio of $R = 0.1$, seen in the appendix Figure E.3 and Figure E.4, the direct method was very close to the measured crack growth data. This is especially true at low values of ΔK_{eff}, where the direct method seemed to hit the center of the data points of initial crack length measurements consistently and matched the slope consistently as well. In the regime approaching final failure, the largest deviations are seen. It can be argued, however, that the entire point of the sliding box analogy is to capture the common Paris regime of consistent crack growth. This regime occurs after crack formation and before the edge effects or large amounts of deformation at final failure take effect. Based on the direct method's very rudimentary approach to the sliding box analogy, evidence is presented that demonstrates its validity in these cases.

At low temperatures, however, there is an observable strong offset between initial crack growth rates of around 0.2 μm, which on the scale of crack growth rates in Figure E.3e is quite substantial. The progression of the curve slope, however, remained very similar to that of the experimental data, indicating primarily a vertical shift due to the initial overestimation of crack growth rate. In contrast to this point, the observation for an increase in the stress ratio caused the opposite effect: minor vertical offset but a greater increase in slope to a greater final deviation.

Overall, based on these comparisons, it can be said that the sliding box itself is likely a valid approach, even if it may not yet be accurate with the current formulation of the energy balance. It is limited by the offset at low temperatures, which is concerning at this point. Reasons for the low temperature offset are not explainable simply by the material properties changing since this did not limit the sliding box performance as demonstrated by the direct approach. This leads to the assumption that the applied load and therefore the value of S_{max} has a greater influence on crack propagation and shielding mechanisms. This assumption was supported by the analysis of the increased plasticity at the crack tip of the low-temperature fatigue test compared to the lower nominally stressed room-temperature test in Figure 6.5. As a result, a possible conclusion is that the energy balance dampening term C_p dealing with the increased plasticity may be used to correct this and improve the accuracy of the EBSB framework.

6.8. Discussion on the Limitations of the Conducted Research

The experimental campaign and the associated modeling framework provide a coherent basis for comparison across alloys and conditions. However, several practical occurrences during testing and key simplifying assumptions in the model introduce limitations that affect the breadth of the dataset and the achievable level of agreement. The following discussion summarizes the most relevant experimental drawbacks and the principal modeling constraints identified from the results.

From an experimental standpoint, the test space was reduced by the absence of a completed 6061-T6 trial at $R = 0.1$. This omission was primarily caused by irregular data capture by the test program and an incorrectly calculated fatigue life leading to an underestimated nominal stress. This resulted in a run that exceeded 900,000 cycles. Beyond limiting direct comparisons across stress ratios for this alloy, this event also highlights the sensitivity of fatigue tests to correct load targeting. Particularly for more ductile materials, where life can increase dramatically when the applied stress is even slightly underestimated while aiming for a target of total cycles to failure.

On the modeling side, a major limitation is the lack of an explicit plane strain transition, which appears to be a contributor to persistent model-data misalignment. The current framework effectively assumes a predominantly plane-stress-like response, whereas the results and fracture observations suggest that constraint effects and transitions in stress state play a meaningful role over the crack propagation regime. An improvement would be to include a thickness-dependent transition between plane strain and plane stress, for example, by assuming a linear stress state transition through the thickness and evaluating the corresponding contributions separately. The observed dependence on applied stress is likely also linked to the stress-state transition attributable to crack growth geometry effects. This suggests that the constraint evolution is not purely thickness-driven but also coupled to the evolving crack-tip field.

A deeper analysis based on the available DIC data can further help explain the remaining discrepancies between the experimental data and the EBSB model predictions. In particular, comparing the current formulation for the energy balance against a robust numerical reference would provide a clearer basis for identifying missing dissipation mechanisms and for quantifying the damping term C_p. A possible numerical reference can be an FEA-based simulation throughout the crack propagation regime.

Finally, the DIC measurements offer a practical way to improve crack growth data quality by enabling compliance-based inference at the crack tip. This approach was already applied using five calibration points for the low-temperature test. Extending this method consistently across all specimens and the full dataset could reduce noise in the crack growth measurements. Implementing a uniform compliance quantification procedure for each specimen would therefore improve the stability of the derived da/dN data and strengthen comparisons between experimental trends and model predictions.

7

Conclusions

This thesis set out to investigate the validity and applicability of a physics-based energy balance approach, specifically the Energy Balance with Sliding Box analogy (EBSB), for modeling fatigue crack growth in aluminum alloys in cold environments. The motivation stemmed from the increasing relevance and value of such models for the design and analysis of cryogenic liquid hydrogen storage solutions and their integration in aerospace structures. For these new design purposes, the traditional empirical approaches like the Paris' law are limited by their dependence on extensive experimental data.

An experimental and data processing methodology was developed to assess the EBSB model's fatigue crack growth framework under both room temperature and low temperature conditions. Quasi-static tensile tests were performed to obtain case-specific elastic and plastic properties, such as the yield stress and strain as well as the elastic stiffness. These properties were then used as the primary material inputs to the EBSB model. Fatigue crack-growth experiments were conducted on ASTM standard-defined specimens using pin-jointed clamping to isolate Mode I loading. Crack length was tracked from images of the specimen's rear face and converted from crack length versus cycles (a-N) relationships to crack growth rates da/dN versus ΔK_{eff} curves using filtered measurements with either curve-fit differentiation or point-wise increments. Deformation fields were tracked at the same intervals as the crack images using a digital image correlation (DIC) speckle pattern and a DIC-specific camera.

Quasi-static tensile testing across the selected aluminum alloys showed the expected ranking in which aluminum 7075-T6 reaches the highest yield and ultimate stresses but shows low hardening. The 2024-T3 alloy occupies an intermediate range in both yield strength and work hardening, the A300 over-aged 2024 specimen showed the lowest yield strength and decreased failure deformation, and 6061-T6 shows a low yield strength with a gradual hardening behavior but large deformation before failure. For 7075-T6 thickness variations (1–6.4 mm), the curves essentially coincide in the elastic region but show some variation at the onset of plasticity with only minor differences at larger strains. At $-30°$C, the 7075-T6 tensile response showed an increase in work hardening of approximately 20 MPa, a similar yield strength differing by approx. 10 MPa, but also an unexpectedly significant decrease in ductility before failure.

Constant-amplitude fatigue experiments produced crack surfaces that were predominantly flat and planar through the initial crack-growth region. The general failure mode was characterized as single-crack growth to final failure on both sides of a centered pre-crack. Most specimens showed the development of single or double shear lips in the last third, or less, of crack growth. Relative surface texture differences, such as increased tortuosity for the 2024 alloys and the low-temperature 7075-T6 case, and a more ductile final fracture impression for 6061-T6, were interpreted as increased crack shielding with higher energy dissipation per crack growth. For the low-temperature fatigue test, the changes expected in the fatigue characteristics at low temperature were not conclusive. While the stress level had to be increased significantly, the number of cycles to failure was also reduced, and the critical stress intensity factor was reached earlier than at room temperature.

From the collected data, the crack growth rate curves were calculated and compared to the EBSB model. To determine the effect of increasing the amount of plastic energy dissipation in the model, the plastic zone approximations from Irwin and Dugdale and the Von Mises yield criterion were compared. The effect did not yield the expected results due to the definition of the plastic energy density by Kuijk [13]. For all but the thickness variations, the increase in plastic zone size led to an increased crack growth rate estimation. This indicated a potential plane strain to plane stress condition through the specimen thickness. Furthermore, DIC strain-field post-processing confirmed that the DIC-derived plastic volume V_p increased with crack length and grew significantly faster at $-30°$C. A decreasing plastic zone was observed at greater crack lengths and attributed to ”holes” appearing in the DIC mesh due to increased crack opening displacement. This observation limited the valid portion of DIC plastic volume plots to the region before $a = 25$ mm at room temperature and $a = 15$ mm at low temperature.

Overall, a range of varied experimental data was created and reviewed. The EBSB model was successfully applied with plastic zone variations for the case-specific quasi-static material properties of each fatigue test. The model was able to capture the fatigue characteristics, as they were present in the low-temperature experiment in this thesis, to a partial extent, being particularly accurate at larger effective stress intensity factors. A lower limit to the validity interval, where the EBSB model can realistically model the fatigue damage growth, appears to lie within the Paris region and the stable tearing region. Material variations at room temperature were not modeled accurately by the full EBSB beyond the small crack lengths. In general, the orders of magnitude and the nature of modeled crack growth curves were similar, however. The direct version of the sliding box analogy, on the other hand, maintained a higher level of robustness independent of the energy balance. Finally, to improve on the assumptions made by the original EBSB framework, a new method was proposed to quantify plastic strain energy density. This allows the separation of energy dissipation related to crack growth from plasticity-induced crack shielding phenomena. Further advances can be obtained by approximating stress state transitions throughout crack growth and as an on thickness.

7.1. Answers to the Research Questions

In this section we expand on the general conclusion by looking at answering the research questions again, now that the results have been collected and discussed. The original hypothesis for each research question was given in section 3.2 and used to construct the methodology. For each research question the agreement with the original hypothesis is stated.

1. To what extent can a physics-based sliding box analogy approach to crack propagation capture the fatigue characteristics of aluminum metals at low temperatures?

The sliding-box analogy effectively captures the overall curvature and order of magnitude of the crack-growth response, particularly when implemented in its direct form. However, the full EBSB model, which incorporates the energy balance, exhibits condition-dependent deviations. These were evident as plasticity and stress-state effects increase, such as for material variations that lower yield stress or increased strain hardening. Across room-temperature tests at $R = 0.1$, the direct sliding-box approach follows measured crack growth trends more closely, especially at lower ΔK_{eff}, supporting the validity of the sliding-box analogy itself. At $-30°$C, the indirect model reproduces a similar slope evolution but exhibits a noticeable initial vertical offset (overestimation), indicating that low-temperature effects are not fully captured in the entire crack growth regime with the current EBSB formulations. Overall,

The extent to which the model captures the fatigue characteristics is indeed limited as hypothesized and was likely related to the energy balance. However, the effect was opposite of what was expected, and crack growth rates were overestimated.

1.(a) How can stress range, material variations, and thickness effects at room temperature lead to conclusions about the validity of Van Kuijk's [13] energy balance with sliding box approach at low temperatures?

Room-temperature variations show that the sliding-box component is comparatively robust, while the energy balance's plastic energy term appears to drive most of the error. Thickness-dependent plane strain conditions likely contribute to early-stage misalignment. Materials with larger ductility and hardening indicate increased crack shielding, which becomes even more critical when extrapolating toward cold environments, where both of these attributes are expected to be enhanced. Thickness effects were observed and could be accounted for, to an extent, by varying the plastic zone size. Increasing the stress ratio showed inconclusive results, in part due to a missing 6061-T6 dataset for $R = 0.1$.

Limitations of the energy balance were shown by changing the variables of this research question, and in its current form it is likely not a valid formulation in contrast to the original hypothesis. This does not mean that the descriptive energy balance can't be valid if the right assumptions are made. For this purpose, points of improvement were determined, and an attempt was made to improve on the plastic energy dissipation term to find a more robust energy balance based on quasi-static properties.

1.(b) What effect does a low-temperature environment have on aluminum in the context of quasi-static mechanical properties for fatigue loading?

At low temperatures, the quasi-static properties were expected to show an increase in yield stress and work hardening to a higher ultimate strength as well as greater ductility. The $-30°$C tensile results indicate approximately a 10 MPa increase in yield stress and increased work hardening to an approximately 13 MPa higher ultimate stress. The measured ductility decreased in this test, which is an outcome flagged as potentially related to the setup or the additional effects of a cold environment.

2. To what extent can the plastic zone size and energy storage of a crack tip in aluminum be defined by using quasi-static mechanical properties at room temperature and $-30°$C?

Plastic zones and energy storage can indeed be defined to a partial extent using quasi-static properties, but the observed plastic zone growth, especially at low temperature, does not map easily to the crack-growth rate. A quasi-static-property-based plastic strain energy density formulation was developed and combined with iso-strain DIC regions to estimate dU_p/da without FEA. The discussion highlights a mismatch where crack growth can be overestimated despite plastic-zone size not being overestimated, pointing to deficiencies in the remaining plastic-energy density term. Plasticity needs to be modeled not only as "more plastic zone leads to more driving energy" but also consistently with shielding and crack closure to be predictive across temperature. A possible split of the plastic energy term into a quasi-static behavior-based strain energy term and a crack length-dependent damping term C_p was proposed.

3. To what extent do the fundamental assumptions made in the physics-based energy balance with sliding box analogy model agree with low-temperature fatigue?

As hypothesized, the agreement is limited. Key assumptions, such as a plane stress state and the way plasticity is translated into driving energy, are plausible in trend but insufficient. This was shown for the tested material variations as well as the low-temperature test. Maintaining a plane-stress assumption throughout likely inflates early crack-growth predictions when constraint is strongest, suggesting the need for a plane stress/plane strain transition treatment. Using opening-stress corrections at the start from a machined pre-crack is identified as invalid and may contribute to the low-temperature initial offset when the model is initialized before a crack has fully formed. The assumption that the plasticity effect can be collapsed into the dU_p/dV_p term, using the golden ratio-based curve fit Q, was another fundamental assumption that did not hold up to the testing that was performed within the scope and testing methodologies of this thesis.

8

Recommendations for Future Research

This chapter identifies key points of improvement and recommendations for further research to extend the scope and usefulness of the present work. It first highlights the need for expanded cryogenic testing to achieve lower temperatures, increase repeatability, and improve confidence in the observed material trends under more representative low and cryogenic environmental conditions. Next, it is recommended to incorporate strain hardening into the constitutive analytical framework to better capture post-yield behavior, allowing the improvement of energy density calculations. The chapter further emphasizes improving the spatial resolution and processing of DIC imaging measurements to refine estimates of plastic zone size, particularly in regimes where the crack is initiating or the crack is very open. Finally, a critical reassessment of the plastic energy density estimation is recommended based on the improved property-based energy density estimation.

8.1. Cryogenic Testing

The low-temperature campaign was constrained by the climate-chamber cooling performance. Issues with the liquid-nitrogen feed meant the minimum temperature only hovered around -30°C rather than the initial target of -50°C. In addition, clamp misalignment introduced out-of-plane wobble; this can be corrected and may improve load introduction. The double pin-joint used to extend into the chamber showed similar wobble, but the pins likely limited any load-introduction effects. A more critical limitation was frictional heating in the pins, which generated substantial heat (visible as smoke) and effectively capped the run at about 140,000 cycles as chamber temperature began to rise. This issue should be reduced at a higher stress ratio, and with an improved liquid-nitrogen feed, it should be less noticeable due to better cooling.

Material and setup choices also suggest clear next steps. The low-temperature test used 7075-T6 as the baseline material, but a 6xxx or 2xxx series alloy may be more representative for pressure-tank applications, where changes in work hardening and ductility can be more pronounced. At the same time, 7075-T6 remains close to elastic perfectly plastic behavior and therefore aligns well with the model's base assumptions. For further investigation, scaling down the specimen size would simplify cryogenic testing and make voltage-drop crack measurement particularly valuable. Finally, because the chamber provides only a single viewing window, observations were limited to one side; a two-camera arrangement could capture both crack growth and DIC on the two window-facing halves of the specimen.

8.2. Accounting for Strain Hardening

The results of this study indicate that further refinement of the crack growth framework should focus on improved treatment of elastic–plastic behavior at the crack tip, with particular emphasis on accounting for the strain hardening effects. The displacement field analysis from DIC led to the estimation of the plastic volume created with the crack advance calculated based on subsection 4.5.5. As shown in the plot of plastic volume growth rate in Figure 6.5, the experimentally observed plastic volume growth per unit crack advance exceeds the values predicted by the EBSB model, while the corresponding crack growth was overestimated for materials other than 7075-T6 aluminum. This inconsistency suggests that the way plastic energy dissipation was related to the crack driving energy dissipation was not correct without the average plastic energy density function derived for the datasets used by Kuijk [13]. Therefore, a new way of incorporating a stress-strain curve parametrically was devised in Equation 6.9. Building on this relation will allow calculating the plastic strain energy density, including strain hardening contributions. This would improve the use of quasi-static properties to estimate the plastic energy dissipation. A primary difference of the outlined approach would be the ability to capture strain hardening to the ultimate stress rather than assuming constant stress and strain beyond the yield point.

A further expansion with respect to strain hardening, ductility, and the stress-strain curve would be to employ true stress and strain measurements during quasi-static tensile tests. The difference between engineering and true stress-strain curves is the implementation of the Poisson ratio and accounting for a changing cross-section of the specimen under load. The effect is a greater amount of measured strain hardening as the applied load increases, but as the cross section shrinks, the true stress is higher. The benefit of using a true stress-strain relationship is that curve functions like Ramberg-Osgood [48] and its variations are better suited to modeling true stress-strain at higher strain values. The necessary data for calculating true stresses and strain can also be extracted from existent DIC images of the tensile tests in this thesis by applying virtual strain gauges across the loading direction. 3D DIC would further improve the measurements with out-of-plane displacement data.

8.3. Plastic Energy Density Estimation

In subsection 6.6.1, a function was proposed that makes use of the Ramberg-Osgood relation to represent the plastic strain energy density relationship in the plastic zone. The function was given in Equation 6.9. Future work should incorporate this quasi-static property-based approach to estimate the plastic strain energy density of a crack tip's stress field. An implementation into the EBSB model may improve the approach to replace the current golden ratio-based curve (Q) for the scaling of the plastic strain energy density as well as separate crack shielding from crack-driving mechanisms.

As shown in Figure 6.6, the decreasing trend employed by Kuijk [13] for the plastic energy density was not recreated with the plastic strain energy formulation. In all tests an increase in dVp/da resulted in an increase in crack growth. As a consequence, the investigation of a damping term, C_p, in the energy balance that accounts for the crack shielding related to the size of the plastic zone and the energy captured within it is strongly recommended.

The DIC measurements obtained in this study provide a step toward reconstructing the full-field strain state within a finite element analysis (FEA) by imposing the experimentally measured surface deformations onto an FEA mesh. Such an approach would allow the strain field to be extended beyond the surface and enable evaluation of local energy dissipation terms associated with plastic deformation, including variations through the specimen thickness. The usage of the J-integral to evaluate energy dissipation is an additional advantage of a finite element approach. Comparable methodologies have been demonstrated in the literature, where DIC-informed finite element analyses have been used for comparison with experimental energy dissipation data, as outlined by Quan [16].

The measurement of the cyclic stress-strain relationship throughout fatigue damage propagation and related hysteresis progression is another useful step for deeper analysis of the energy balance. The measured energy dissipation can be used to evaluate both the EBSB model as well as analytical and finite element-based energy dissipation calculations. Additionally, FEA material data can be obtained from the quasi-static stress-strain curves when represented by the Ramberg-Osgood relation.

8.3.1. Resolution and Analysis of the Plastic Zone

The resolution and analysis of the plastic zone was limited in the presented research by the camera setup as well as the effect of holes in the DIC displacement fields. For future research a higher resolution camera, or a focus on only half of the center-cracked specimen for DIC, could significantly improve the level of noise with which the speckle pattern is captured. Half-specimen DIC is also useful for climate chamber tests where the crack length must be measured. Crack growth pictures could then be taken of the other side of the center crack from the same side through the viewing window.

Concerning the holes created by non-converging cells in the DIC displacement fields, a method to account for this in data processing should exist. It should be possible to use logic-based metrics to determine pixel strain values depending on the previous image. By converting values of strain that are exactly zero after previously being in the plastic strain magnitude regime to ”NaN” values, it would be possible to filter these pixels out or ignore their decrease in magnitude.

8.4. Plane Stress and Plane Strain

In addition to the plastic zone size model, another extension of the present work would be to incorporate explicit thickness-based corrections for the stress state within the specimen. This could be achieved by partitioning the specimen thickness into regions governed predominantly by plane strain and plane stress conditions, respectively, and evaluating the associated energy dissipation in each region in separate steps. Such an approach would better reflect the three-dimensional nature of the crack-tip stress state.

Furthermore, the transition from plane strain to stress also exists macroscopically in the direction of crack growth. Starting out as plane strain dominated and progressing to a plane stress condition as stress intensity increases and the remaining net section diminishes. An initial approximation for this phenomenon could be to split the energy balance based on observable transitions from plane strain to plane stress. As mentioned, that could be the transition into shear lip behavior at values such as $2a/W = 2/3$ or $1/2$. Alternatively, it may also be possible to use 3D DIC, with a stereo camera setup, to measure the out-of-plane strain ϵ_z. The current plane strain formulation to determine a strain magnitude in DIC is a conservative approach. It can benefit from either a through-thickness correction with measured out-of-plane strain values or using the Poisson ratio effect instead.

8.5. Additional Recommendations

Thus far the more complex and fundamental recommendations have been explained in detail up to this point, but there are further recommendations to take into account when conducting further research into the topics covered in this thesis. These additional recommendations are listed below for reference.

- Run repeated fatigue tests per condition, such as five or more, to quantify scatter and improve confidence in observed trends. This helps increase the statistical relevance of the results.
- Use a more directly comparable constant nominal stress for all specimen. This would aid in isolating individual properties and their specific effect within the EBSB model and the fatigue properties of the specimen.
- Reduce operator-induced noise by moving toward more automated crack-length tracking (e.g., potential drop, or higher-quality imaging with automated tracking).
- Avoid overreliance on smoothing. Exponential fits of a-N curves before differentiating can mask or distort local changes in crack growth rate; in some cases it was found the point-wise data aligns better with the model.
- Revisit the use of opening-stress corrections and when they are applied, since this may have contributed to initial model curve offsets. They could also be used to quantify plasticity related crack closure parametrically to relate back to the plastic energy dissipation.
- Extend the EBSB framework’s limitations regarding overload corrections or variable-amplitude loading effects.

References

[1] "Innovative cryogenic electric flight (ICEFlight)," Luchtvaart in Transitie. [Online]. Available: https://luchtvaartintransitie.nl/en/project-item/iceflight/.

[2] M. Nagelsmit and L. Veldhuis, "Towards a sustainable air transport system," Delft Univ. of Technology and Nederlands Lucht- en Ruimtevaartcentrum, Whitepaper TU Delft - NLR, Feb. 2021, pp. 27–47.

[3] M. F. Hordeski, *Alternative fuels: the future of hydrogen*, 3rd ed. Boca Raton, United States: CRC press, 2013.

[4] M. Jin et al., "Cryogenic deformation behaviour of aluminium alloy 6061-t6," *Metals and Materials International*, vol. 30, no. 6, pp. 1492–1504, Jun. 2024. DOI: 10.1007/s12540-023-01594-5.

[5] Y. Oda, H. Noguchi, and K. Higashida, "Loading frequency effect on fatigue crack growth rate in low pressure hydrogen gas in the case of a6061-t6 aluminum alloy," *Journal of Solid Mechanics and Materials Engineering*, vol. 5, no. 11, pp. 599–609, Nov. 2011. DOI: 10.1299/jmmp.5.599.

[6] C. H. Wang, "Plastic yielding at crack tip," in *Introduction to Fracture Mechanics*. Melbourne, Australia: DSTO Aeronautical and Maritime Research Laboratory, 1996, pp. 36–44. DOI: 10.13140/RG.2.1.1444.2408.

[7] D. Broek, *Elementary Engineering Fracture Mechanics*, 3rd ed. Dordrecht: Springer Netherlands, 1982.

[8] J. Schijve, *Fatigue of Structures and Materials*. Dordrecht, Netherlands: Springer Science & Business Media, 2009.

[9] A. Kotousov, A. Khanna, and S. Bun, "An analysis of elasto-plastic fracture criteria," in *Recent Advances in Structural Integrity Analysis - Proceedings of the International Congress (APCF/SIF-2014)*, L. Ye, Ed. Woodhead Publishing, 2014, pp. 67–71. DOI: 10.1533/9780081002254.67.

[10] T. Machniewicz, "Fatigue crack growth prediction models for metallic materials: Part i: Overview of prediction concepts," *Fatigue & Fracture of Engineering Materials & Structures*, vol. 36, pp. 293–307, Apr. 2013. DOI: 10.1111/j.1460-2695.2012.01721.x.

[11] L. Bian and F. Taheri, "Analytical modeling of fatigue crack propagation in metals coupled with elasto-plastic deformation," *International Journal of Fracture*, vol. 153, no. 2, pp. 161–168, Oct. 2009. DOI: 10.1007/s10704-008-9301-8.

[12] R. Alderliesten, "How proper similitude can improve our understanding of crack closure and plasticity in fatigue," *International Journal of Fatigue*, vol. 82, pp. 263–273, Jan. 2016. DOI: 10.1016/j.ijfatigue.2015.04.011.

[13] J. van Kuijk, "Novel insights into the physics of fatigue crack growth: Theoretical and experimental research on the fundamentals of crack growth in isotropic materials," Doctoral Thesis, Dept. of Aerospace Engineering, Delft Univ. of Technology, Delft, Netherlands, 2022. DOI: 10.4233/UUID:A7676DC2-8003-4495-839D-B900F95FD061.

[14] L. Vitos et al., "The surface energy of metals," *Surface Science*, vol. 411, no. 1, pp. 186–202, Aug. 1998. DOI: 10.1016/S0039-6028(98)00363-X.

[15] J. Hogeveen, "Towards a proper understanding of fatigue crack growth and crack closure," Master Thesis, Dept. of Aerospace Engineering, Delft Univ. of Technology, Delft, Netherlands, 2016. [Online]. Available: https://resolver.tudelft.nl/uuid:fbad28b7-f53d-44eb-b1cd-ac16a107b226.

[16] H. Quan, "The energy dissipation during fatigue crack growth," Doctoral Thesis, Dept. of Aerospace Engineering, Delft Univ. of Technology, Delft, Netherlands, 2022. DOI: 10.4233/UUID:5C4D7F24-4DF6-40B2-B58F-8F673F17AE4C.

[17] R. C. Alderliesten, “The explanation of stress ratio effect and crack opening corrections for fatigue crack growth in metallic materials,” *Advanced Materials Research*, vol. 891-892, pp. 289–294, Mar. 2014. DOI: 10.4028/www.scientific.net/AMR.891-892.289.

[18] J. J. Van Kuijk, R. C. Alderliesten, and R. Benedictus, “Unraveling the myth of closure corrections: Sharpening the definition of opening and closure stresses with an energy approach,” *International Journal of Fatigue*, vol. 143, no. 106016, Feb. 2021. DOI: 10.1016/j.ijfatigue.2020.106016.

[19] A. U. De Koning, “A simple crack closure model for prediction of fatigue crack growth rates under variable-amplitude loading,” in *Fracture Mechanics*, R. Roberts, Ed. West Conshohocken, United States: ASTM International, 1981, pp. 63–85. DOI: https://doi.org/10.1520/STP28791S.

[20] J. Schijve, “Some formulas for the crack opening stress level,” *Engineering Fracture Mechanics*, vol. 14, no. 3, pp. 461–465, Jan. 1981. DOI: 10.1016/0013-7944(81)90034-5.

[21] W. Elber, “The significance of fatigue crack closure,” in *Damage Tolerance in Aircraft Structures*, M. Rosenfeld, Ed. West Conshohocken, Untied States: ASTM International, 1971, pp. 230–242. DOI: 10.1520/STP26680S.

[22] G. B. Stephenson, “Evaluation of the strain energy density method of notch stress concentration calculations in the plastic range,” Master Thesis, Dep. of Aeronautics and Astronautics, Naval Postgraduate School, Monterey, United States, 1996. [Online]. Available: https://apps.dtic.mil/sti/tr/pdf/ADA311044.pdf.

[23] G. Irwin, “Linear fracture mechanics, fracture transition, and fracture control,” *Engineering Fracture Mechanics*, vol. 1, no. 2, pp. 241–257, Aug. 1968. DOI: 10.1016/0013-7944(68)90001-5.

[24] C. Sun and Z.-H. Jin, “Crack tip plasticity,” in *Fracture Mechanics*, A. T. Zehnder, Ed. Springer, 2012, pp. 123–169. DOI: 10.1016/B978-0-12-385001-0.00006-7.

[25] P. Duthil, “Superconductivity for accelerators,” in *in Proceedings of the CAS–CERN Accelerator School*, R. Bailey, Ed. Geneva, Switzerland: CERN, 2014, vol. 27, pp. 77–96. DOI: 10.5170/CERN-2014-005.

[26] S. W. Van Sciver, “Low-temperature materials properties,” in *Helium Cryogenics*. New York, United States: Springer New York, 2012, pp. 17–58. DOI: 10.1007/978-1-4419-9979-5_2.

[27] “Alloys information & technical data sheets,” ASM Aerospace Specification Metals, Accessed: Nov. 28, 2025. [Online]. Available: https://www.aerospacemetals.com/aluminum-distributor/.

[28] A. Tzamtzis and A. T. Kermanidis, “Improvement of fatigue crack growth resistance by controlled overaging in 2024□t3 aluminium alloy,” *Fatigue & Fracture of Engineering Materials & Structures*, vol. 37, no. 7, pp. 751–763, Jul. 2014. DOI: 10.1111/ffe.12163.

[29] C. H. Suh, Y.-C. Jung, and Y. S. Kim, “Effects of thickness and surface roughness on mechanical properties of aluminum sheets,” *Journal of Mechanical Science and Technology*, vol. 24, no. 10, pp. 2091–2098, Oct. 2010. DOI: 10.1007/s12206-010-0707-7.

[30] B. Nečemer et al., “High-cycle fatigue behaviour of the aluminium alloy 5083-h111,” *Materials*, vol. 16, no. 7, p. 2674, Mar. 2023. DOI: 10.3390/ma16072674.

[31] *Test methods for tension testing of metallic materials*, E8/E8M-22, ASTM International, 2024. DOI: 10.1520/E0008_E0008M-22.

[32] *Test method for measurement of fatigue crack growth rates*, E647-24, ASTM International, 2024. DOI: 10.1520/E0647-24.

[33] A. d. S. Ribeiro, A. M. P. d. Jesus, and A. A. Fernandes, “Fatigue crack propagation rates of the aluminum alloy 6061-t651,” in *18th International Congress of Mechanical Engineering*. Ouro Preto, Brazil: ABCM, Nov. 2005.

[34] M. A. Sutton, J.-J. Orteu, and H. W. Schreier, *Image correlation for shape, motion and deformation measurements: basic concepts, theory and applications*. New York, N.Y: Springer, 2009.

[35] “Digital image correlation: Motion and deformation analysis,” Accessed: Nov. 28, 2025. [Online]. Available: https://www.zeiss.com/metrology/en/explore/topics/digital-image-correlation.html.

[36] N. Lovaas. “Resolution and accuracy. ”[Online]. Available: https://correlated.kayako.com/article/32-resolution-and-accuracy.

[37] “Filtering and smoothing data,” Accessed: Nov. 28, 2025. [Online]. Available: https://nl.mathworks.com/help/curvefit/smoothing-data.html.

[38] H. J. K. Lemmen, “Fatigue and damage tolerance of friction stir welded joints for aerospace applications,” Doctoral Thesis, Dept. of Aerospace Engineering, Delft Univ. of Technology, Delft, Netherlands, 2010.

[39] T. Pardoen et al., “Mode i fracture of sheet metal,” *Journal of the Mechanics and Physics of Solids*, vol. 52, no. 2, pp. 423–452, Feb. 2004. DOI: 10.1016/S0022-5096(03)00087-5.

[40] E. Zaiken and R. Ritchie, “Effects of microstructure on fatigue crack propagation and crack closure behavior in aluminum alloy 7150,” *Materials Science and Engineering*, vol. 70, pp. 151–160, Apr. 1985. DOI: 10.1016/0025-5416(85)90276-9.

[41] M. Schaefer and R. A. Fournelle, “Effect of strontium modification on near- threshold fatigue crack growth in an al-si-cu die cast alloy,” *Metallurgical and Materials Transactions A*, vol. 27, no. 5, pp. 1293–1302, May 1996. DOI: 10.1007/BF02649866.

[42] J. Zuidema, F. Veer, and C. Van Kranenburg, “Shear lips on fatigue fracture surfaces of aluminum alloys,” *Fatigue & Fracture of Engineering Materials & Structures*, vol. 28, no. 1, pp. 159–167, Jan. 2005. DOI: 10.1111/j.1460-2695.2004.00837.x.

[43] R. Alderliesten, “How proper similitude principles could have improved our understanding about fatigue damage growth,” in *24th ICAF Conference and 28th ICAF Symposium*, A. Siljander, Ed. Helsinki, Finland: ICAF, 2015, pp. 47–57. [Online]. Available: https://repository.tudelft.nl/record/uuid:fe8d2b88-f6b0-4844-8b89-d97904a660e8.

[44] T. O. Hodson, “Root-mean-square error (RMSE) or mean absolute error (MAE): When to use them or not,” *Geoscientific Model Development*, vol. 15, no. 14, pp. 5481–5487, Jul. 2022. DOI: 10.5194/gmd-15-5481-2022.

[45] M. Janssen, J. Zuidema, and R. Wanhill, *Fracture Mechanics: Fundamentals and Applications*, 2nd ed. CRC Press, 2004. DOI: 10.1201/9781482265583. [Online]. Available: https://www.taylorfrancis.com/books/9781482265583.

[46] H. Ye et al., “Calibration of paris law constants for crack propagation analysis of damaged steel plates strengthened with prestressed CFRP,” *Theoretical and Applied Fracture Mechanics*, vol. 117, no. 103208, Feb. 2022. DOI: 10.1016/j.tafmec.2021.103208.

[47] Y. Wang et al., “Deformation behavior of pure aluminum at room and cryogenic temperatures,” *Journal of Materials Research and Technology*, vol. 31, pp. 2355–2366, Jul. 2024. DOI: 10.1016/j.jmrt.2024.06.215.

[48] W. Ramberg and W. R. Osgood, “Description of stress-strain curves by three parameters,” National Bureau of Standards, NACA-TN-902, Jul. 1943. [Online]. Available: https://ntrs.nasa.gov/citations/19930081614.

A

Engineering Drawings

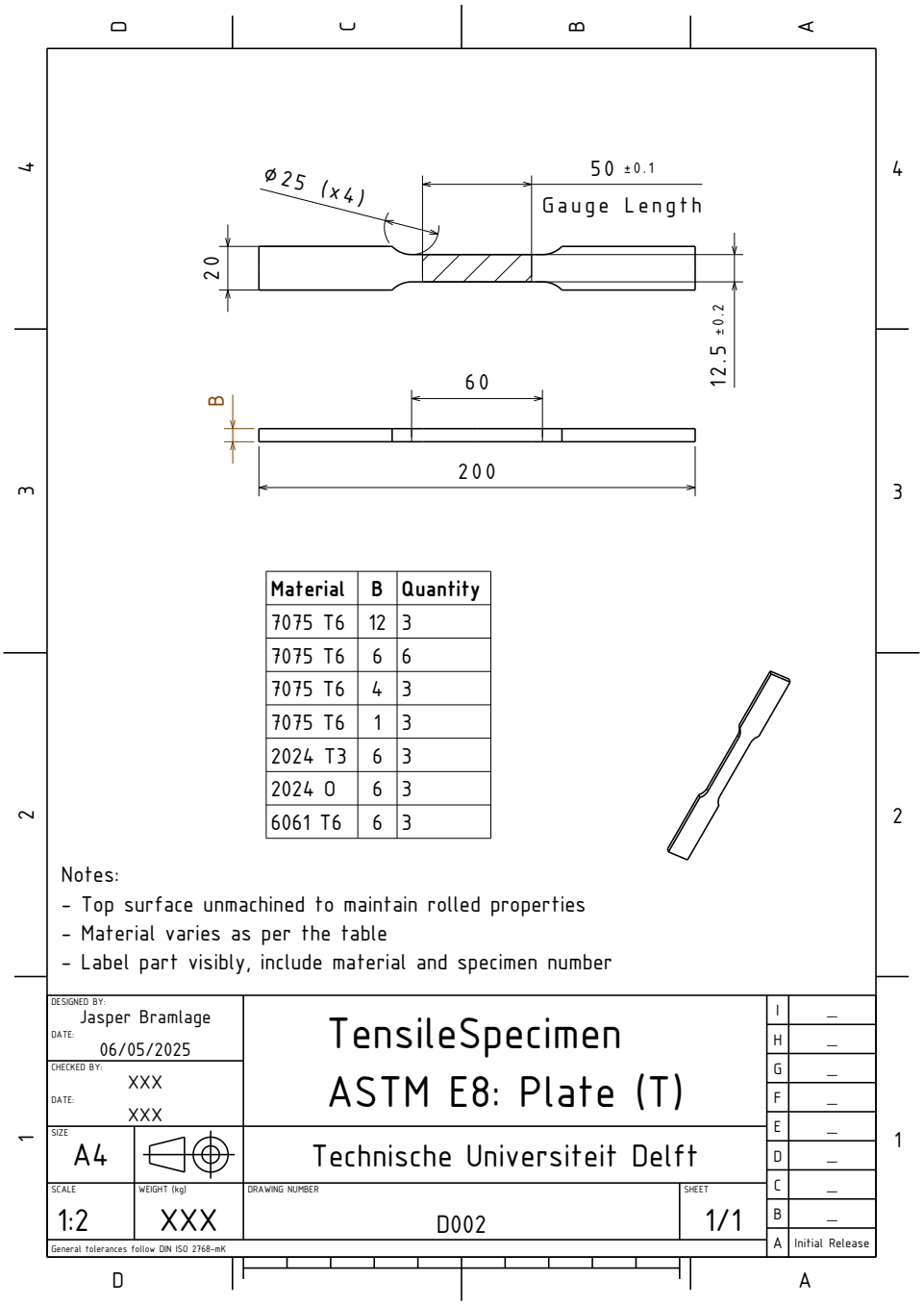

Figure A.1: Tensile quasi-static testing specimen. Note: ”2024 O” was replaced with ”2024 A300”.

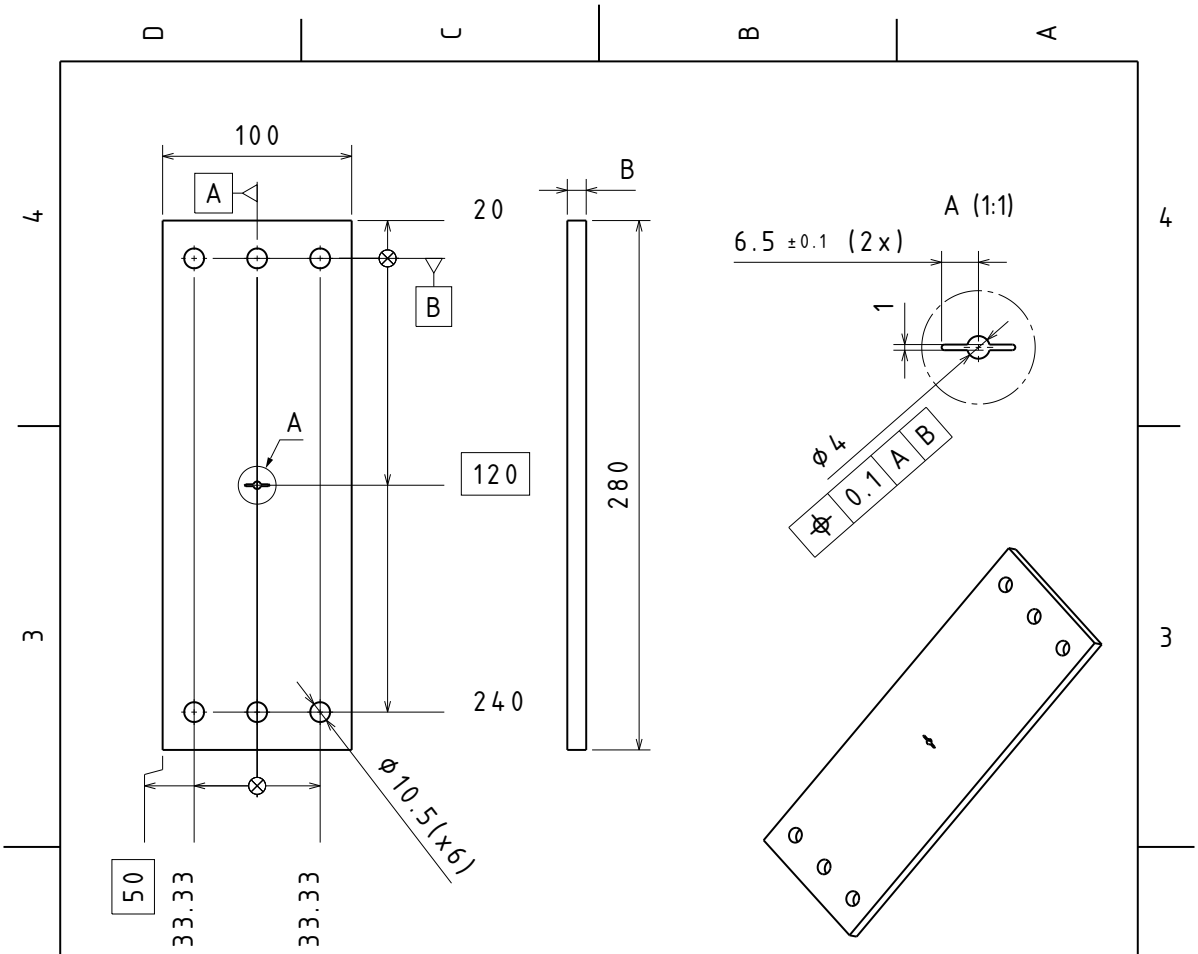

Notes:

- Boxed dimensions to be ±0.01 mm
- Material varies, follow separately discussed instructions
- Label part visibly, include thickness (B) and specimen number
- 1mm slot to be milled if possible

	7075 T6	*6061 T6*	*2024 T3*	*2024 O*
B	**Quantity**			
1	1	0	0	0
4	1	0	0	0
6	5	2	2	1
12	1	0	0	0

DESIGNED BY: Jasper Bramlage DATE: 29/04/2025	FatigueSpecimen ASTM E647-24: M(t)		
CHECKED BY: XXX DATE: XXX			
SIZE: A4	Technische Universiteit Delft		
SCALE: 1:3	WEIGHT (kg): XXX	DRAWING NUMBER: D001	SHEET: 1/1
General tolerances follow DIN ISO 2768-mK			

I	–
H	–
G	–
F	–
E	–
D	–
C	–
B	–
A	Initial Release

Figure A.2: Fatigue testing specimen. Note: ”2024 O” was replaced with ”2024 A300” and the 1 mm wide slot was created with wire EDM instead of milling.

B

Test Matrices with Notes

Table B.1: Summary of quasi-static tensile experimental test matrix and specific observations.

#	Material	Thickness [mm]	Temperature [°C]	Speed [mm/min]	Notes
1	7075-T6	1.00	21.0	0.9	-
2	7075-T6	1.00	21.0	0.9	-
3	7075-T6	1.00	21.0	0.9	-
1	7075-T6	4.00	21.0	0.9	-
2	7075-T6	4.00	21.0	0.9	REMOVED: Indexing error DIC to load data
3	7075-T6	4.00	21.0	0.9	-
1	7075-T6	6.43	21.0	0.9	-
2	7075-T6	6.43	21.0	0.9	REMOVED: negative strain measurements from DIC were not directly invertible.
3	7075-T6	6.43	21.0	0.9	-
1	7075-T6	6.43	-30.0	1.0	Crosshead speed increased to 4 mm/min after yield.
2	7075-T6	6.43	-30.0	1.0	REMOVED: interrupted at IMG 2506 and then continued, resulting in out-of-sync measurements.
3	7075-T6	6.43	-30.0	1.0	Crosshead speed increased to 4 mm/min after yield, failed earlier than expected.
1	6061-T6	6.50	21.0	0.9	-
2	6061-T6	6.49	21.0	0.9	Strain offset aligned for use with average curve.
3	6061-T6	6.49	21.0	0.9	-
1	2024-T3	6.36	21.0	0.9	Crosshead speed increased to 2 mm/min after 2% strain which is after the yield point for all materials.
2	2024-T3	6.36	21.0	0.9	Speed increased to 2 mm/min after yield.
3	2024-T3	6.36	21.0	0.9	Speed increased to 2 mm/min after yield.
1	2024-T3-TL	6.36	21.0	0.9	Strain offset aligned for use with average curve. Speed increased to 2 mm/min after yield.
2	2024-T3-TL	6.36	21.0	0.9	Speed increased to 2 mm/min after yield.
3	2024-T3-TL	6.36	21.0	0.9	Speed increased to 2 mm/min after yield.
1	2024-A300-TL	6.36	21.0	0.9	Speed increased to 2 mm/min after yield.
2	2024-A300-TL	6.36	21.0	0.9	Speed increased to 2 mm/min after yield.
3	2024-A300-TL	6.36	21.0	0.9	Speed increased to 2 mm/min after yield.

Table B.2: Fatigue test matrix with cycles to failure and specimen specific observations.

#	Material	Thickness [mm]	Stress Ratio [-]	Temperature [$\pm 3\,^{\circ}$C]	Cycles to Failure [-]	Notes
1	7075-T6	1.00	0.1	21.0	–	REMOVED: Failed to fail after 550,000 cycles after a single overload during setup peaking around the 8 kN mark ($2\times$ cyclic).
2	7075-T6	1.00	0.1	21.0	127,084	Everything worked well, failed slightly early due to slightly higher load to encourage crack initiation.
1	7075-T6	4.00	0.1	21.0	185,024	Everything worked well.
2	7075-T6	4.00	0.1	-30.0	–	REMOVED: Blue double pin clamps. Climate chamber control set to -50°C and held for 30 min before starting test. Start temperature: -26.3°C. Minimum temperature reached: -33°C. Heating after 140,000 cycles due to friction and heat dissipation overcoming cooling capacity without liquid nitrogen. Stopped at 261,881. The climate chamber wobbles to an extent; this appears to cause distortion in the window, affecting the speckle pattern for DIC.
1	7075-T6	6.43	0.1	21.0	185,142	Failed to record a correct DIC reference image; bad crack tracking on rear camera due to lacking contrast and exposure.
2	7075-T6	6.43	0.1	21.0	193,289	Everything worked well. Applied white paint on rear face to account for lighting to measure crack length.
3	7075-T6	6.43	0.5	21.0	193,422	No out-of-plane wobble observed anymore, likely due to the higher average stress being higher than the aligning force for the setup.
4	7075-T6	6.43	0.1	-30.0	115,460	Everything worked well, temperature within -30°C $\pm 3^{\circ}$C. Some out-of-plane wobble of the climate chamber, potentially distorting DIC images.
1	6061-T6	6.50	0.1	21.0	951,843	Ran too long due to high fatigue resistance; some misalignment in the 250 kN Zwick causes out-of-plane wobble. Measured every 500 cycles. Issues with images; some cycles did not load correctly.
2	6061-T6	6.50	0.5	21.0	197,058	No problems in test setup but missing DIC images are evidenced again in this test as well.
1	2024-T3 T-L	6.36	0.1	21.0	191,981	T–L orientation. Missing some DIC images as with all tests on the 250 kN Zwick, as it turns out.
1	2024-A300 T-L	6.36	0.1	21.0	43,212	Capped at 52 kN, 8 Hz for vibrations. One extra picture in DIC data due to zero $\neq$ zero after 52 kN load and will be used to review DIC effects later. Failed very quickly; properties likely than given in the reference source.

C

Quasi-Static Tensile Stress-Strain Curves

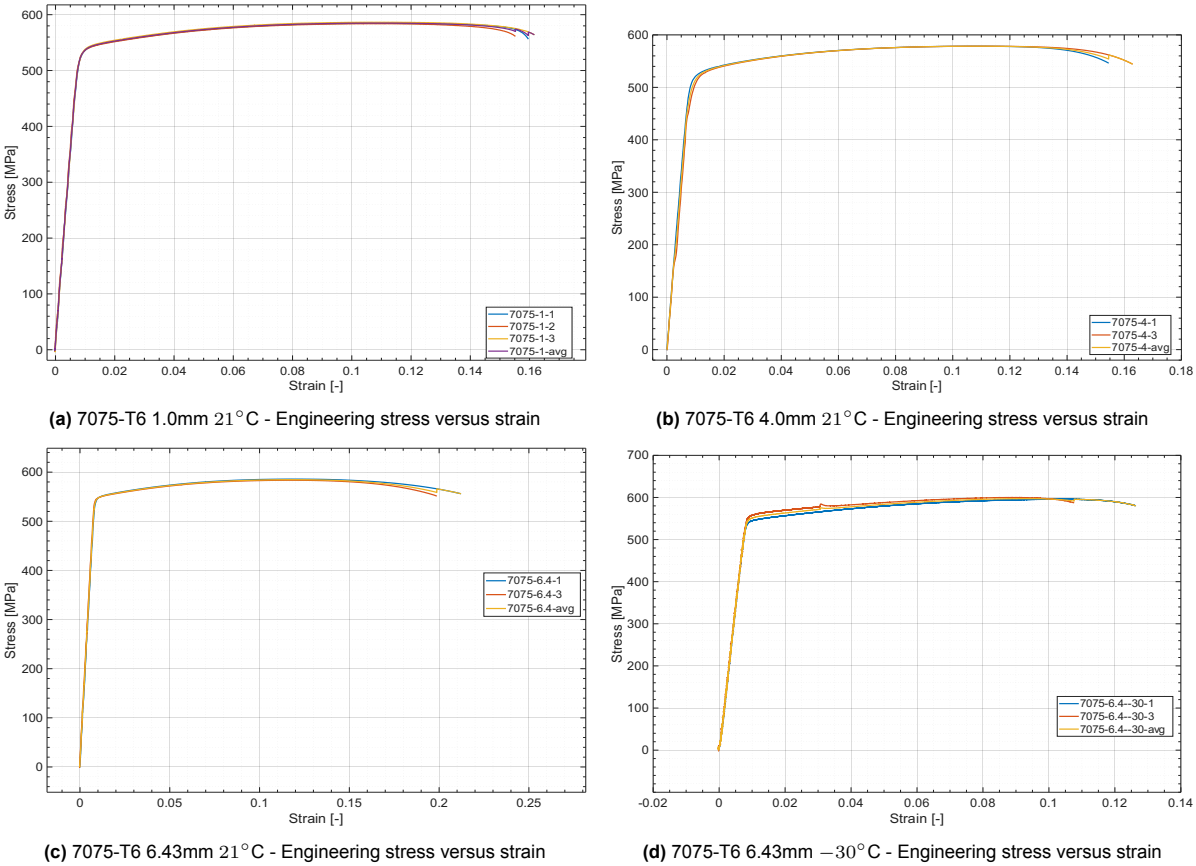

(a) 7075-T6 1.0mm 21°C - Engineering stress versus strain

(b) 7075-T6 4.0mm 21°C - Engineering stress versus strain

(c) 7075-T6 6.43mm 21°C - Engineering stress versus strain

(d) 7075-T6 6.43mm -30°C - Engineering stress versus strain

Figure C.1: Quasi-static tensile testing results. Shown as engineering stress versus strain curves with outlier trials removed. Page 1.

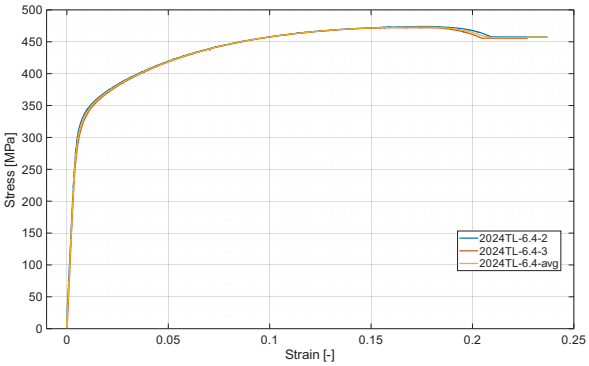

(a) 2024-T3 (T-L) 6.36mm 21°C - Engineering stress versus strain

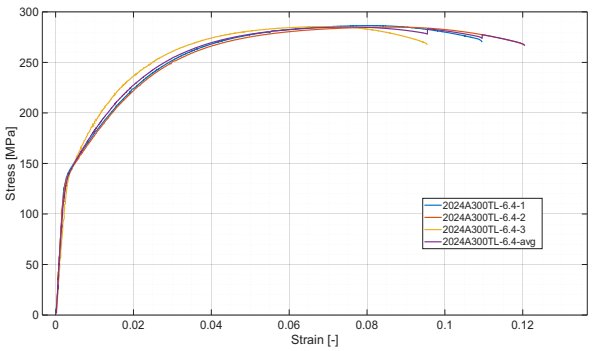

(b) 2024-A300 (T-L) 6.36mm 21°C - Engineering stress versus strain

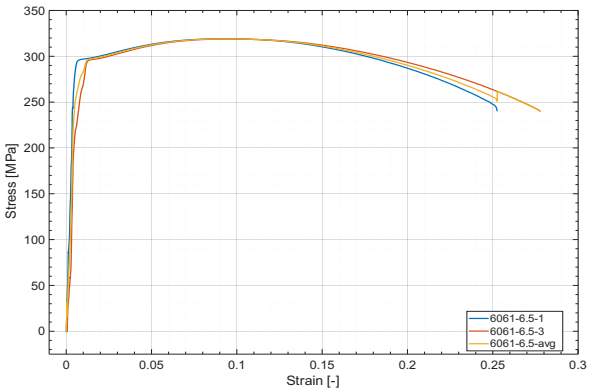

(c) 6061-T6 6.50mm 21°C - Engineering stress versus strain

Figure C.2: Quasi-static tensile testing results. Shown as engineering stress versus strain curves with outlier trials removed. Page 2.

D

Fatigue Crack Growth Results

D.1. Experimental Crack Growth Data

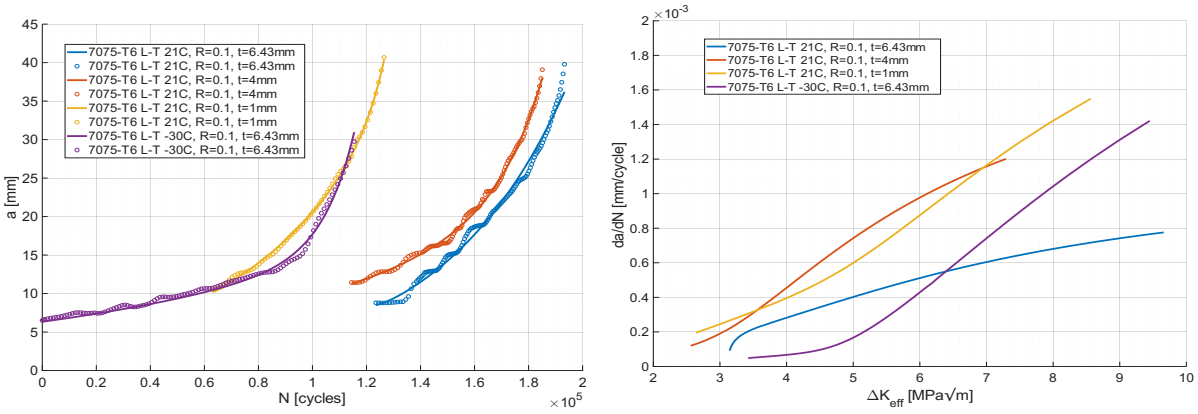

(a) Crack length versus cycles

(b) da/dN versus ΔK_{eff}

Figure D.1: Fatigue testing results for thickness variations for 7075-T6 at $21°$C and $-30°$C

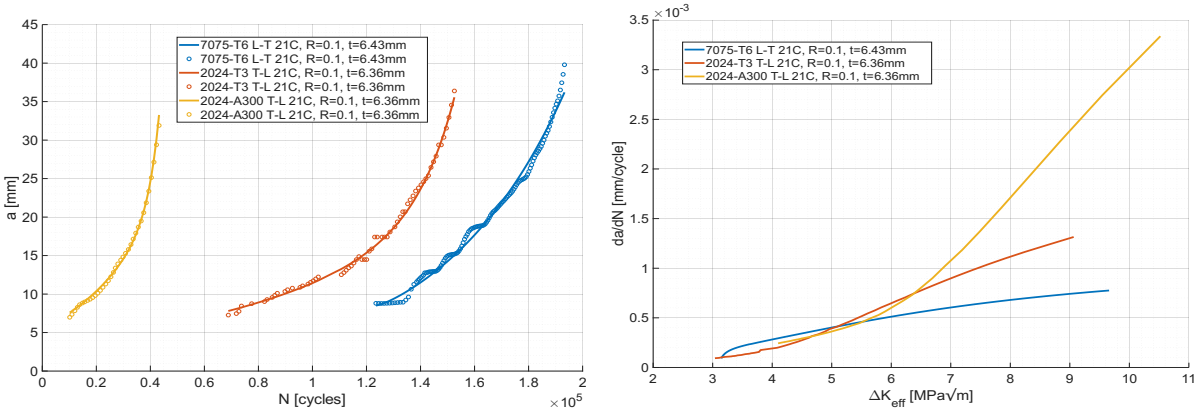

(a) Crack length versus cycles

(b) da/dN versus ΔK_{eff}

Figure D.2: Fatigue testing results for material variations.

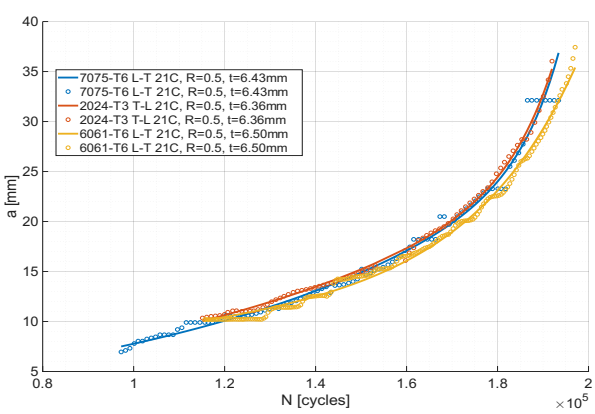

(a) Crack length versus cycles for $R = 0.5$

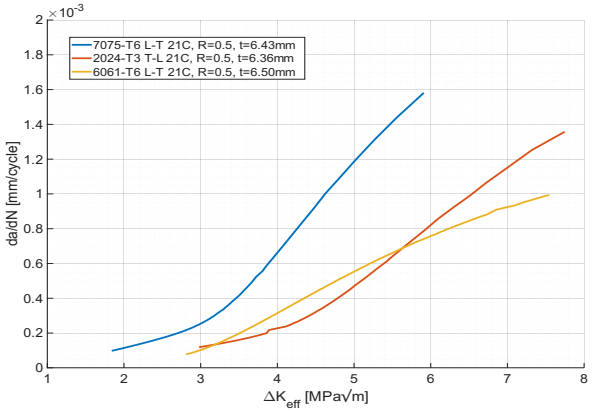

(b) da/dN versus ΔK_{eff} for $R = 0.5$

Figure D.3: Fatigue testing results for the R-ratio variation.

E

Crack Length Versus Cycles Irwin (Original) EBSB Model Results

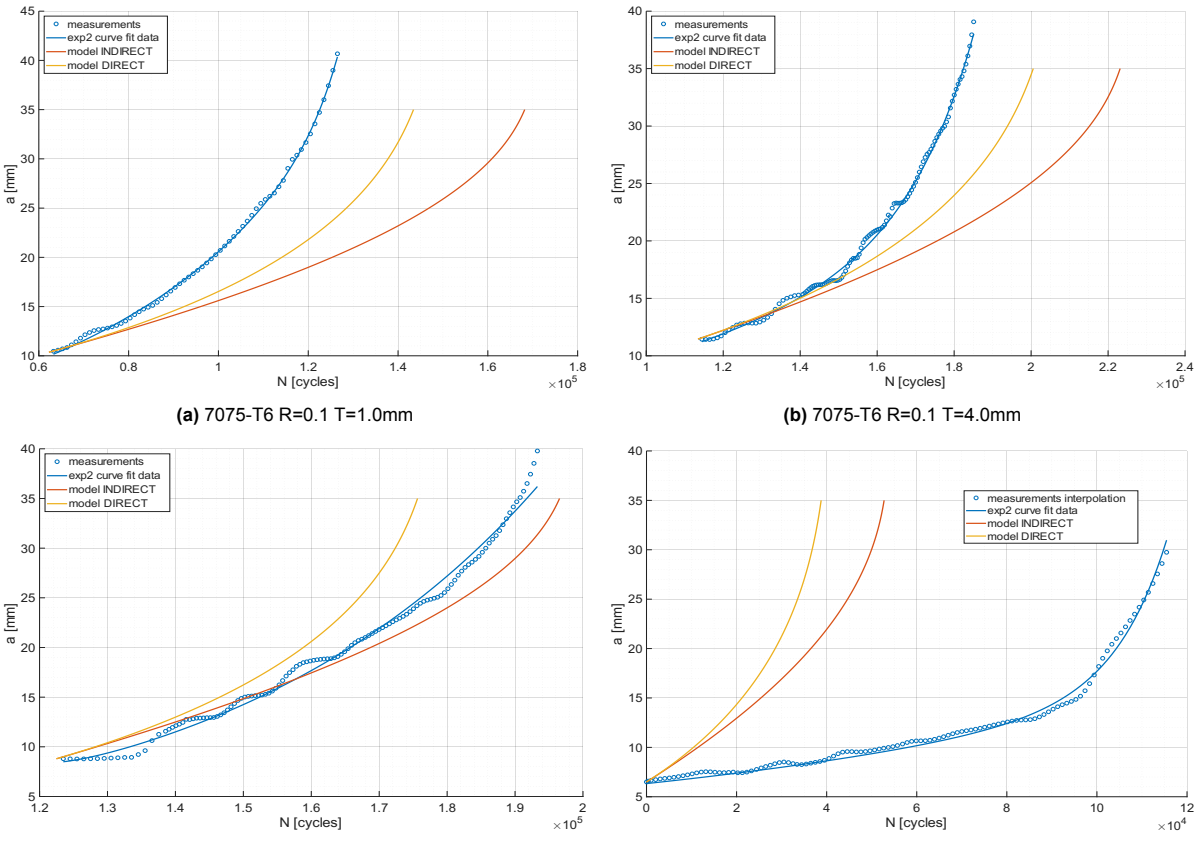

(a) 7075-T6 R=0.1 T=1.0mm

(b) 7075-T6 R=0.1 T=4.0mm

(c) 7075-T6 R=0.1 T=6.43mm

(d) 7075-T6 R=0.1 T=6.43mm at low temperature ($-30°$C)

Figure E.1: Fatigue crack growth rate plots based on the Von Mises plastic zone version of the EBSB model versus experimental data. Page 1.

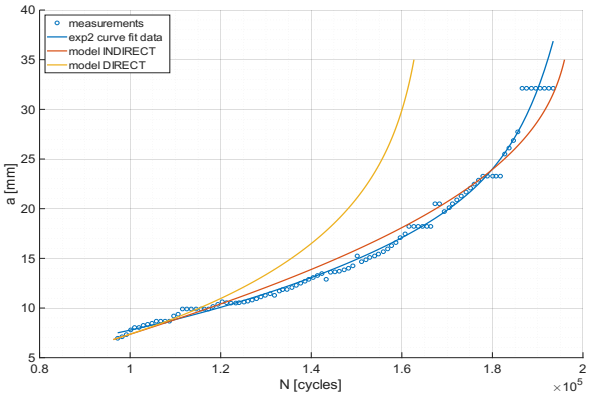

(a) 7075-T6 R=0.5 T=6.43mm

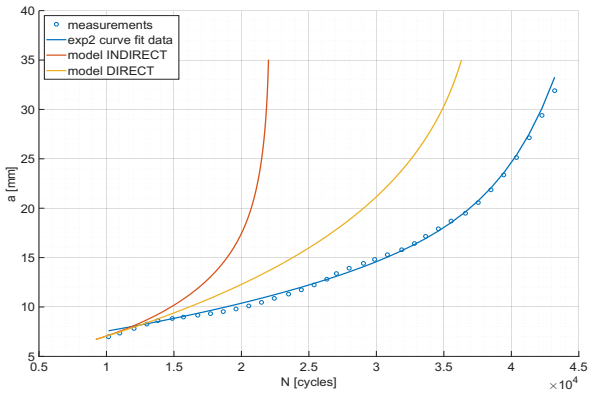

(b) 2024-A300 T-L R=0.1 T=6.36mm

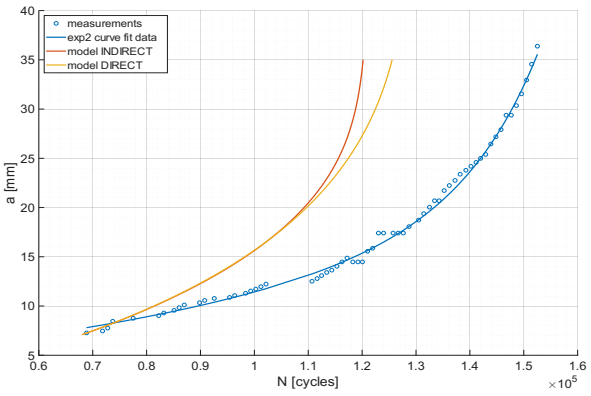

(c) 2024-T3 T-L R=0.1 T=6.36mm

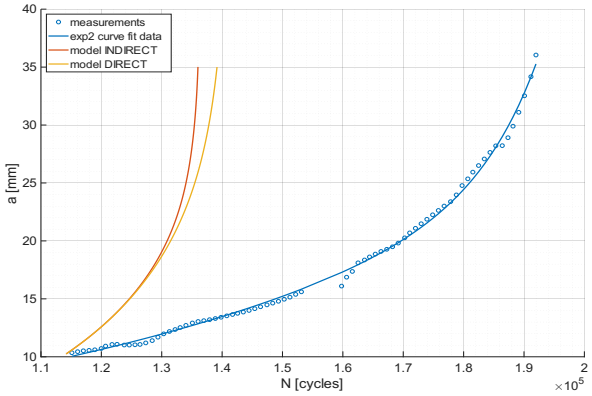

(d) 2024-T3 T-L R=0.5 T=6.36mm

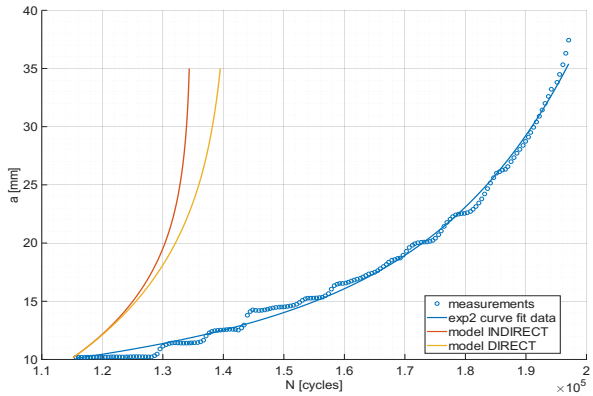

(e) 6061-T6 R=0.5 T=6.50mm

Figure E.2: Crack length a versus cycles N with experimental data, indirect, and direct original EBSB model with Irwin plastic zone. Page 2.

E.1. Irwin (Original) Plastic Zone EBSB Results

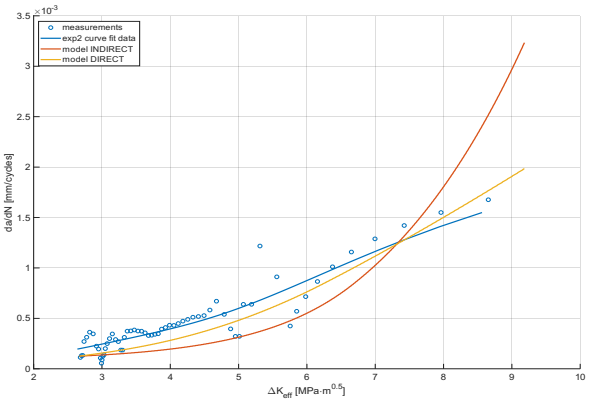

(a) 7075-T6 R=0.1 T=1.0mm - da/dN versus ΔK_{eff} with experimental data, indirect, and direct EBSB

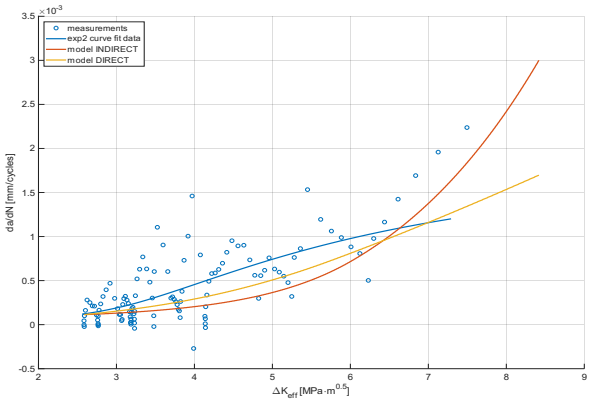

(b) 7075-T6 R=0.1 T=4.0mm - da/dN versus ΔK_{eff} with experimental data, indirect, and direct EBSB

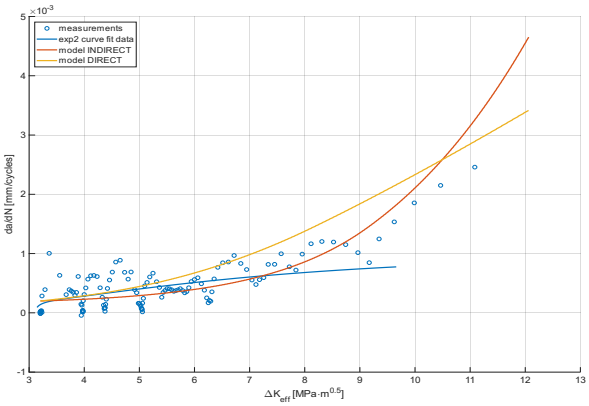

(c) 7075-T6 R=0.1 T=6.43mm - da/dN versus ΔK_{eff} with experimental data, indirect, and direct EBSB

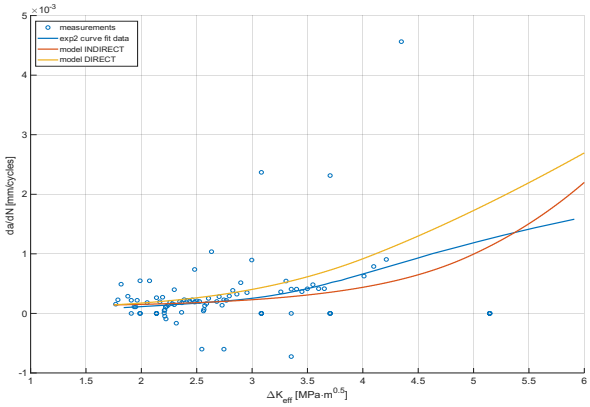

(d) 7075-T6 R=0.5 T=6.43mm - da/dN versus ΔK_{eff} with experimental data, indirect, and direct EBSB

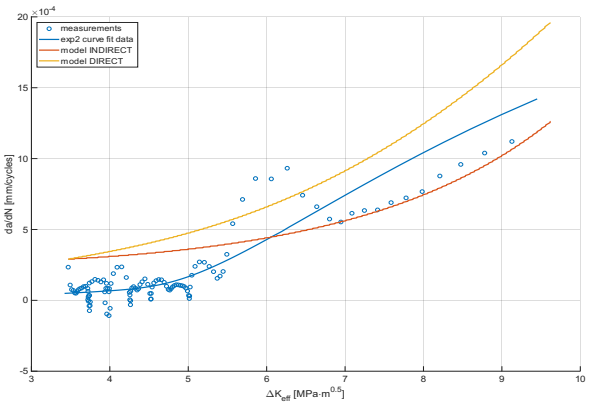

(e) 7075-T6 R=0.1 T=6.43mm at low temperature (-30°C) - da/dN versus ΔK_{eff} with experimental data, indirect, and direct EBSB

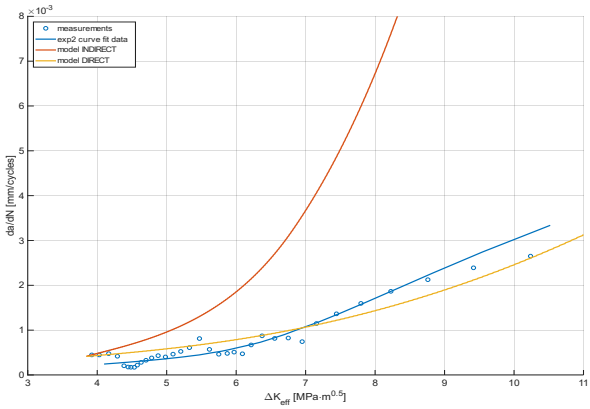

(f) 2024-A300 T-L R=0.1 T=6.36mm - da/dN versus ΔK_{eff} with experimental data, indirect, and direct EBSB

Figure E.3: Fatigue crack growth rate plots based on the original EBSB model by Kuijk [13] versus experimental data. Page 1.

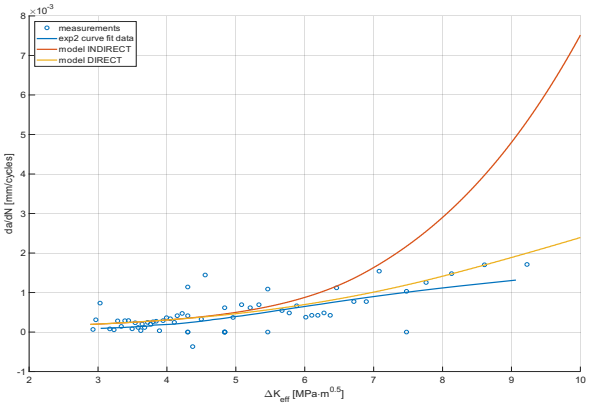

(a) 2024-T3 T-L R=0.1 T=6.36mm - da/dN versus ΔK_{eff} with experimental data, indirect, and direct EBSB

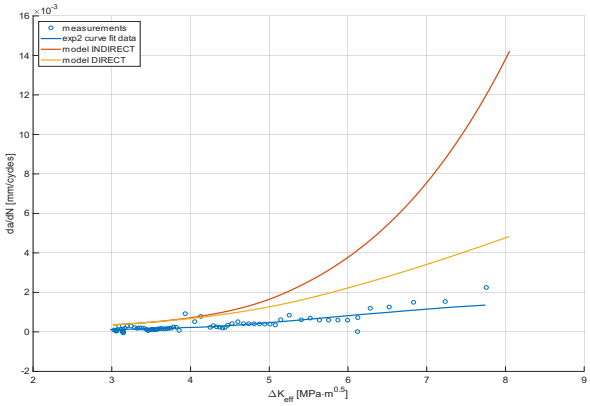

(b) 2024-T3 T-L R=0.5 T=6.36mm - da/dN versus ΔK_{eff} with experimental data, indirect, and direct EBSB

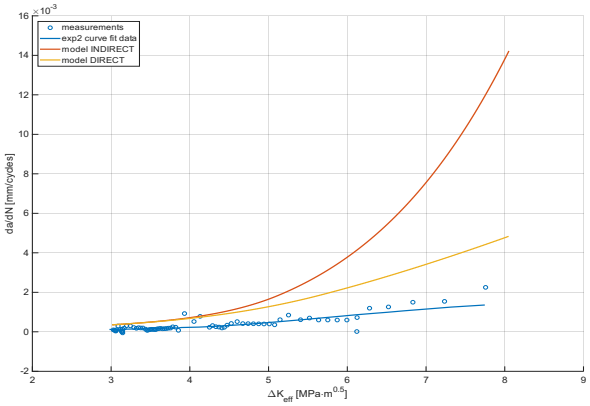

(c) 6061-T6 R=0.5 T=6.50mm - da/dN versus ΔK_{eff} with experimental data, indirect, and direct EBSB

Figure E.4: Fatigue crack growth rate plots based on the original EBSB model by Kuijk [13] versus experimental data. Page 2.

E.2. Dugdale Plastic Zone EBSB Results

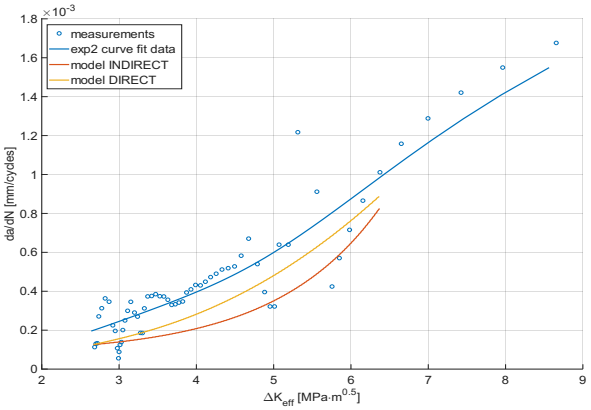

(a) 7075-T6 R=0.1 T=1.0mm - da/dN versus ΔK_{eff} with experimental data, indirect, and direct EBSB model with Dugdale plastic zone

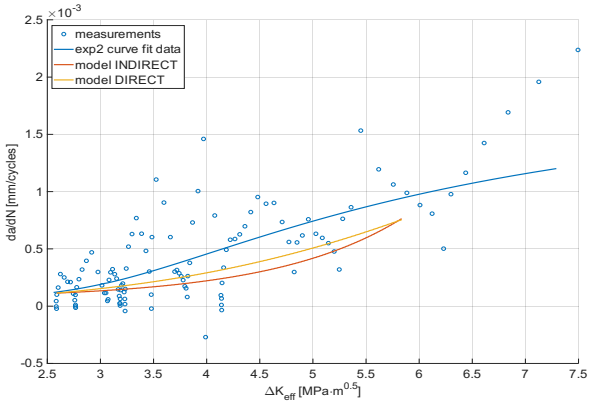

(b) 7075-T6 R=0.1 T=4.0mm - da/dN versus ΔK_{eff} with experimental data, indirect, and direct EBSB model with Dugdale plastic zone

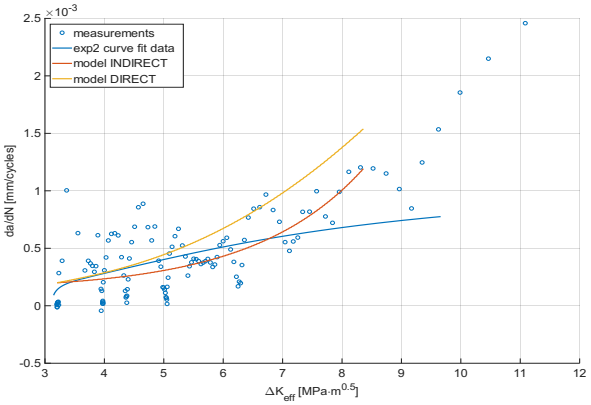

(c) 7075-T6 R=0.1 T=6.43mm - da/dN versus ΔK_{eff} with experimental data, indirect, and direct EBSB model with Dugdale plastic zone

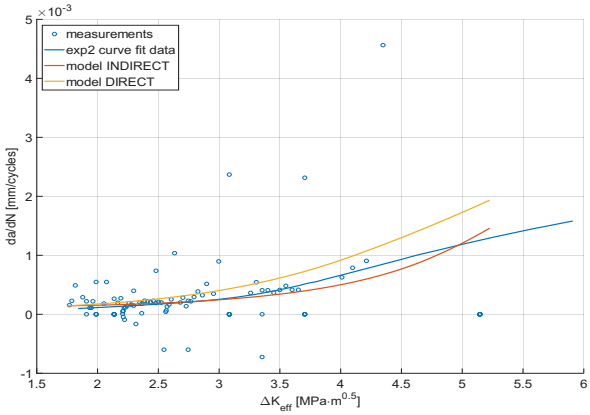

(d) 7075-T6 R=0.5 T=6.43mm - da/dN versus ΔK_{eff} with experimental data, indirect, and direct EBSB model with Dugdale plastic zone

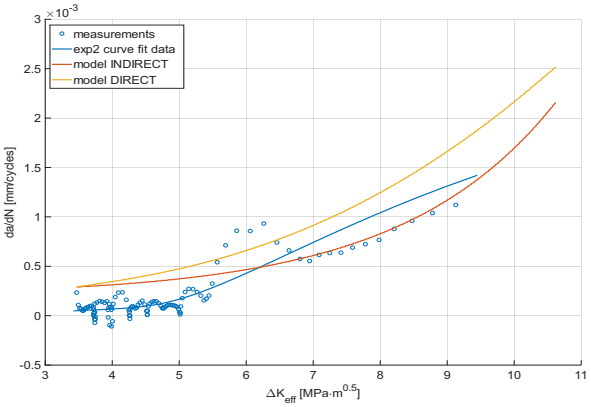

(e) 7075-T6 R=0.1 T=6.43mm at low temperature ($-30°$C) - da/dN versus ΔK_{eff} with experimental data, indirect, and direct EBSB model with Dugdale plastic zone

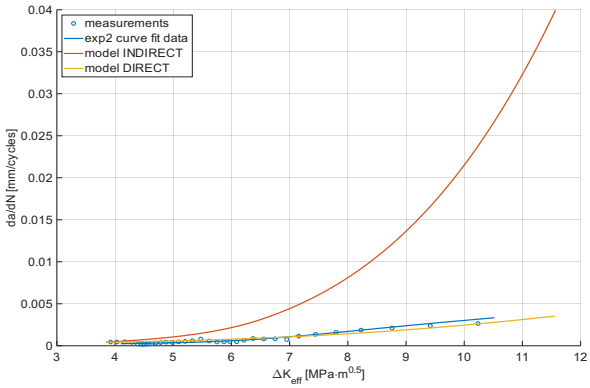

(f) 2024-A300 T-L R=0.1 T=6.36mm - da/dN versus ΔK_{eff} with experimental data, indirect, and direct EBSB model with Dugdale plastic zone

Figure E.5: Fatigue crack growth rate plots based on the Dugdale plastic zone version of the EBSB model versus experimental data. Page 1.

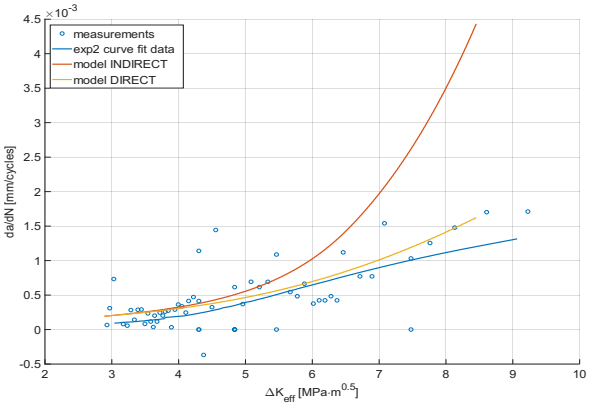

(a) 2024-T3 T-L R=0.1 T=6.36mm - da/dN versus ΔK_{eff} with experimental data, indirect, and direct EBSB model with Dugdale plastic zone

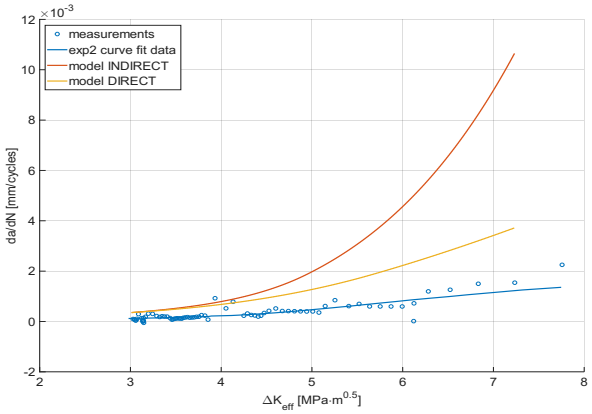

(b) 2024-T3 T-L R=0.5 T=6.36mm - da/dN versus ΔK_{eff} with experimental data, indirect, and direct EBSB model with Dugdale plastic zone

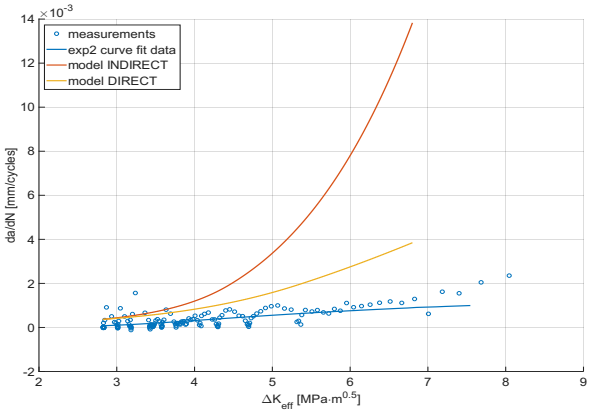

(c) 6061-T6 R=0.5 T=6.50mm - da/dN versus ΔK_{eff} with experimental data, indirect, and direct EBSB model with Dugdale plastic zone

Figure E.6: Fatigue crack growth rate plots based on the Dugdale plastic zone version of the EBSB model versus experimental data. Page 2.

E.3. Von Mises Criterion Plastic Zone EBSB Results

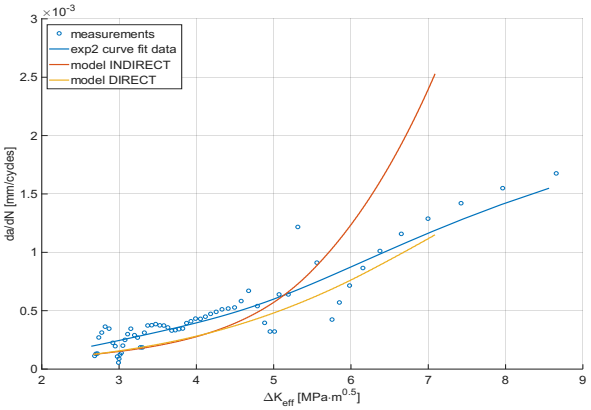

(a) 7075-T6 R=0.1 T=1.0mm - da/dN versus ΔK_{eff} with experimental data, indirect, and direct EBSB model with Von Mises plastic zone

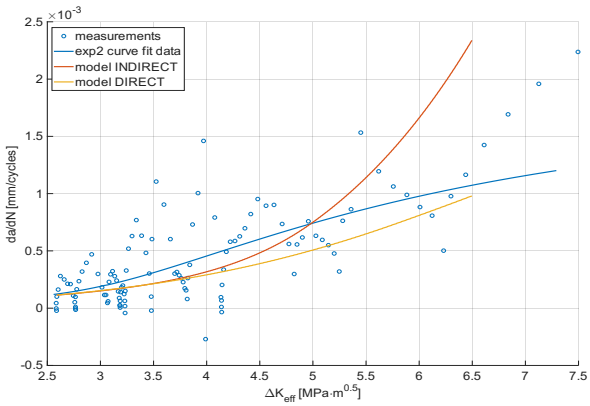

(b) 7075-T6 R=0.1 T=4.0mm - da/dN versus ΔK_{eff} with experimental data, indirect, and direct EBSB model with Von Mises plastic zone

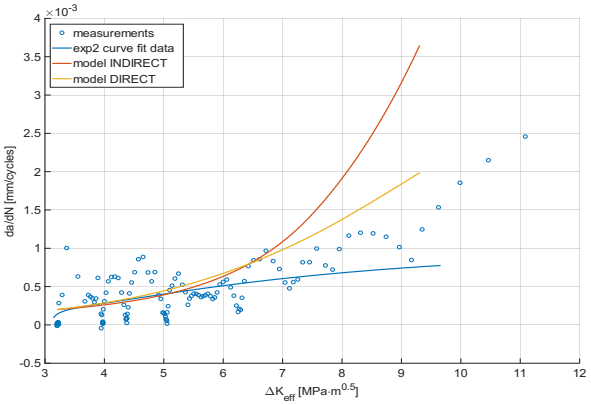

(c) 7075-T6 R=0.1 T=6.43mm - da/dN versus ΔK_{eff} with experimental data, indirect, and direct EBSB model with Von Mises plastic zone

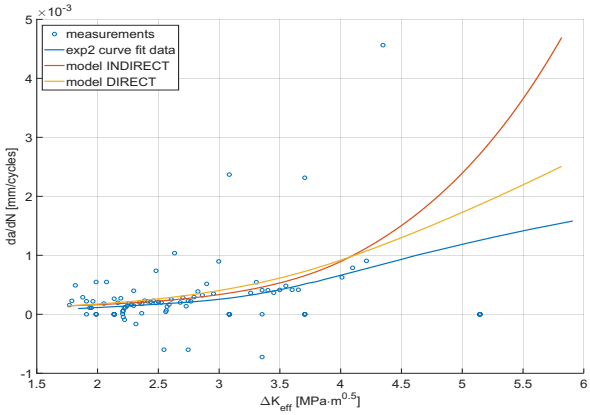

(d) 7075-T6 R=0.5 T=6.43mm - da/dN versus ΔK_{eff} with experimental data, indirect, and direct EBSB model with Von Mises plastic zone

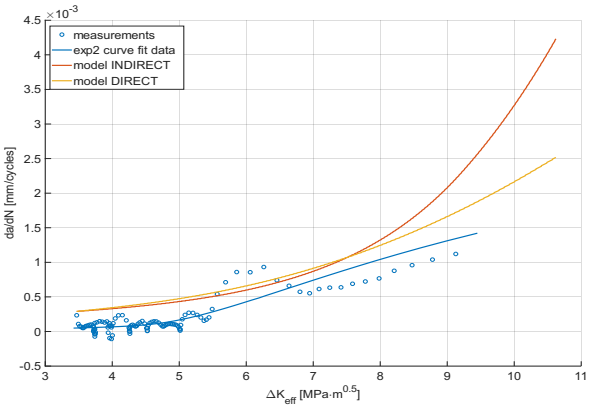

(e) 7075-T6 R=0.1 T=6.43mm at low temperature ($-30°$C) - da/dN versus ΔK_{eff} with experimental data, indirect, and direct EBSB model with Von Mises plastic zone

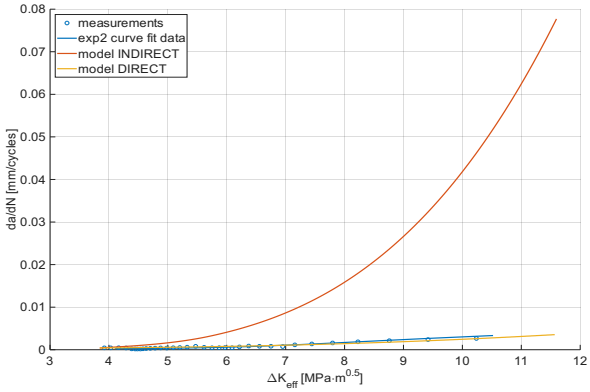

(f) 2024-A300 T-L R=0.1 T=6.36mm - da/dN versus ΔK_{eff} with experimental data, indirect, and direct EBSB model with Von Mises plastic zone

Figure E.7: Fatigue crack growth rate plots based on the Von Mises plastic zone version of the EBSB model versus experimental data. Page 1.

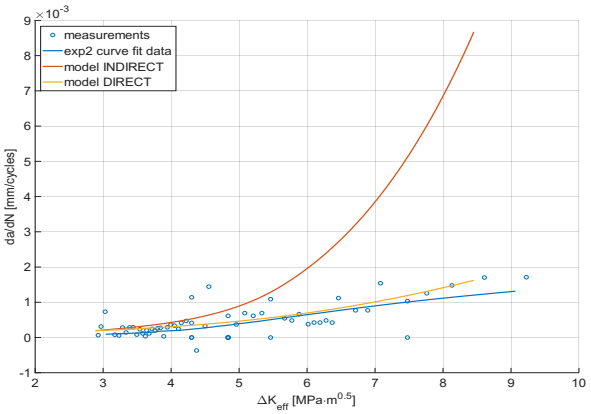

(a) 2024-T3 T-L R=0.1 T=6.36mm - da/dN versus ΔK_{eff} with experimental data, indirect, and direct EBSB model with Von Mises plastic zone

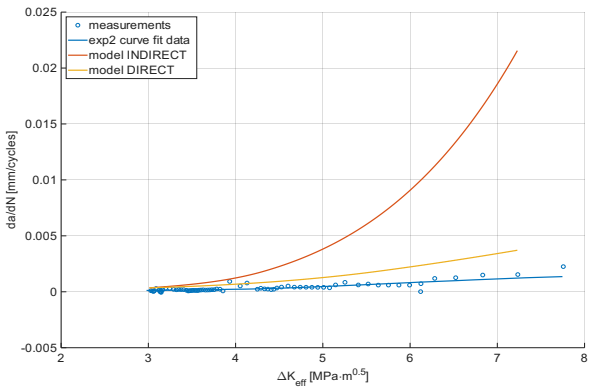

(b) 2024-T3 T-L R=0.5 T=6.36mm - da/dN versus ΔK_{eff} with experimental data, indirect, and direct EBSB model with Von Mises plastic zone

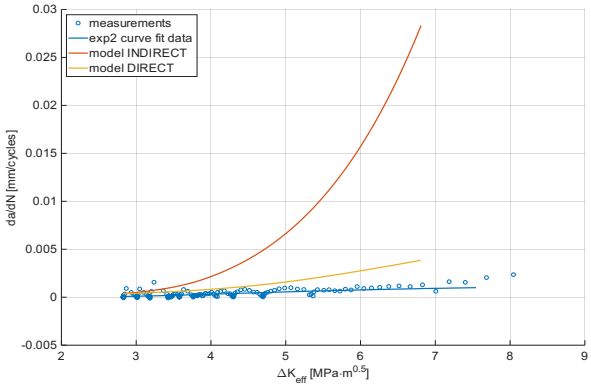

(c) 6061-T6 R=0.5 T=6.50mm - da/dN versus ΔK_{eff} with experimental data, indirect, and direct EBSB model with Von Mises plastic zone

Figure E.8: Fatigue crack growth rate plots based on the Von Mises plastic zone version of the EBSB model versus experimental data. Page 2.

F

Additional Figures

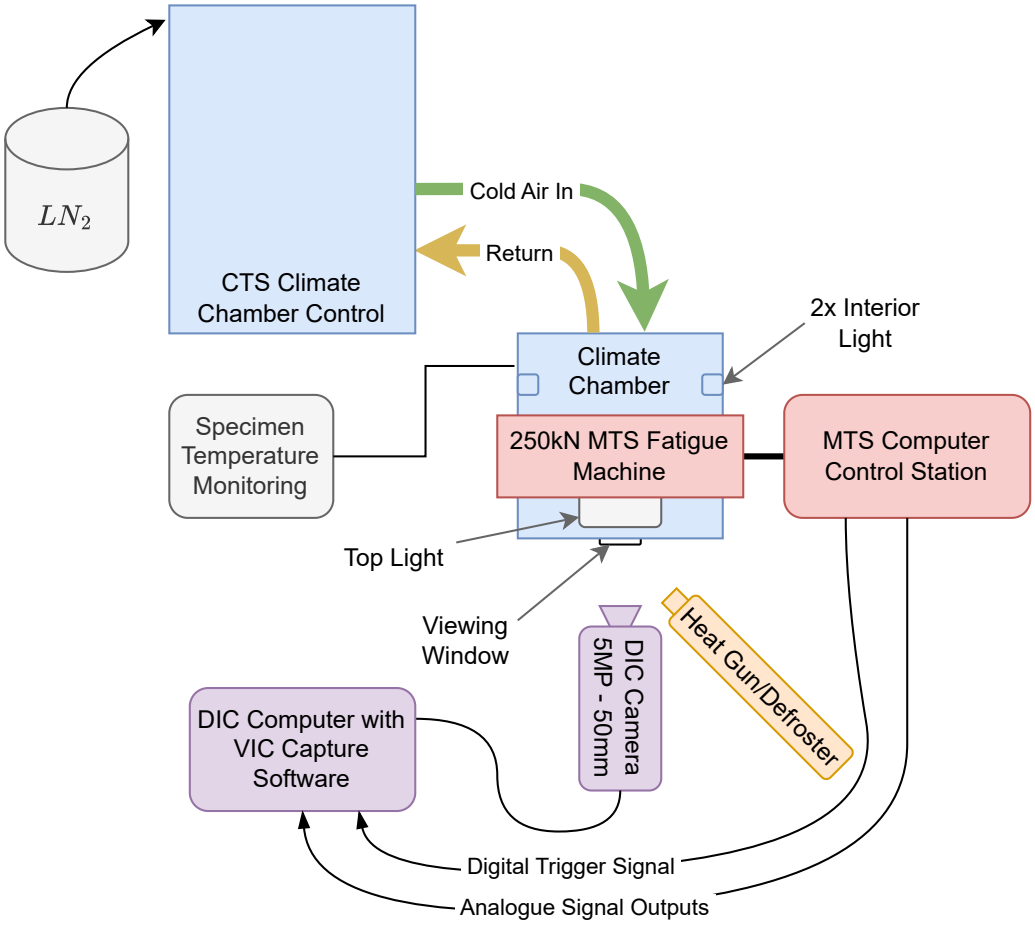

Figure F.1: Low temperature fatigue testing schematic setup.